LLE Review

UR
LLE

Quarterly Report

About the Cover:

Scientist Andrei Babushkin is shown aligning a frequency-tripling crystal in the apparatus he is using to demonstrate a new dual-tripler scheme for converting the infrared light of OMEGA to the third harmonic in the ultraviolet. This crystal has been placed in front of a large octagonal mounting that holds a doubler-tripler crystal pair. Together, these three crystals triple the frequency of infrared light with high efficiency over a significantly wider bandwidth than has been obtainable until now with doubler-tripler pairs alone. When implemented on the OMEGA laser system, efficient frequency tripling over widened bandwidths will allow the use of broadband beam-smoothing techniques with faster smoothing times than have been possible until now. Dr. Babushkin is one of a team of several scientists from LLE and elsewhere involved in the development of this technique.

For questions or comments, contact Reuben Epstein, *Editor*, Laboratory for Laser Energetics, 250 East River Road, Rochester, NY 14623-1299, (716) 275-5405.

Worldwide-Web Home Page: http://www.lle.rochester.edu/

LLE Review

Quarterly Report

UR ✸
LLE

Contents

In Brief

This volume of the LLE Review, covering the period April–June 1998, includes a report on a recent series of experiments, performed by A. Babushkin, M. Guardalben, R. Keck, and W. Seka, that demonstrate a new scheme for converting the infrared light of OMEGA to the third harmonic in the ultraviolet over a bandwidth that is significantly wider than has been previously attainable. This innovative scheme, employing a second tripling crystal in addition to the doubler-tripler pair currently in use, was proposed by D. Eimerl at Lawrence Livermore National Laboratory and adapted to the OMEGA system by S. Craxton and S. Oskoui, a recent participant in LLE's Summer High-School Research Program. Wider bandwidths on OMEGA will allow the use of broadband beam smoothing with faster smoothing times than have been employed until now.

Additional research highlights reported in this issue are

- O. Konoplev, Y. Fisher, and D. Meyerhofer report on ultrahigh-dynamic-range measurements of high-contrast pulses using a second-order autocorrelator that they have designed and built. This device is capable of measurements with dynamic ranges of up to ~10^{12} at a time resolution of ~50 fs, the highest dynamic range yet achieved for measurements with this degree of time resolution.

- D. Harding describes results from two ion-beam analysis techniques—Rutherford backscattering spectroscopy and nuclear resonance analysis—that have been used to provide an accurate method for determining the complete elemental composition of capsules and target materials used at LLE. These new sources of information are more expansive than other analytical techniques in use, and the data are needed for interpreting the results of our experiments.

- By placing a pinhole array in front of a flat-crystal x-ray spectrometer, B. Yaakobi has introduced a diagnostic technique with the ability to obtain simultaneously a large number of two-dimensional images over a wide range of photon energies at a high degree of spectral resolution. This article presents images of $K\alpha$ fluorescence pumped by core radiation, delineating the compressed, cold shell, and pumped by suprathermal electrons, showing that ~1% of the laser energy preheats the target.

- The simultaneous forward and backward stimulated Brillouin scattering (SBS) of crossed laser beams is described in detail by C. McKinstrie and E. Startsev. They obtain new analytical solutions for the linearized equations governing the transient phase of the instability and the nonlinear equations governing the steady state. These solutions show that backward SBS dominates the initial evolution of the instability, whereas forward SBS dominates the steady state.

- R. Short and A. Simon have calculated the damping of localized plasma waves using a new physical approach that is linear in the wave field and that avoids introducing complex particle velocities. The simplicity of this approach is obtained by invoking the time-reversal invariance of the Vlasov equation. This greatly simplifies the calculation of Landau damping of plasma waves in an infinite of medium and "transit-time damping" of plasma waves localized in general geometries.

Reuben Epstein
Editor

Demonstration of Dual-Tripler, Broadband Third-Harmonic Generation and Implications for OMEGA and the NIF

A critical concern for Nd:glass fusion lasers such as OMEGA and the National Ignition Facility (NIF) is the uniformity of irradiation experienced by the fusion target. Uniform beams are generated by beam-smoothing schemes such as smoothing by spectral dispersion (SSD),[1] which vary the instantaneous speckle pattern on target on time scales that are short compared with relevant hydrodynamic time scales. In a simplified picture of beam smoothing, the laser presents a new speckle pattern to the target every coherence time, where the coherence time is given by the inverse of the bandwidth. The beam is smoothed because the target responds hydrodynamically to the average of a large number of independent speckle patterns. The ratio of the coherence time to the relevant hydrodynamic time is thus a key parameter. Alternatively stated, the time required to obtain a given level of uniformity is inversely proportional to the laser bandwidth.

Smoothing achieved using present fusion lasers is limited by the bandwidth acceptance of the KDP crystals that are used for third-harmonic generation (THG). Conventionally, THG involves frequency doubling in a first, "doubler" crystal followed by sum-frequency mixing in a second, "tripler" crystal.[2] Eimerl et al.[3] recently proposed, however, that broader-bandwidth THG can be achieved by using dual triplers, i.e., two tripler crystals in series with slightly different angular detunings from phase matching and appropriately chosen thicknesses. Oskoui[4] showed that by adding a second tripler to the existing conversion crystals in each beamline of the OMEGA laser system it is possible to increase the bandwidth acceptance by a factor of 3, and he developed an optimized design. Conversion of OMEGA to dual-tripler THG is now underway.

This article reports on what is believed to be the first experimental demonstration of dual-tripler THG. A second (type-II) KDP tripler, with 9-mm thickness, was added to a tripling cell (used on the former 24-beam OMEGA laser system) containing two type-II, 16-mm KDP crystals. All crystals were antireflection coated. The dual-tripler configuration was tested using a narrow-bandwidth, high-power laser beam whose angle of incidence on the crystals was varied. The

THG conversion efficiency was measured as a function of this angle. Since an angular tilt of the incident IR beam is equivalent to a change in its wavelength (this relationship is linear to a good approximation, with ~ -160 μrad equivalent to 1 Å[5]), a measured increase in the angular acceptance of the THG conversion is equivalent to a proportional increase in the THG acceptance bandwidth.

One important parameter investigated in the experiment was the separation between the two triplers. The relative phase $\Delta\Phi$ between the three interacting waves (defined as $\Delta\Phi = \Phi_3 - \Phi_2 - \Phi_1$, where Φ_i is the phase of harmonic i) can change due to a number of factors, including dispersion in the air path between the triplers, dispersion in the windows of the crystal cell, and phase changes due to the coatings on the crystal surfaces. (The relative phase within a tuned crystal is zero by the definition of phase matching.) Using the formula $(n-1) \times 10^7 = 2726.43 + 12.288/\lambda^2 + 0.3555/\lambda^4$, where n is the refractive index and the wavelength λ is in μm,[6] 4.0 cm of air is predicted to be equivalent to a full cycle of phase shift [i.e., $(k_3 - k_2 - k_1)L = 2\pi$, where k_i is the wave vector in air of harmonic i and $L = 4$ cm]. In the experiment, the relative phase $\Delta\Phi$ emerging from the first tripler was unknown due to dispersion in the output cell window; thus, to ensure the optimum $\Delta\Phi$ at the input to the second tripler, it was necessary to adjust the air gap to the optimum position within this 4-cm range.

This article extends the work of Ref. 7, which reports the experimental results, to include details of the dual-tripler design currently being implemented on OMEGA and a dual-tripler design that could provide a comparable bandwidth on the NIF.
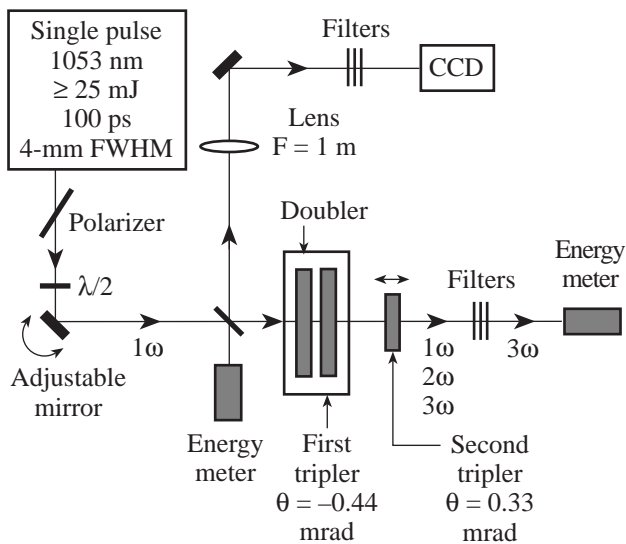
Experiment

The laser beam used in the experiment originated from a Nd:YLF-based, diode-pumped, mode-locked oscillator that generated a train of bandwidth-limited, 100-ps-duration pulses. A single pulse was switched out and amplified in a flash-lamp-pumped, negative-feedback-controlled, regenerative amplifier[8] and two subsequent single-pass, flash-lamp-

pumped, Nd:YLF amplifiers separated by spatial filters. This produced a collimated beam with 100-ps time duration, up to 25 mJ of energy, and an approximately Gaussian spatial profile with a FWHM diameter of 4 mm.

The experimental setup is shown in Fig. 75.1. The input laser beam was reflected off an adjustable mirror, which was used to vary its angle of incidence on the crystals. Back-reflections from the crystal surfaces were transported through a 1-m focus lens onto a CCD camera to monitor the beam alignment relative to the crystals and the relative alignment between the crystals. The polarization of the incoming beam was adjusted using a half-wave plate to be 35° with respect to the *o* axis of the first crystal. The second tripler was mounted on a stage with a 5-cm translation range, which was required to optimize the relative phase between the three interacting waves incident on the second tripler. The crystals were set up using the converging-lens technique[9] with a separation of ~0.77 mrad between the phase-matching directions of the two triplers, this angle being the optimum predicted separation.

Single pulse
1053 nm
≥ 25 mJ
100 ps
4-mm FWHM

Filters

CCD

Lens
F = 1 m

Polarizer

Doubler

λ/2

Energy meter

1ω

Filters

Adjustable mirror

1ω
2ω
3ω

1ω   3ω

Energy meter   First tripler
θ = −0.44 mrad

Second tripler
θ = 0.33 mrad

E8928

Figure 75.1
Experimental setup.

The experimental results are shown in Fig. 75.2 for five values of the air gap spanning the 4-cm range in 1-cm increments. The results are in excellent agreement with predictions of the plane-wave code Mixette (based on Ref. 2), which calculates the conversion averaged over the assumed Gaussian spatial and temporal beam profiles at a nominal intensity of 1.2 GW/cm^2.

The conversion efficiency was measured as the ratio of the energy of the third-harmonic beam at the output of the second tripler to the energy of the fundamental beam at the input to the doubler. For each angular position several measurements (typically 5 to 7) were made, and the averaged value was used as the measured conversion efficiency. Typically the averaged data had an uncertainty (standard deviation) of the order of 1% or less, although in a few cases the uncertainty was as large as ~5%.

Small scaling factors were applied to the experimental measurements (0.95 to the angle and 1.04 to the conversion) to account for systematic uncertainties in the accuracies with which the values of angles and intensities were measured. These scaling factors were determined from one data set and were then maintained constant for the remainder of the experiment. The calculations assumed that the first tripler was detuned to be phase matched for a beam tilt of −0.44 mrad on the horizontal axes of Fig. 75.2. The corresponding tilt for the second tripler was 0.33 mrad, all tilt angles quoted in this article being external to the crystals. (The absolute values of these angles were not known experimentally.) The optimum air gap [corresponding to Figs. 75.2(a) and 75.2(e)] was assumed to be 1.5 cm away from the point of no net dispersion [midway between that in Figs. 75.2(c) and 75.2(d)]. The sign of this distance depends on the orientations of the optic axes of the triplers, which were parallel in this experiment. The calculations shown in Fig. 75.2 assumed a 4.1-cm period, which was found to fit the data slightly better than the predicted 4.0-cm period; this small difference is ascribed to different temperatures, humidity, etc., from those of Ref. 6.

The nominal laser intensity I_{nom}, defined as

$$E \big/ \left(\pi r_{HW}^2 \tau_{FWHM} \right),$$

where E is the laser energy and $2r_{HW}$ and τ_{FWHM} are the spatial and temporal FWHM's, respectively, was 1.2 GW/cm^2, corresponding to a peak intensity in space and time of 0.78 GW/cm^2. The low conversion efficiencies shown in Fig. 75.2 are primarily a result of the non-optimum beam profile (Gaussian in both space and time), for which 50% of the IR energy is incident at less than 30% of the peak intensity. This is illustrated in Fig. 75.3, which reproduces the data and calculated curve of Fig. 75.2(e) and adds predictions for what would have been obtained with different beam spatial and temporal profiles. It is seen that conversion efficiencies up to 80% would have resulted for beams flat in space and time.
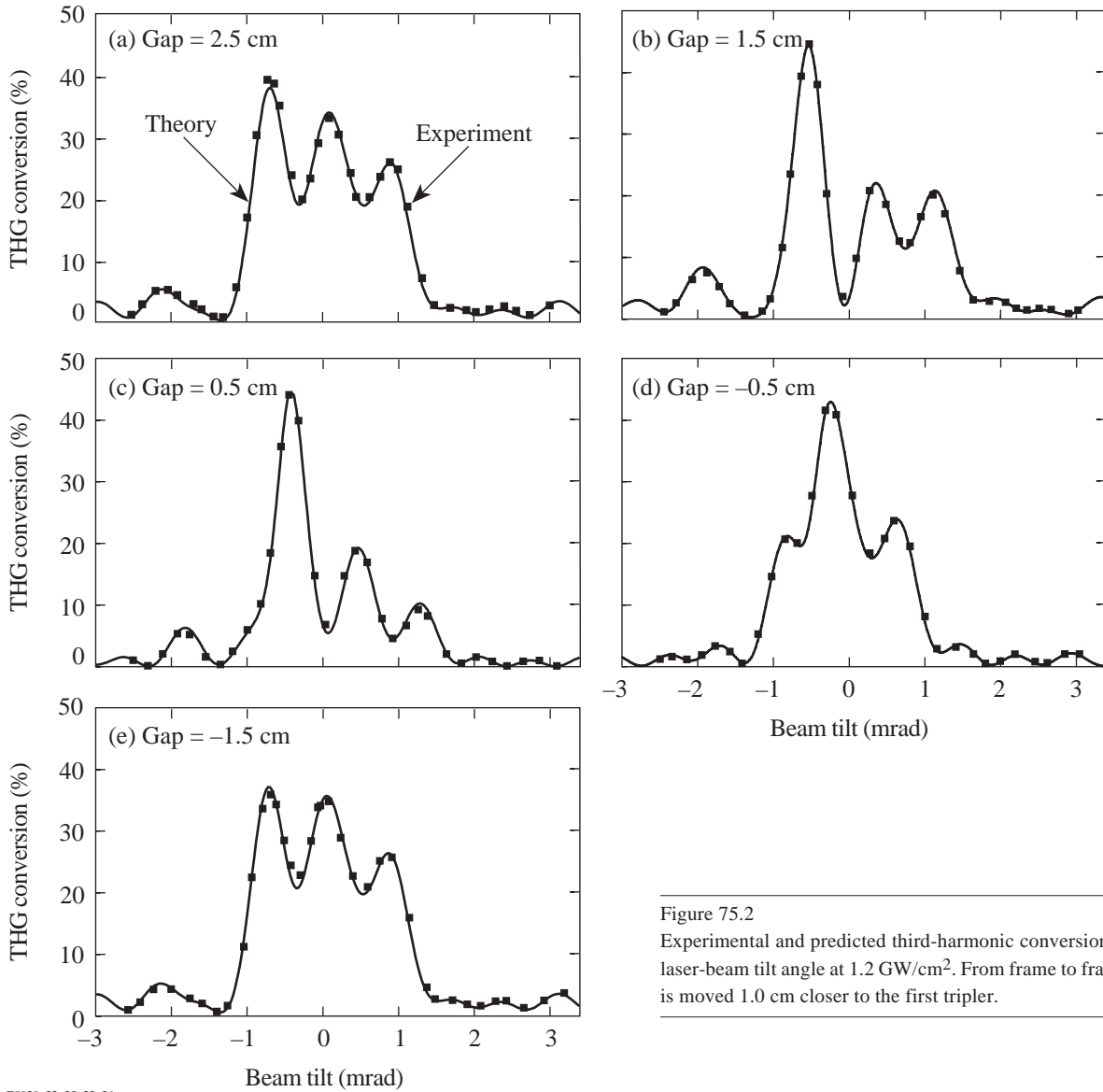
Figure 75.2
Experimental and predicted third-harmonic conversion as a function of the laser-beam tilt angle at 1.2 GW/cm^2. From frame to frame the second tripler is moved 1.0 cm closer to the first tripler.
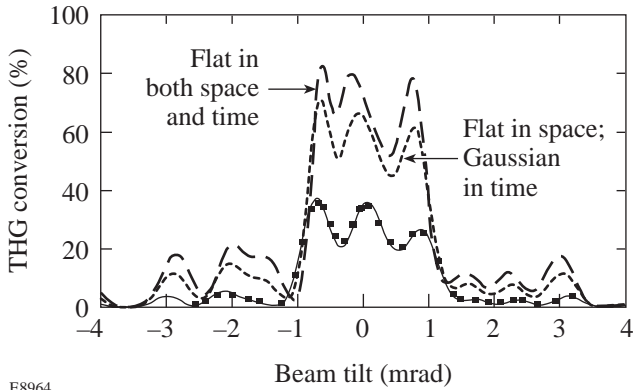
Figure 75.3
THG conversion versus beam tilt angle for the conditions of Fig. 75.2(e) (solid curve and data points) together with predictions for what would have been obtained if the beam were flat in space but Gaussian in time (dotted curve) and flat in both space and time (dashed curve). All curves are for a nominal intensity of 1.2 GW/cm^2.

Design for OMEGA

Figure 75.4 shows predictions for single rays (i.e., beams that are flat in space and time) for the OMEGA laser system, assuming that an 8-mm tripler crystal is added to each beam after the existing conversion crystals (which are both 12.2-mm, type-II KDP crystals). Here the first tripler is detuned 0.62 mrad (to phase match at −3.84 Å), and the second is detuned −0.38 mrad (to phase match at 2.36 Å). The air gap is 1.0 cm. Curves are shown for intensities from 0.5 to 1.5 GW/cm^2, spanning the range of normal operating conditions, and for small signal (0.1 GW/cm^2). At 1.5 GW/cm^2, the FWHM bandwidth is 13.8 Å, corresponding to 1.1 THz at 351 nm, and at lower intensities the bandwidth is slightly greater.

TC4624

Figure 75.4
Predicted performance of the OMEGA laser system as a function of IR wavelength shift, for the addition of a second tripler of 8-mm thickness at a separa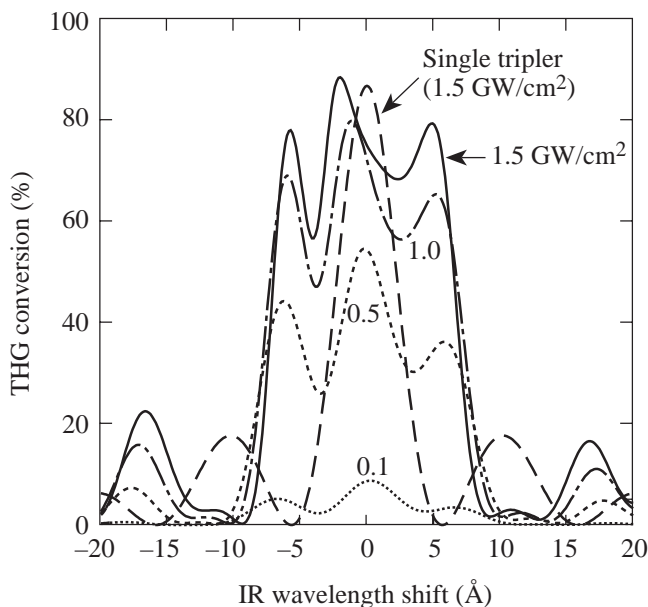tion of 1.0 cm. The curves correspond to intensities ranging from 1.5 to 0.1 GW/cm^2. The dashed curve corresponds to the existing system at 1.5 GW/cm^2. At this intensity, the extra tripler increases the FWHM bandwidth from 4.9 Å to 13.8 Å (1.1 THz in the UV). The curves in this and similar figures are calculated for monochromatic beams with varying wavelength.

The shape of the dual-tripler curve at 1.5 GW/cm^2 is advantageous for the conversion of a broad-bandwidth phase-modulated beam. The THG conversion is maintained in the 60%–90% range as the IR wavelength varies through ±6 Å. In contrast, the single-tripler curve results in significant loss beyond ±2 Å. In a typical SSD laser beam, the instantaneous wavelength will vary in time through ±6 Å at any point in the

beam cross section, and, at each time, it will exhibit a similar variation across the beam aperture. The net conversion integrated over the beam will then correspond to some average over wavelength of the curves of Fig. 75.4, depending on the specific parameters of the SSD design used.

The dual-tripler design being implemented on OMEGA calls for the triplers to be spaced 1.0 cm apart with a tolerance of ±0.1 cm, and for their relative angular separation to be accurate within 100 μrad. Curves illustrating the effects of these deviations are shown in Fig. 75.5 for the peak anticipated operating intensity of 1.5 GW/cm^2. In both cases, the variations in the predicted conversion curves are considered acceptable. The variations experienced in the spatially averaged conversion efficiency will be less (of the order of 1%–2%) because the curves resulting from deviations from the design lie above the design at some wavelengths and below the design at others.

It is worth noting that the alignment accuracy required by dual-tripler THG is no greater than that already in place on OMEGA. Currently the crystals are tuned to a much smaller tolerance than 100 μrad.

Design for the NIF

Very similar broadband conversion may also be obtained on the NIF. Two designs are considered here (see Table 75.I): The "11/8/10" design was suggested in Ref. 3, although with slightly different tuning angles. (It should be noted that all angles quoted in Ref. 3 are internal to the crystal, i.e., 1.5 times smaller than the external angles quoted here.) The "11/9/9" design is an alternative design that is compatible with the NIF two-crystal base-line design ("11/9").

A comparison between the two dual-tripler designs is shown in Fig. 75.6. The "11/8/10" design provides slightly more conversion and allows slightly more bandwidth; otherwise, the two designs are very similar. The curves are remarkably similar to those of the optimum OMEGA design of Fig. 75.4; again, the range of wavelengths that can be efficiently converted is increased from ±2 Å to ±6 Å.

Comparing either dual-tripler design with the two-crystal base-line design, shown superposed on both plots of Fig. 75.6 at the nominal operating intensity of 3.0 GW/cm^2, it is clear that there will be some loss in overall conversion when averaging over a broadband beam, but probably no more than 10% based on the 3.0-GW/cm^2 curve. (The loss at lower intensities is less.)

The effective beam uniformity resulting from dual-tripler conversion on the NIF may be even greater than that on OMEGA, based on the reasonable presumption that it is the ratio between the coherence time (1/bandwidth) and the relevant hydrodynamic time that is important. The coherence time is the same on each system, but the hydrodynamic time scales are a few times longer on the NIF.

TC4754,55
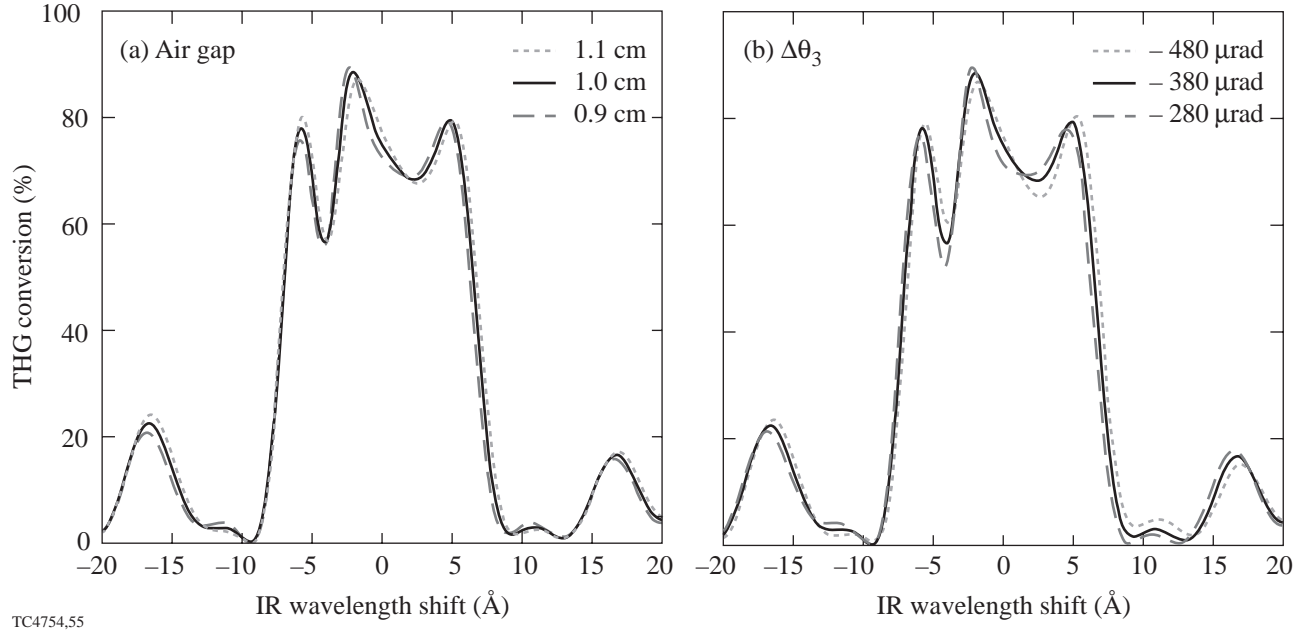
Figure 75.5
Sensitivity of the base-line design for dual-tripler THG on OMEGA to (a) deviations in the air gap between triplers from 1.0 cm and (b) deviations in the tilt angle of the second tripler from −380 μrad. All curves are for the maximum anticipated operating intensity of 1.5 GW/cm^2. Deviations of no greater than (a) ±0.1 cm and (b) ±100 μrad are acceptable.

Table 75.I: Existing and dual-tripler designs for OMEGA and the NIF. Tilt angles $\Delta\theta_i$ are external to the crystals, with a positive angle indicating an increase in the angle between the propagation direction and the optic axis. OMEGA crystals are all type-II KDP; NIF doublers are type-I KDP and triplers type-II KD*P. Subscript "1" indicates the doubler, "2" the first tripler, and "3" the second tripler.

	Crystal thickness (mm)			Crystal tilt (μrad)			Gap between triplers (mm)
	L_1	L_2	L_3	$\Delta\theta_1$	$\Delta\theta_2$	$\Delta\theta_3$	gap
OMEGA, present	12	12	–	0	0	–	–
OMEGA, dual tripler	12	12	8	0	620	−380	10
NIF "11/9" base line	11	9	–	350	0	–	–
NIF "11/8/10"	11	8	10	325	900	−1000	0
NIF "11/9/9"	11	9	9	325	750	−1000	0
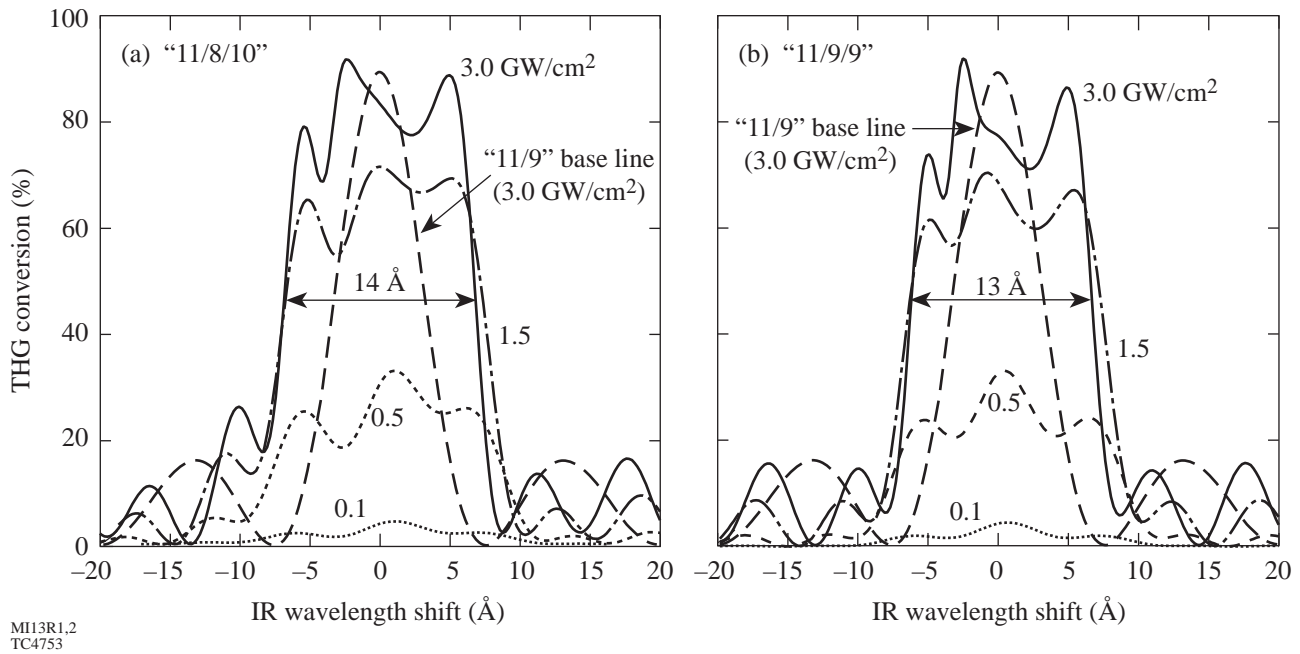
Figure 75.6
Predicted performance for two enhanced-bandwidth designs for the NIF: (a) the "11/8/10" design of Eimerl (Ref. 3) and (b) an alternative "11/9/9" design that leaves the base-line, two-crystal, "11/9" NIF design unchanged.

One important difference between OMEGA and the NIF is that the optimum "11/8/10" and "11/9/9" designs for the NIF require no relative phase change between the triplers. This will indeed be the case on the NIF since the base-line design calls for the crystals to be mounted in vacuum. It is anticipated that the antireflection (AR) coatings on the output of the first tripler and the input to the second tripler will not significantly affect the phase at any wavelength.

Transmission losses between crystal surfaces have not been included in the calculations presented here for OMEGA and the NIF since the AR coatings have not yet been designed. Small losses will be incurred since one cannot simultaneously eliminate reflections at all three wavelengths; however, this does not significantly affect the results presented here.

The sensitivity of the "11/9/9" dual-tripler design for the NIF to angular misalignments of the crystals is shown in Fig. 75.7. In each case, the ideal conversion curve was calculated together with eight variants. In each variant, each crystal was tilted by either $+\Delta\theta$ or $-\Delta\theta$. The shaded areas on the plots indicate the envelope of all eight of these variants, including the worst-case combinations. Again, less variation may occur in some cases for the average over a broadband beam since some curves lie below ideal at some wavelengths and above ideal at others. Results for a tolerance of $\pm 25\ \mu$rad are clearly better than those for $\pm 50\ \mu$rad.

At 1.5 GW/cm^2, the greatest deviations from ideal occur as a result of detunings of the doubler from the design orientation. These deviations are essentially the same that occur for the base-line, two-crystal NIF design and result from the sensitivity of the angle-detuned, type-I/type-II design to doubler orientation;[2] thus, the addition of a second tripler to the NIF does not require any greater angular alignment accuracy than is already included in the base-line design.

Conclusion

The dual-tripler scheme for broadband frequency conversion has been experimentally demonstrated. The close agreement between theory and experiment provides high confidence that the scheme will work on OMEGA and the NIF. On the basis of these results, plans are being made to convert the full OMEGA system. A similar design exists for the NIF. For both laser systems, an approximate threefold increase in bandwidth can be expected, which should result in a threefold reduction in smoothing time and correspondingly more-uniform target implosions.
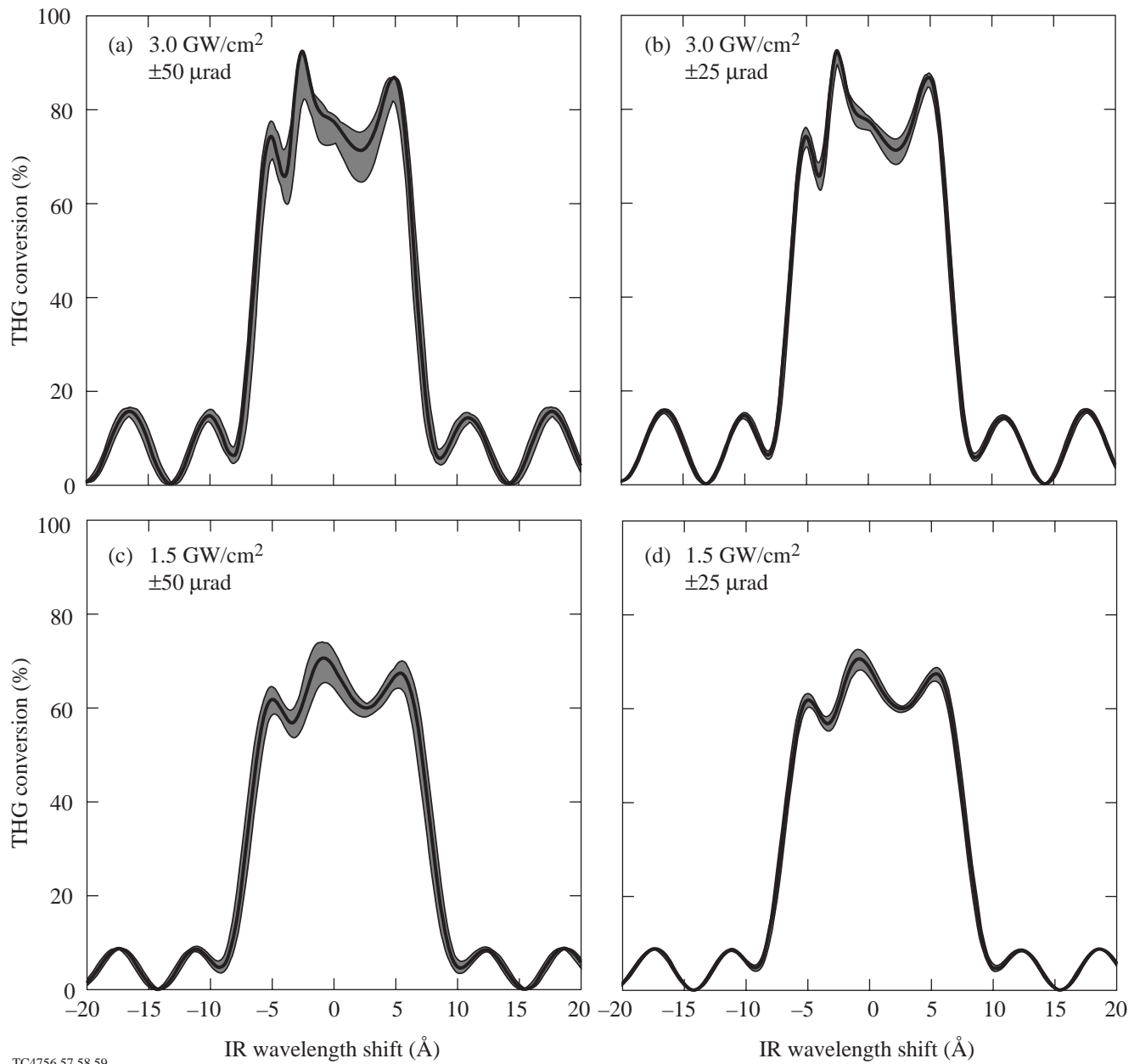
TC4756,57,58,59

Figure 75.7
Sensitivity of the "11/9/9" NIF design to crystal alignment errors. In each case the solid line indicates the ideal conversion curve. The shaded area indicates the full range of possible curves (eight combinations) resulting from simultaneously applying errors of $\pm\Delta\theta$ (external) to each of the three crystals, where $\Delta\theta$ = 50 μrad [(a) and (c)] and 25 μrad [(b) and (d)]. The results for 3.0 GW/cm^2, the peak operating intensity [(a) and (b)], are not greatly different from those for 1.5 GW/cm^2 [(c) and (d)].

REFERENCES

1. S. Skupsky, R. W. Short, T. Kessler, R. S. Craxton, S. Letzring, and J. M. Soures, J. Appl. Phys. **66**, 3456 (1989).

2. R. S. Craxton, IEEE J. Quantum Electron. **QE-17**, 1771 (1981).

3. D. Eimerl *et al.*, Opt. Lett. **22**, 1208 (1997).

4. S. Oskoui, Laboratory for Laser Energetics Report No. 277, NTIS document No. DOE/SF/19460-173 (1996). Copies may be obtained from the National Technical Information Service, Springfield, VA 22161.

5. R. S. Craxton, S. D. Jacobs, J. E. Rizzo, and R. Boni, IEEE J. Quantum Electron. **QE-17**, 1782 (1981).

6. R. C. Weast, ed. *CRC Handbook of Chemistry and Physics*, 58th ed. (CRC Press, Cleveland, OH, 1977), p. E-224.

7. A. Babushkin, R. S. Craxton, S. Oskoui, M. J. Guardalben, R. L. Keck, and W. Seka, Opt. Lett. **23**, 927 (1998).

8. A. Babushkin, W. Bittle, S. A. Letzring, A. Okishev, M. D. Skeldon, and W. Seka, in *Advanced Solid-State Lasers*, edited by C. R. Pollock and W. R. Bosenberg, OSA Trends in Optics and Photonics Series, Vol. 10 (Optical Society of America, Washington, DC, 1997), pp. 106–108.

9. W. L. Smith and T. F. Deaton, *Laser Program Annual Report 1979*, Lawrence Livermore National Laboratory, Livermore, CA, UCRL-50021-79, 2-209 (1980).

Ultrahigh Dynamic Range Measurement of High-Contrast Pulses Using a Second-Order Autocorrelator

In high-intensity, ultrafast laser–plasma interactions with solid targets, the intensity of prepulses with a typical time duration of ~1 ns, arriving before the main laser pulse, must be less than ~10^{10} W/cm^2 to avoid having the high-intensity pulse interact with a preformed plasma.[1,2] Currently, the highest available peak laser intensities are ~5×10^{19} W/cm^2 with 30-fs pulses[3] for small-scale laboratory lasers and 10^{21} W/cm^2 with 500-fs pulses on a large-laboratory scale.[4] The development of optical parametric chirped-pulse amplification[5] may allow the construction of small-laboratory-scale, truly tabletop subpetawatt lasers with peak intensities in the range of 10^{21} to 10^{23} W/cm^2;[6] therefore, the dynamic range of temporal pulse measurements must exceed ~10^{12} to predict if, where, and when a preformed plasma will be produced. Detailed knowledge of the temporal shape of the pulse is crucial to the study of high-density plasma physics.[7] The interaction of a high-contrast pulse with a high-density solid target or a high-density plasma is completely different from that of a low-contrast pulse. In particular, efficient production of the ultrafast x-ray emission[8,9] may require a high-contrast pulse.[10]

In some cases the intense pulse will contain a long, low-contrast prepulse with known temporal shape. The temporal shape of this prepulse must be known since it will affect the outcome of the interaction. At 10^{21} W/cm^2 intensities, a prepulse at the level of ~10^{-12} below peak intensity produces a preformed plasma, while one at the 0.1% level of peak intensity can ionize atoms and ponderomotively accelerate electrons out of the focus before the main pulse arrives. A pulse of this kind is used in the fast ignitor,[11] where a long, low-contrast (~10^{-3} below peak intensity) prepulse bores a hole for the main pulse. The temporal history of the prepulse will critically affect the propagation of the intense laser pulse in a large-scale coronal plasma and the energy deposition process in the overdense region.

With current state-of-the-art, ultrashort, high-peak-intensity lasers, the ideal device for measuring the temporal profile of the pulse would be a device with temporal resolution of tens of femtoseconds and a dynamic range of 10^{12}.

Devices simultaneously possessing subpicosecond resolution and high dynamic detection range are noncollinear beam correlators based on frequency conversion. The pulse to be measured is split into two parts, one of which may be delayed by the time delay τ, attenuated, and perhaps modified in frequency. The two parts are recombined in a nonlinear medium. In high-dynamic-range autocorrelation (HDRA), the sum frequency is generated noncollinearly to avoid the direct exposure of the detector by each individual beam. In second-order (SO) HDRA, where the noncollinearly recombined replicas of the beam are identical, the second-harmonic energy $E_{2\omega}(\tau)$ as a function of delay is proportional to the second-order intensity correlation function[12] (autocorrelation function):

$$E_{2\omega}(\tau) \propto G^{(2)}(\tau) \propto \int I(t)\, I(t - \tau)\, dt,$$

where $I(t)$ is the intensity.

In third-order (TO) HDRA, one beam is frequency doubled before noncollinear recombination, and the resulting third-harmonic signal $E_{3\omega}(\tau)$ is proportional to the third-order intensity correlation function[13]

$$E_{3\omega}(\tau) \propto G^{(3)}(\tau) \propto \int I(t)\, I^2(t - \tau)\, dt.$$

The advantages of SO over TO HDRA are simplicity, longer wavelength of the recorded signal, and better temporal resolution. Deteriorated temporal resolution in TO HDRA can be due to the limited acceptance bandwidth of the tripler[14,15] and, for shorter pulses (~100 fs and shorter), due to the dispersion of the pulse in the doubler or relay optics of autocorrelator.[3,15] The main advantage of TO over SO HDRA is that it can distinguish prepulses from postpulses.

The required proportionality of $E_{2\omega}(\tau)$ on the square of the incident intensity, $E_{2\omega}(\tau = 0) \propto (I_\omega)^2$, is satisfied over many orders of magnitude of incident intensities, so no

modification in the optical part of the autocorrelator or in the attenuation of the input beam is required when the delay τ is increased. A square-law, slow detector (with nanosecond resolution) is usually attenuated with calibrated filters to keep the noncollinear, sum-frequency signal at approximately the same level. In addition, the detected signal can be electronically time gated (on a time scale of ~10 ns) to minimize any extraneous noise associated with long-time-scale optical or electrical background.

Ultrafast pin diodes or streak cameras possess neither the required temporal resolution nor the required high dynamic range. The typical dynamic range of a streak camera with picosecond resolution is 100. It can be boosted to 10^7 by nonlinear shutters, by operating at lower temporal resolutions, and, for stable laser systems, by averaging over many laser shots.[16] The main disadvantage of correlators is that they are an indirect method of detection, i.e., the transformation of the signal from $I(t)$ to $G^{(2)}(\tau)$ occurs nonlinearly, allowing the existence of multiple solutions during reconstruction of the primary signal from the correlation signal. Both streak cameras and autocorrelators lose important temporal-phase information of the pulse. Recently, several methods have been developed to completely characterize ultrashort pulses, i.e., to obtain the temporal-phase and intensity information about the most intense portion of the beam. This is done with autocorrelators that frequency resolve the autocorrelation signal. The single-shot technique, which is able to completely characterize the most intense portion of the pulse, such as frequency-resolved optical gating (FROG),[17] is well developed with SO and TO noncollinear autocorrelators. These techniques, however, have not demonstrated a dynamic range approaching 10^{12}.

For ultrashort intense pulses, it is necessary to perform additional high-contrast autocorrelation to obtain information about the temporal-energy distribution outside the most intense portion. In this article, we perform only high-contrast autocorrelation measurements, although the autocorrelator used is "FROG-ready" and can work in the single-shot regime if the on-crystal focusing lenses are removed. The phase-sensitive measurements were not performed because the measured pulse was close to its bandwidth limit.

Noncollinear Autocorrelator for Temporal-Pulse-Shape Measurements

The z coordinate (transverse) of the spatial profile of the wide second-harmonic (SH) beam[18,19] or third-harmonic beam[15] may be linearly mapped to the delay τ to obtain the corresponding autocorrelation function in a single shot, as shown on Fig. 75.8. Figure 75.8 illustrates type-I noncollinear phase matching for two wide beams of diameter D, represented by ordinary waves with carrier frequency ω, (o,ω) propagating in a doubling crystal with thickness L_c at angle Φ with respect to each other. The direction of the noncollinearly generated second-harmonic extraordinary $(e,2\omega)$ beam is determined by the phase-matching condition, $\vec{k}_{0_1,\omega} + \vec{k}_{0_2,\omega} = \vec{k}_{e,2\omega}$. To maintain the correspondence between the transverse signal profile $S_{2\omega}(z)$ and the autocorrelation function $G^{(2)}(\tau)$ over the most intense temporal portion of the pulse, the transverse sizes (D) of the interacting beams should be large to avoid distorting the shape of the SH beam due to the spatial shape of the fundamental beam. The following two conditions should be satisfied: the spatial walk-off of each beam along the z coordinate in the thickness of the crystal, $L_c \tan(\Phi/2)$, should be at least three times smaller than the beam diameter size along the z direction, $D\cos(\Phi/2)$, giving $L_c \tan(\Phi/2) \lesssim (D/3)\cos(\Phi/2)$, and the size of the interaction region (diamond-shaped region in Fig. 75.8) should be at least three times smaller than the transverse size of the beam D, giving $L_p / \tan(\Phi/2) \lesssim D/3$. $L_p \approx (c/n_{o,\omega})\tau_p$ is the physical length of the pulse inside the crystal, c is the speed of light, $n_{o,\omega}$ is the index of refraction, and

E9152
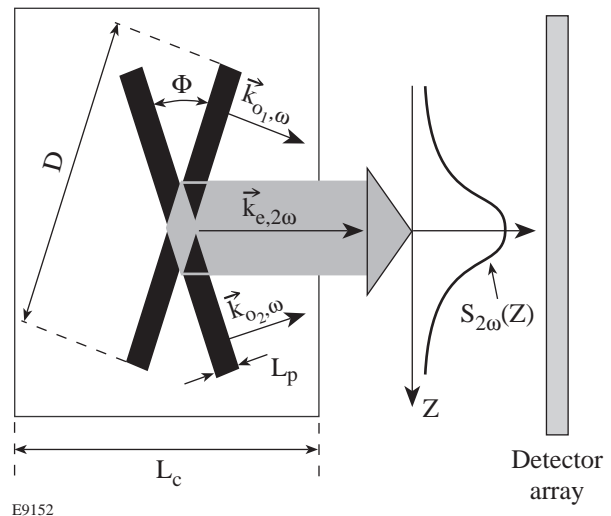
Figure 75.8
Single-shot setup for the noncollinear second-order autocorrelator. Two wide, ordinary beams with k-vectors $\vec{k}_{o_1,\omega}$ and $\vec{k}_{o_2,\omega}$, propagating in the nonlinear crystal at angle Φ with respect to each other, create a second-harmonic beam $\vec{k}_{e,2\omega}$. The width of the generated second-harmonic beam depends only on the duration of the pulses if beam diameters D are large. The shape of the second-harmonic beam, which is proportional to the second-order autocorrelation function $G^{(2)}(\tau)$, is recorded with a linear detector array.

τ_p is the pulse duration. The single-shot setup is limited to an ~10- to 100-ps range of delays (τ), due to the finite sizes of the crossing beams and/or the nonlinear crystal,[14] and to a dynamic range of ~10^6 to 10^7.[15,20] The finite dynamic range is due to the scattering of the intense portions of the noncollinearly generated beam into low-intensity portions.

To obtain a higher dynamic range with a delay of hundreds of picoseconds, one must work in the scanning regime when only one point of autocorrelation function (one τ) is recorded during a single shot. This is shown in Fig. 75.9, where the linear detector array is replaced by a single-point detector. In an experiment, the averaged autocorrelation function

$$\overline{G}(\tau, \Delta\tau) = \frac{1}{\Delta\tau} \int_{\tau-\Delta\tau/2}^{\tau+\Delta\tau/2} G(\tau') d\tau'$$

is recorded, instead of $G(\tau)$, due to finite sizes of the crossing beams. To avoid the effect of averaging $\overline{G(\tau)} = G(\tau)$, the transverse beam sizes at the intersection point inside the crystal must be reduced to one-third of the beam size obtained in a single-shot setup, or the time window determined by the crossing beams must be less than approximately one-tenth of

the pulse duration $\Delta\tau \lesssim \tau_p/10$. Figure 75.9 can be compared to Fig. 75.8. In Fig. 75.9, the beam diameters are reduced by a factor of 10, and, consequently, the z width of the SH beam is reduced by factor of 3 with respect to the original single-shot size. The transverse size $D = 2w_0$ of the crossing beams should satisfy $D / \{L_p / \sin(\Phi/2)\} \lesssim 0.3$. The sizes of the beams and their crossing angle will define the temporal resolution

$$\Delta\tau \approx (1.2/\gamma)(Dn_{o,\omega}/c)\tan(\Phi/2), \tag{1}$$

where γ is the form factor relating the FWHM of $I(t)$ to that of $G^{(2)}(\tau)$.

For ~100-fs and shorter pulses, dispersion may be a factor in the temporal resolution, or more correctly, dispersion will affect the width of the measured autocorrelation function because the lengths of interacting pulses, L_p, will be different upon arrival at the interaction point.

In the case of the finite transverse width of the probe pulse and negligible dispersion, the recorded autocorrelation function is proportional to the pulse shape $G(t) \propto I_\omega(t)$ at all times where $I_\omega(t)$ changes slowly, i.e., far from the most intense
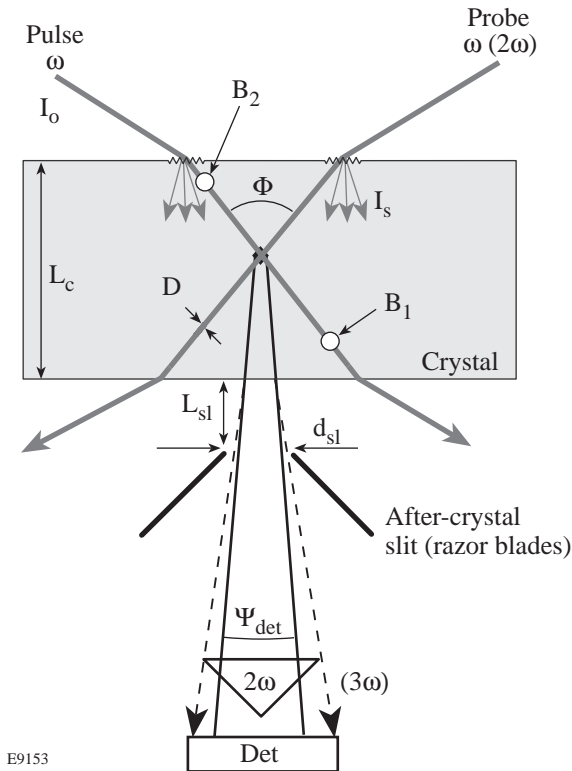
Figure 75.9
Geometry of the crossing beams in a noncollinear scanning autocorrelator. Two focused beams cross inside the crystal and generate the sum-frequency signal noncollinearly. For a particular delay between the pulse and the probe beams, the energy generated in the interaction region is proportional to the autocorrelation function. This geometry gives only one point of the auto-correlation function for a particular delay between the two beams (scanning regime) but allows one to obtain the higher dynamic range required for measurements of intense, ultrashort pulses. The light scattered from the first surface I_s (shown with arrows originating from the rough surface) can be frequency doubled during propagation through the bulk of the crystal and can reach the detector. An after-crystal slit is installed to reduce it. Each individual beam can be frequency converted along the passage through the crystal and then can scatter into the direction of the detector, producing a delay-independent background. We assume that only some portion of the beam path between points B_1 and B_2 is visible from the detector due to the presence of the after-crystal slit. We refer to this type of background as bulk-scattering noise.

region. The most intense portion is modified due to the autocorrelation transformation [integration of $I(t)I(t-\tau)$]. For example, for the temporal Gaussian/sech^2 pulse shape of $I(t)$ with a symmetric low-intensity pedestal, the $G^{(2)}(\tau)$ is 1.4 to 1.5 times wider than $I(t)$ and gives a pedestal intensity that is overestimated by factor of 2.8 to 3.

In several previous works, authors have measured 0.1- to 1-ps pulses with SO HDRA[21–25] with dynamic ranges of 10^5 to 10^8 and with TO HDRA[26–31] with dynamic ranges of 10^6 to 10^8. In two works,[3,13] the dynamic range with a TO autocorrelator is up to 10^{10} for 10-ps and 30-fs pulses with a temporal resolution of ~1 ps and ~0.1 ps, respectively (affected by dispersion). In the latter reference, the recorded autocorrelation function does not follow $G^{(3)}(\tau)$ over the most intense portion of the pulse, and additional second-order, single-shot, low-contrast autocorrelation is performed to complement the high-contrast measurements. In all of the cited references, there were no estimates of the factors that limit the available dynamic range.

In modern short-pulse laser systems, a contrast measurement of 10^8 may be insufficient. In a conventional CPA laser system, where a nanojoule-level oscillator determines the high-dynamic-range structure of the pulse, the contrast of optical background is ~10^8 or lower.[32–35] This optical background usually propagates through the CPA system and is present in the final amplified and compressed pulse. In addition, after stretching and relay losses, the amplified pulse may acquire a background associated with the amplified spontaneous emission (ASE) of the amplifier itself. As a rule of thumb, the contrast of the compressed pulse resulting from ASE noise of an amplifier can be expressed as the number of injected photons within the gain-narrowed spectrum, if the injected-pulse spectrum is wider than the gain-narrowed spectrum supported by this amplifier. Typically, with a pulse energy of ~100 pJ injected into the first regenerative or multipass amplifier, the ASE background may be of the order of 10^{-8} below the peak intensity in the compressed pulse.

In the case of insufficient pulse contrast, several schemes have been proposed to increase it. These include the use of the nonlinear birefringence of the fibers,[32] Pockels cells,[20] saturable absorbers,[21] frequency doubling of the amplified pulse,[36,37] degenerate optical parametric amplification (OPA),[38] amplification based on stimulated Raman scattering,[39] and self-induced plasma shuttering.[23] Using feedback-controlled mode-locked (FCM) lasers[40] with a saturable absorber inside the cavity makes it possible to create 1-ps pulses with ~10^8

contrast and ~1-μJ energy,[27] which effectively nullifies the influence of ASE of subsequent amplifiers to the level of 10^{-12}. For OPA CPA,[5] where co-propagating amplified and pumped pulses are timed and matched in duration, the long-duration ASE noise does not exist, due to the absence of an inverted medium. In many of the above-mentioned, experimentally realized schemes, the estimated contrast of picosecond and shorter pulses may be higher than 10^{12} but has not been measured.[36–39]

We have analyzed the factors that limit the dynamic range of the noncollinear autocorrelators and have systematically minimized them. The main physical factors are the finite energy of the pulse, scattering from the surface of the crystal, and bulk scattering. Minimizing or eliminating noise resulting from these factors dictates the geometry of the crossing beams in the autocorrelator and the size and quality of the crystal for a given pulse duration. Our estimate for the dynamic range is carried out for SO HDRA but can be applied to TO HDRA as well because both use the second-order nonlinearity $\chi^{(2)}$ of the medium [a cascaded $\chi^{(2)}:\chi^{(2)}$ process in the case of TO autocorrelation measurements] to produce the noncollinear signal.

The dynamic range of the autocorrelator can be conveniently defined as the ratio of the noncollinear signal at zero delay ($\tau = 0$) to the sum of signals E_1 and E_2 due to each beam, one at a time, sensed by the detector when the other beam is blocked:

$$DR = E_{nc}(\tau = 0)/(E_1 + E_2). \qquad (2)$$

This definition is independent of the temporal pulse shape and beam delay. Here E_{nc}, E_1, and E_2 are the energies that reach a detector from the noncollinear signal at zero delay and from each individual beam, respectively. It is assumed that E_1, $E_2 \ll E_{nc}$, and that the detector is frequency filtered to detect only the sum of the frequencies. The noise signals E_1 and E_2 reaching the detector can be scaled according to the second-harmonic-generation (SHG) equation[41] with additional spatial averaging into the detector:

$$E_{1,2} \propto I_{1,2}(2\omega) \propto \int d_{eff}^2 L^2 \, sinc^2\left[\frac{\Delta k(\Omega)L}{2}\right]$$
$$I_{1,2}^2(\omega, \Omega) d\Omega_{det}. \qquad (3)$$

Here $sinc(x) = sin(x)/x$, $d\Omega_{det}$ is the solid angle subtended by the detector from a point in the interaction region, $I(\omega, \Omega)$ is the

fundamental harmonic intensity into the direction of the detector, L is the interaction length for SHG, Δk is the phase mismatch, and d_{eff} is standard shorthand for the effective second-order nonlinearity. Equation (3) assumes that the regions of the surface and of the bulk of the crystal traversed by the beams become weak secondary sources of light at the sum frequency (the frequency of noncollinear signal) due to the scattering followed by frequency conversion or due to the frequency conversion (of strong but SHG phase-mismatched beams) followed by scattering. The highly directional noncollinear (nc) signal is scaled with the same parameters:[18,42] $E_{\text{nc}} \propto d_{\text{eff,nc}}^2 L_{\text{nc}}^2 I_1 I_2$ (for $\Delta k = 0$). L_{nc} can be roughly estimated as the walk-off distance when one beam crosses the other. These equations allow an estimate of the amount of noncollinear signal produced by two beams and the background produced by each individual beam. With the known position of the entrance pupil of the detector and the scattering properties of the crystal, the noncollinear signal can be compared to the signal produced by the scattered light, and the dynamic range of the noncollinear autocorrelator can be estimated.

Finite Pulse Energy

When the energy of the amplified pulse exceeds several millijoules, the current state-of-the-art lasers can operate only at a low repetition rate—typically 1 to 10 Hz for the first amplification stage and less for the second and higher stages. In this case, a multipulse averaging technique (such as lock-in detection) is impossible. A detector signal corresponding to below 1 photon per pulse in the incident radiation is not practically extractable. If we assume that the equivalent noise level of the device is 10 photons per pulse, to obtain the dynamic range of 10^{12}, 10^{13} photons, or 3 μJ of energy, are required in the second-harmonic noncollinear signal at the peak ($\tau = 0$) for 1-μm fundamental light. The undepleted second-harmonic signal ($E_{\text{nc}} \propto I_1 I_2$) can be produced with ~10% efficiency; hence, a 30-μJ pulse is required at the entrance to the crystal. For high-repetition-rate lasers, such as oscillators, lock-in detection can reduce requirements for the energy of individual pulses by 3 or more orders of magnitude. For example, several types of ultrashort-pulse oscillators, with individual-pulse energy in the range of 1 nJ, have been characterized with dynamic ranges of 10^8.[32–35]

Surface Scattering

Light scatters from a rough surface according to[43]

$$\frac{I_s}{I_0} = \left(\frac{4\pi\delta}{\lambda}\right)^2, \tag{4}$$

where I_0 and I_s are the incident and scattered intensities, λ is the wavelength of the incident radiation, and δ is the rms surface roughness. Equation (4) is valid for near-normal incidence and relatively smooth surfaces, $\delta \ll \lambda$. It is assumed that light scatters from the surface isotropically. With typical numbers $\delta \approx 50$ Å and $\lambda = 1$ μm, we find $I_s/I_0 = 0.4\%$, which is very high. The fundamental light scattered from the surface can propagate through the crystal, be frequency doubled, and reach the detector, shown in Fig. 75.9 as arrows originating from the rough surface. The detector is assumed to be blocked against the fundamental light. Using the scaling of Eq. (3) with $I(\omega, \Omega) = (1/4\pi)I_s$, $d\Omega_{\text{det}} \approx 10^{-2}$ steradians, a mismatch factor $\text{sinc}^2(\Delta k L_c/2) \approx 10^{-5}$, and the SHG length of the surface-scattered noise equal to the crystal bulk length $L_c \left[L_{\text{scat}} = L_c \sim 1 \text{ mm} \left(L_{\text{scat}}/L_{\text{nc}} \approx 10 \right) \right]$, the signal-to-noise level is approximately 10^8. This is about three to four orders of magnitude lower than required. The scattering in a particular direction can be enhanced if the surface is manufactured with a characteristic roughness period, which acts as a diffraction grating.

To reduce the surface-scattering effects, an aperture or slit can be placed just after the crystal to block the surface-scattered light from entering the detector. We refer to this slit as an "after-crystal" slit (see Fig. 75.9). It is evident that this is more effective at higher crossing angles, with smaller entrance-pupil angles of the detector, and/or with thicker crystals. For the two beams crossing halfway in the bulk of the crystal, the condition for reducing surface-scattering noise can be stated as follows: an observer at the detector should not see regions where the interacting beam hits the surface, or the backward image of the detector entrance-pupil angle onto the first surface of the crystal should be within the "dark area" (see Fig. 75.9),

$$d_{\text{sl}} + \Psi_{\text{det}}\left(L_{\text{sl}} + L_c/n_{2\omega}^e\right)$$
$$< L_c \tan(\Phi/2) - 6w_0/\cos(\Phi_{\text{air}}/2). \tag{5}$$

The left-hand side of Eq. (5) is the size of the backward image of the detector onto the first surface of the crystal with slit size d_{sl}, crystal thickness L_c, and distance from second surface of the detector to the slit, L_{sl}. The right-hand side is the size of the "dark area" on the first surface of the crystal where the two beams, with waist size w_0, separated by the distance $L_c \tan(\Phi/2)$, are attenuated to $10^{-8} I_0$. This is due to the phase-matching and intensity effects on the conversion efficiency. Equation (5) determines the minimum crossing angle or

thickness of the crystal for efficient surface-noise filtering. It also fixes the optimal linear size of the detector Ψ_{det} in the crossing plane. The other dimension of the detector is determined purely by the divergence of the noncollinear SHG beam. To maximize the dynamic range, we must choose Ψ_{det} to be approximately equal to the divergence of the noncollinear SH beam, assuming that the detector is in the far field.

The following factors should be considered simultaneously with Eq. (5):

1. The size of the fundamental beams determines the resolution of the autocorrelator, the size of the SHG beam, and the size of the after-crystal slit.

2. The crossing angles are limited by the finite birefringence of the crystal. For example, for $\lambda = 1\ \mu$m, the maximum crossing angle for $LiIO_3$ and BBO is 39°, while for KDP it is 20°.

3. The closer the slit is to the crystal, the better. The razor blades are positioned at an angle with respect to each other that minimizes L_{sl} while keeping the area of contact of the razor blade with the crystal as small as possible. Another reason for such positioning is to avoid blocking each fundamental beam because backwardly reflected light may give additional background.

4. Smaller waists $\left\{ w_0 = D/2 \ll 0.3 L_p \left/ \left[2 \sin(\Phi/2) \right] \right. \right\}$ are impractical because the SHG conversion efficiency will decrease due to the reduced interaction length. Tighter focusing would require higher intensities to keep the energy of the noncollinear signal at the same level, which could result in damage or saturation of the crystal.

The following example illustrates these constraints. Focusing two identical $w_0 = 2$ mm beams with $f = 250$ mm lenses into a noncritically phase-matched $LiIO_3$ crystal (maximum possible $\Phi = 39.5°$) with $L_c = 5$ mm will produce a second-harmonic beam with size $w_{0,2\omega} \approx 100\ \mu$m and divergence $\Psi_{2\omega}$ $\sim 10^{-2}$ rad. For 30-μJ total energy of the two beams, with $d_{eff,nc} = d_{31} = 4.2$ pm/V,[44] the estimated conversion efficiency will be $\sim$10%, giving the required $\sim$3 μJ per pulse of the noncollinear signal. The corresponding peak intensity of each fundamental beam will be $\sim$500 GW/cm^2 for a 1-ps pulse duration. For a crystal–slit separation $L_{sl} = 10$ mm, one needs a slit width $d_{sl} \approx 400\ \mu$m to transmit 99% of light and a linear angular size of the detector $\Psi_{det} \approx 3\Psi_{2\omega} \approx 3 \times 10^{-2}$ rad. The other linear angular size of the detector in the plane perpendicular to the

crossing plane is approximately the same and is determined by the divergence of the SH beam. This gives a 340-μm size of the backward image of the detector onto the first surface of the crystal and the size of the "dark area" as 600 μm. A 2- to 3-mm-thick crystal is required to efficiently filter the surface-scattering noise. With a low-birefringence crystal such as KDP ($\Phi_{max} \approx 20°$), a 6- to 8-mm-thick noncollinear crystal is required to satisfy Eq. (4) and to filter out the surface-scattering noise. In all previously reported SO HDRA's utilizing a nonlinear crystal for frequency conversion,[21–25] the dynamic range at the level of 10^8 to 10^9 was probably limited by surface scattering.

Bulk Scattering

Bulk scattering is always present in the background and presents the fundamental limitation to the dynamic range of the autocorrelator. Each beam propagating through the crystal can be scattered into the direction of the detector and converted to SH noise or can be converted to the SH and then scattered. The latter process is more probable because the scattering is inversely proportional to the fourth power of wavelength $R \propto 1/\lambda^4$. R, expressed in cm^{-1}sr^{-1}, is the bulk-scattering intensity ratio I_s/I_0 per unit length traveled in the bulk of a solid material per unit solid angle. Bulk scattering depends on the macroscopic index-of-refraction inhomogeneities of a dielectric, Δn,[45]

$$ R = \frac{C}{\lambda^4} (\Delta n)^2 , \tag{6} $$

where λ is expressed in μm and $C \approx (2 \text{ to } 4) \times 10^3\ \mu$m^4 cm sr^{-1}. The angular and polarization dependence of the scattered light is omitted for the purposes of these estimates. Well-manufactured amorphous glasses have $\Delta n \approx 10^{-4}$–10^{-5} cm^{-1} and follow the λ^{-4} laws.[46] Good-quality optical crystals may have $\Delta n \approx 10^{-6}$ cm^{-1} and $R \approx 10^{-8}$ for visible light. For the smaller bulk-scattering ratios ($R \leq 10^{-8}$–10^{-9} cm^{-1} sr^{-1}), the scattering from a single molecule can be comparable to the scattering from macroscopic inhomogeneities.

Here we describe the level of noise scattered into the detector from a single beam converted to the second harmonic and then scattered. We assume that SHG occurs over a 1-mm length along the k-vectors ($\vec{k}_{o_1,\omega}$ and $\vec{k}_{o_2,\omega}$) of the beams. This gives the ratio of the bulk-generated to noncollinearly generated intensities:

$$ I_{2\omega,\text{bulk}} \left/ I_{2\omega,\text{nc}} = \left(L_{\text{bulk}} / L_{\text{nc}} \right)^2 \text{sinc}^2 \left(\Delta k L_{\text{bulk}} / 2 \right) \approx 10^{-3} \right. . $$

Taking $\Delta n \sim 10^{-5}$ cm^{-1} gives $R_0 = 10^{-7}$ for $\lambda = 0.5$ μm. The highly fluctuating function $\text{sinc}^2(x)$ may be replaced on average with $1/2x^2$. With the solid angle of the detector $d\Omega_{\text{det}} \approx 10^{-2}$ steradian, the fraction $R_0 L_{\text{im}} d\Omega_{\text{det}} \approx 10^{-10}$ of the light will be scattered into the direction of the detector, giving background noise at the level $10^{-3} \times 10^{-10} = 10^{-13}$. Here, $L_{\text{im}} \sim$ 1 mm is the length of the path of the single beam inside the crystal, which is visible from the detector as shown in Fig. 75.9 with end points B_1 and B_2 and with $L_{\text{im}} = |B_1 - B_2|$. This path segment is the secondary source of SHG noise, which creates delay-independent background into the detector. The non-collinear signal will be $\sim 5 \times 10^{12}$ times stronger than the bulk-scattering signal.

Here we discuss the bulk-noise level into the detector in the case where the fundamental beam first scatters in the bulk and where the scattered portion is converted into the second harmonic. The portion of the fundamental harmonic scattered into the direction of the detector from the segment path $[B_1 B_2]$ is $(R_0/16)$ $L_{\text{im}} d\Omega_{\text{det}} \approx 10^{-11}$. The SHG (even perfectly phase matched) is the square of this expression. Even if the SHG length of this scattered beam is an order of magnitude higher than the effective SHG length of the main noncollinear signal, the estimated dynamic range is $\sim 10^{18}$, making this scattering process negligible.

Portions of the individual beams directly converted into the second harmonic and then scattered into the direction of the detector limit the dynamic range of the autocorrelator to the level of 5×10^{12} with the refractive bulk inhomogeneities in the 1-mm-thick crystal at the level of $\Delta n \sim 10^{-5}$ cm^{-1}.

Experimental Setup and Results

The experimental setup is shown in Fig. 75.10. The high-contrast pulse is generated in a chirped-pulse-amplification (CPA) system utilizing a chirping fiber. The system consists of
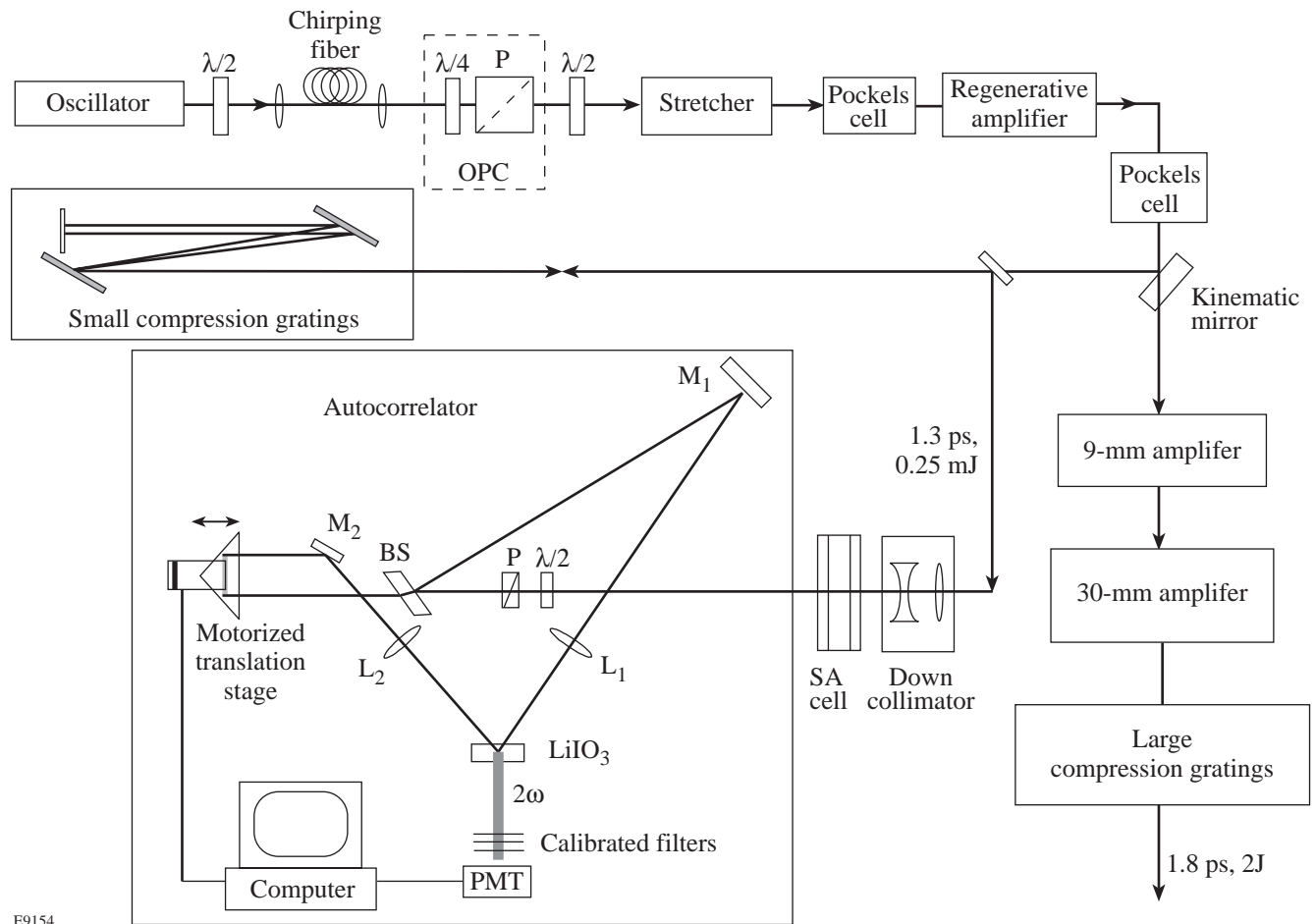

Figure 75.10
Experimental setup for production and measurement of ultrahigh-contrast, 1-ps pulses. OPC: the optical pulse cleaner; P: polarizer; $\lambda/2$ and $\lambda/4$: half- and quarter-wave plates, respectively; BS: beam splitter; M_1 and M_2: mirrors; L_1 and L_2: on-crystal focusing lenses; and PMT: photomultiplier tube.

a Nd:YLF oscillator followed by a fiber, a stretcher, three amplification stages, and a grating compressor. The pulse train from the Nd:YLF oscillator[47] is made up of 100-MHz, 45-ps bandwidth-limited pulses at a wavelength of 1053 nm. These pulses pass through an 800-m-long, single-mode optical fiber, which imposes a frequency chirp on the pulse with a bandwidth of up to 40 Å. A grating stretcher is then used to expand the pulse to 450 ps. After the stretcher, one pulse is selected with a Pockels cell for amplification.

The chirped pulse is amplified in three stages. All three amplifiers are flash-lamp-pumped, water-cooled rod amplifiers that have Nd^{3+}:glass as an active host. The first stage is a non-cavity-dumped, linear regenerative amplifier,[21,48] which provides most of the gain. It operates at a 1-Hz repetition rate. After about 85 passes, one pulse from the regenerative amplifier train with an output energy of ~0.5 mJ is switched out on the leading edge of the pulse-train envelope. The total cumulative B-integral of this pulse is ~0.7. This pulse then passes through a 9-mm-diam rod amplifier where its energy is raised to ~60 mJ. The 9-mm rod amplifier amplifies the pulse in one, two, or three passes. The energy of the pulse can be further boosted by 50 times in the third stage with a single-pass, 30-mm rod amplifier. The amplified pulse is compressed with a pair of compression gratings. The energetic parameters of the CPA system are listed in Table 75.II. When compressed, 1.6-ps pulses can carry energies in excess of 2 J and can be focused onto a target with peak intensities up to 10^{19} W/cm^2.

The amplified compressed pulse exhibits a pedestal consisting of two broad, equal-intensity satellite pulses separated from the main pulse by ~60 ps, as shown in Fig. 75.11, curve (a), with solid circles. The existence of two symmetric satellites was ascertained by performing TO HDRA measurements.[21] Their origin is the overlaid pedestal from the oscillator[13] and uncompensated phase distortions from the chirping fiber. The satellites and long pedestal can be suppressed by two and one-half orders of magnitude by using optical pulse cleaning (OPC) with the nonlinear birefringence of the chirping fiber.[49,50] A quarter-wave plate and a polarizer are inserted, as in Ref. 51, rather than an additional fiber, as in Ref. 32 (Fig. 75.10). The half-wave plate after the OPC is used to restore the polarization necessary for the grating stretcher. The spectrum leaving the chirping fiber was substantially reshaped, as shown in Fig. 75.12. The original spectrum, leaving the fiber without a quarter-wave plate is shown with a solid line. It has peaks at ±20 Å from the central frequency and two wave-breaking sidelobes[52] at ±30 Å. After rotating the wave plate and polarizer for maximum rejection of low-intensity light and maximum transmission of high-intensity light, the spectrum became centrally peaked with reduced peaks at ±20 Å and completely eliminated side lobes, as shown with the dashed line in Fig. 75.12. The spectral intensity of the amplified spectrum is primarily determined by the gain-narrowing in the regenerative amplifier and is almost independent of the injected spectrum. The pulses with contrast improved by OPC are shown in Fig. 75.11 with open diamonds. The seed energy contained within the shape of gain-narrowed spectrum is ~5 pJ. This imposes an ASE background with contrast ~10^7 when the pulse is compressed, as seen in Fig. 75.11 [curve (b)] for delays $\tau \geq 130$ ps. This background is very sensitive to the alignment of the seed and can be increased by one or two orders of magnitude by a slight mispointing of the seed pulse. The inset in Fig. 75.11 shows the amplified spectrum (solid curve) corresponding to the autocorrelation data (a) and the spectrum after OPC (dashed curve) corresponding to the autocorrelation data (b). The spectral width of the amplified OPC-modified pulse was 11.5 Å (FWHM), with the shape close to Gaussian. With a form factor $\gamma = 1.4$, the autocorrelation measurement gives a pulse duration of 1.4 ps and a corresponding time-bandwidth product of 0.44.

Table 75.II: Parameters of the CPA system

	In	Out	Total gain (gain in the active host)	Peak fluence	Output spectrum	B-integral
Oscillator		1 nJ/45 ps		–	0.4 Å	
Fiber	1 nJ	0.3 nJ/150 ps	0.5	–	30 Å	~100
Regenerative amplifier	3 pJ/450 ps	0.5 mJ/150 ps	10^{36}	0.1 J/cm^2	12 Å	0.7
9-mm amplifier (three passes)	0.3 mJ	60 mJ	400	0.1 J/cm^2	12 Å	0.2
30-mm amplifier	40 mJ	2 J	50	0.5 J/cm^2	12 Å	0.6

The contrast of the amplified compressed pulses was further boosted by a fast saturable absorber (SA) cell.[21] The compressed pulse was down-collimated to a waist of 0.7 mm before the SA cell to obtain a peak fluence of 25 mJ/cm^2 with 1.4-ps, 0.25-mJ pulses. The SA was Kodak dye #9860 in nitrobenzene with molar concentrations (n_M) varying from 50 to 75 μM. The relaxation time of this SA is ~4.2 ps.[53] The thickness of the

cell was 1 cm, with ~12.5-mm wall thicknesses. Within the range of incident fluences between 0.01 and 20 mJ/cm^2, the incident-fluence-dependent absorption coefficient $[T = \exp(-\alpha L)]$, as measured with compressed 1.6-ps pulses, was

$$\alpha = \alpha_0 + \alpha_{sat}\left[1 + \left(J_{inc}/J_{sat}\right)^n\right]^{-1},$$
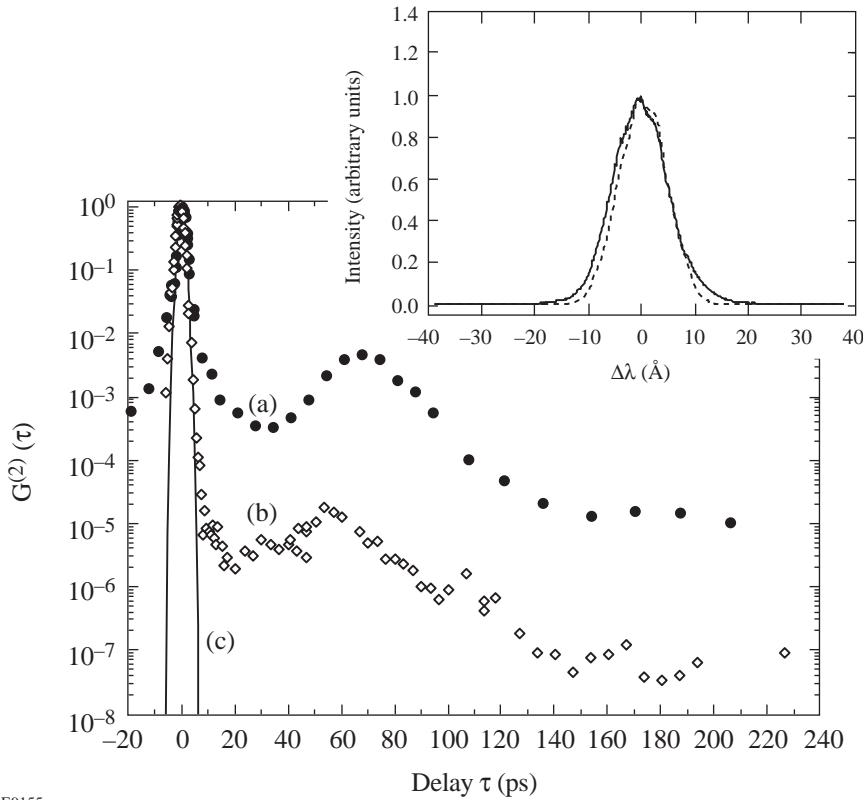
Figure 75.11
Normalized second-order autocorrelation functions of the compressed pulses leaving the regenerative amplifier: (a) original pulses, (b) OPC-cleaned pulses, and (c) the 1.4-ps Gaussian-curve fit to both of these autocorrelation functions. The origin of the pedestal and two symmetric satellites is the oscillator and the uncompensated (after compression with gratings) phase distortions from the chirping fiber. After OPC cleaning and amplification, the pedestal level is determined by the ASE from the regenerative amplifier, which is nearly equal in intensity to the residual pedestal from the oscillator and fiber.

E9155
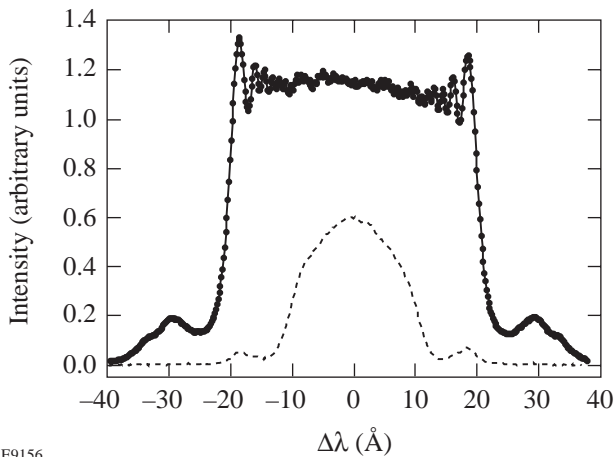
Figure 75.12
The spectrum leaving the chirping fiber. The spectrum measured without a quarter-wave in the OPC is shown with solid line. The OPC-cleaned spectrum is shown with dashed line.

E9156

with $\alpha_0/n_M = 0.02$ cm^{-1} μM^{-1}, $\alpha_{sat}/n_M = 0.16$ cm^{-1} μM^{-1}, $J_{sat} = 1.28\pm0.02$ mJ/cm^2, and $n = 1.50\pm0.04$. For incident fluences higher than ~30 mJ/cm^2, increased nonlinear absorption was observed instead of saturable absorption (decrease in transmission by 2%–3%). The operating incident intensity was chosen near 20 to 25 mJ/cm^2. The measured transmission of the cell was $\exp(-\alpha_0 L) = 22\%$ with a Kodak-dye concentration of ~75 μM, and the expected contrast boost was $\exp(\alpha_{sat}L) \sim 10^5$.

The autocorrelator was constructed as follows: A 10-mm × 10-mm, 4-mm-thick LiIO$_3$ crystal with rms surface roughness below 50 Å and bulk index-of-refraction inhomogeneities below 10^{-5} cm^{-1} was chosen as the noncollinear crystal. The two beams had a crossing angle $\Phi \approx 19°$ (~75° in the air). Without a down-collimator and on-crystal focusing lenses, the autocorrelator was used to measure the pulse duration in a single shot. The diameter of each individual beam was $2w_0 \sim 5.6$ mm. With a down-collimator before the saturable absorber cell and with the insertion of $f = 125$-mm lenses L_1 and L_2 (see Fig. 75.10), the two beams were focused onto the crystal with waist sizes of 40 μm. The crystal was cut for type-I noncritical phase matching. An after-crystal slit with a width of $d_{sl} \approx 300$ μm was placed $L_{sl} = 1$ mm behind the crystal, as shown in Fig. 75.9. The autocorrelator was carefully aligned with respect to any geometrical displacement of the probe beam inside the crystal when the translation stage is scanned. A photomultiplier tube (PMT), heavily filtered against the fundamental frequency and attenuated with variable-calibrated neutral-density filters to keep the signal on the same level, was used as the detector. The signal from the PMT was additionally time gated to avoid any noise associated with two-photon fluorescence, or any other long-time-scale optical noise. The signal from the PMT was an electrical pulse ~4 ns in duration. This electrical pulse was integrated within the gate time of 80 ns and converted into counts. One count from our acquisition system corresponded to 4 optical photons. The combined optical and electrical noise level with the PMT exposed to the experimental surroundings, without attenuating neutral-density filters and without blocking the noncollinear signal, was 2 counts.
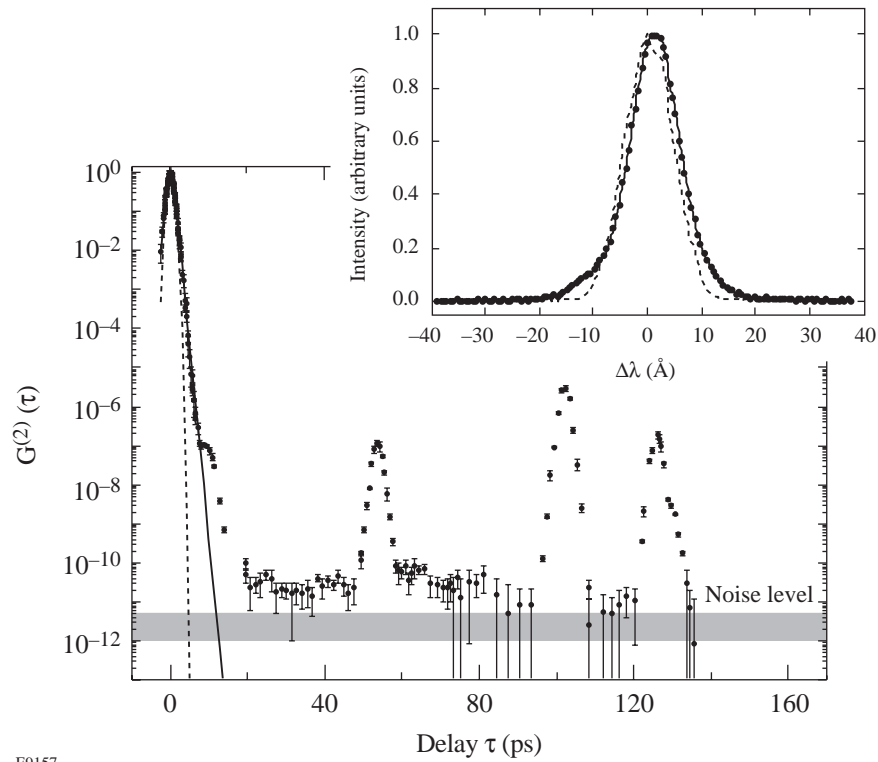
The second-order autocorrelation measurements of pulses cleaned with OPC and SA are shown in Fig. 75.13. Each point of the autocorrelation curve in Fig. 75.13 corresponds to an average of five laser shots. The inset shows the measured spectrum before and after the SA cell. From the spectral measurements, it can be seen that the B-integral accumulated in the SA cell is ~1. The estimated B-integral in the rest of the

autocorrelator optics is ~0.3. After transmission through the SA cell, the duration of the pulse was reduced from 1.4 ps to 1.0 ps. The peaks at 54, 100, and 125 ps are Fresnel reflections from optics in the autocorrelator. The pulse is measured to have an intensity contrast in excess of 10^{11}.

The dynamic range of the autocorrelator, measured as the ratio of the peak of the signal to the sum of the signals measured from each arm while the other arm was blocked, was 10^8 without the after-crystal slit and 10^{11} with it. Noise from each arm represented a constant addition to the signal, independent of the delay, but proportional to the square of the energy of the fundamental light at the input of the autocorrelator. That additional noise can be subtracted from the signal for each shot, leaving not the noise level from each arm, but rather the uncertainty of the noise level of each arm. The uncertainty of the noise level of each arm was 20% of the noise itself; thus, the system was able to resolve the signal with a dynamic range of 0.5×10^{12}. The signal at large delays was about twice as large as the noise.

The estimates based on the simple geometric layout shown in Fig. 75.9 with Gaussian beam profiles show that our approach can be applied to pulses as short as 100-fs duration. For pulses shorter than ~100 fs, both the geometry and the phase-matching conditions over the 10-nm spectrum may make it difficult to reduce the surface-scattering noise, which may decrease the dynamic range of an autocorrelator. The shorter pulses require higher temporal resolution (smaller $\Delta\tau$) and thus smaller crossing angles. Smaller crossing angles would require a longer crystal. Longer crystals would cause the distortion of the temporal shape of the pulse (due to material dispersion) before it reached the interaction region. Tighter focusing would bring noncollinear frequency conversion closer to saturation with lower energies of the crossing fundamental beams and would give smaller noncollinear beam energies. The after-crystal slit still might be a solution with 100-μm-thick crystals and tighter focusing for multikilohertz systems able to generate ~30-fs pulses[3] because one can utilize lock-in detection.

In conclusion, we have demonstrated for the first time second-order autocorrelation measurements of ultrashort picosecond pulses with dynamic ranges of ~0.5×10^{12}. To our knowledge, this is the highest dynamic range obtained in time-resolved dynamic-range measurements with tens-of-femtoseconds resolution. To our knowledge, this is also the first consideration of dynamic-range limitations for noncollinear, high-dynamic-range autocorrelation measurements.

E9157

Figure 75.13
Normalized second-order autocorrelation of the OPC-cleaned pulses (as shown in Fig. 75.11 with open diamonds) after transmission through the SA cell. A 10^{-12} signal corresponds to ~4 photons per shot. The final autocorrelation function has peaks at 54 ps, 100 ps, and 125 ps at a level of 10^{-5} to 10^{-6} below the peak intensity. These are Fresnel reflections in the autocorrelator optics and in the SA cell. The 54-ps peak is associated with the reflection from the 5-mm-thick non-wedged mirror (M_2 in Fig. 75.10) in the translation-stage arm. It can be eliminated by using a wedged mirror. The 100-ps peak is the secondary reflection in the plano-convex ($f = 125$ mm, thickness $= 10$ mm) on-crystal focusing lenses (L_1 and L_2 in Fig. 75.10). This expected peak was at a different position when focusing lenses with a different thickness were used. It can be reduced and eliminated by better coating and with a slight misalignment of the focusing lenses. The 125-ps peak is the Fresnel reflection from the 1/2-in.-thick wall of the second SA cell. It disappeared but was replaced by a similar peak at 10 ps when a SA cell with 1-mm-thick walls was used. The inset shows the intensity spectrum of the pulses before (dashed line) and after (solid line) transmission through a SA cell for incident fluences of ~25 mJ/cm^2. After transmission through the cell, the pulse duration decreased from 1.4 ps to 1.0 ps. The dashed and solid curves are, respectively, 1.0-ps Gaussian and sech^2 fits to this autocorrelation data.

REFERENCES

1. P. B. Corkum *et al.*, Phys. Rev. Lett. **61**, 2886 (1988).

2. B. C. Stuart *et al.*, Phys. Rev. B **53**, 1749 (1996).

3. A. Antonetti *et al.*, Appl. Phys. B **B65**, 197 (1997).

4. G. A. Mourou, C. P. J. Barty, and M. D. Perry, Phys. Today **51**, 22 (1998).

5. A. Galvanauskas *et al.*, Opt. Lett. **23**, 210 (1998).

6. I. N. Ross *et al.*, Opt. Commun. **144**, 125 (1997).

7. M. M. Murnane, H. C. Kapteyn, and R. W. Falcone, Phys. Rev. Lett. **62**, 155 (1989).

8. H. Chen, B. Soom, B. Yaakobi, S. Uchida, and D. D. Meyerhofer, Phys. Rev. Lett. **70**, 3431 (1993).

9. B. Soom, H. Chen, Y. Fisher, and D. D. Meyerhofer, J. Appl. Phys. **74**, 5372 (1993).

10. Throughout the text it is assumed that the contrast of some structure is the ratio of the peak intensity of the pulse to the intensity of this structure, while the intensity level of a structure is the inverse of the contrast.

11. M. Tabak *et al.*, Phys. Plasmas **1**, 1626 (1994).

12. E. P. Ippen and C. V. Shank, Appl. Phys. Lett. **27**, 488 (1975).

13. G. Albrecht, A. Antonetti, and G. Mourou, Opt. Commun. **40**, 59 (1981).

14. R. Wyatt and E. E. Marinero, Appl. Phys. **25**, 297 (1981).

15. P. Pax, J. Weston, and W. E. White, in *Femtosecond to Nanosecond High-Intensity Lasers and Applications*, edited by E. M. Campbell (SPIE, Bellingham, WA, 1990), Vol. 1229, pp. 82–86.

16. A.-C. Tien *et al.*, Opt. Lett. **22**, 1559 (1997).

17. R. Trebino and D. J. Kane, J. Opt. Soc. Am. A **10**, 1101 (1993).

18. J. Janszky, G. Corradi, and R. N. Gyuzalian, Opt. Commun. **23**, 293 (1977).

19. C. Kolmeder, W. Zinth, and W. Kaiser, Opt. Commun. **30**, 453 (1979).

20. K. Yamakawa *et al.*, Opt. Lett. **16**, 1593 (1991).

21. Y.-H. Chuang, D. D. Meyerhofer, S. Augst, H. Chen, J. Peatross, and S. Uchida, J. Opt. Soc. Am. B **8**, 1226 (1991).

22. L. Zhao *et al.*, in *Mode-Locked and Solid State Lasers, Amplifiers, and Applications*, edited by M. Piché and P. W. Pace (SPIE, Bellingham, WA, 1993), Vol. 2041, pp. 93–102.

23. D. M. Gold, Opt. Lett. **19**, 2006 (1994).

24. P. Beaud *et al.*, in *OSA Proceedings on Shortwavelength V: Physics with Intense Laser Pulses*, edited by M. D. Perry and P. B. Corkum (Optical Society of America, Washington, DC, 1993), Vol. 17, pp. 11–15.

25. O. A. Konoplev, Y. Fisher, and D. D. Meyerhofer, in *Conference on Lasers and Electro-Optics*, Vol. 15, 1995 OSA Technical Digest Series (Optical Society of America, Washington, DC, 1995), p. 216.

26. Y. Beaudoin *et al.*, Opt. Lett. **17**, 865 (1992).

27. R. S. Marjoribanks *et al.*, Opt. Lett. **18**, 361 (1993).

28. C. N. Danson *et al.*, Opt. Commun. **103**, 392 (1993).

29. C. Rouyer *et al.*, in *OSA Proceedings on Shortwavelength V: Physics with Intense Laser Pulses*, edited by M. D. Perry and P. B. Corkum (Optical Society of America, Washington, DC, 1993), Vol. 17, pp. 2–5.

30. M. P. Kalashnikov *et al.*, Phys. Rev. Lett. **73**, 260 (1994).

31. J. P. Chambaret *et al.*, Opt. Lett. **21**, 1921 (1996).

32. J.-L. Tapié and G. Mourou, Opt. Lett. **17**, 136 (1992).

33. P. F. Curley *et al.*, Opt. Commun. **120**, 71 (1995).

34. A. Braun *et al.*, Opt. Lett. **20**, 1889 (1995).

35. I. D. Jung *et al.*, Appl. Phys. B **B65**, 307 (1997).

36. K. Yamakawa *et al.*, IEEE J. Quantum Electron. **27**, 288 (1991).

37. C. Y. Chien, G. Korn, J. S. Coe, J. Squier, G. Mourou, and R. S. Craxton, Opt. Lett. **20**, 353 (1995).

38. Y. Wang and B. Luther-Davies, J. Opt. Soc. Am. B **11**, 1531 (1994).

39. L. L. Losev and V. I. Soskov, Opt. Commun. **135**, 71 (1997).

40. P. Heinz and A. Laubereau, J. Opt. Soc. Am. B **6**, 1574 (1989).

41. E. P. Ippen, and C. V. Shank, in *Ultrashort Light Pulses*, edited by S. L. Shapiro, Topics in Applied Physics, Vol. 18 (Springer-Verlag, Berlin, 1977), pp. 83–122.

42. S. Umegaki and S. Tanaka, Jpn. J. Appl. Phys. **16**, 775 (1977).

43. H. E. Bennett and J. O. Porteus, J. Opt. Soc. Am. **51**, 123 (1961).

44. D. A. Roberts, IEEE J. Quantum Electron. **28**, 2057 (1992).

45. L. D. Landau and E. M. Lifshitz, *Electrodynamics of Continuous Media*, Course of Theoretical Physics, Vol. 8 (Pergamon Press, Oxford, 1960), p. 385.

46. H. Bach and N. Neuroth, in *The Properties of Optical Glasses*, Schott Series on Glass and Glass Ceramics (Springer-Verlag, Berlin, 1995), p. 88.

47. P. Bado, M. Bouvier, and J. S. Coe, Opt. Lett. **12**, 319 (1987).

48. O. A. Konoplev and D. D. Meyerhofer, IEEE J. Sel. Top. Quantum Electron. **4**, 459 (1998).

49. R. H. Stolen, J. Botineau, and A. Ashkin, Opt. Lett. **7**, 512 (1982).

50. B. Nikolaus, D. Grischkowsky, and A. C. Balant, Opt. Lett. **8**, 189 (1983).

51. H. Roskos *et al.*, Opt. Commun. **61**, 81 (1987).

52. W. J. Tomlinson, R. H. Stolen, and A. M. Johnson, Opt. Lett. **10**, 457 (1985).

53. B. Kopainsky, W. Kaiser, and K. H. Drexhage, Opt. Commun. **32**, 451 (1980).

54. Y.-H. Chuang, J. Peatross, and D. D. Meyerhofer, in *Short-Pulse High-Intensity Lasers and Applications*, edited by H. A. Baldis (SPIE, Bellingham, WA, 1991), Vol. 1413, pp. 32–40.

Using Ion-Beam Techniques to Determine the Elemental Composition of ICF Targets

The precise elemental composition of any inertial confinement fusion (ICF) target (capsule, flat foil, or a package attached to a hohlraum) must be known to interpret the results of the implosion. The accuracy of this information was never an issue in earlier experiments: the composition was well known because the targets were straightforward designs (i.e., glass capsules and micro-encapsulated polystyrene shells) that were fabricated using well-characterized polymer chemistry methodologies that yield known compositions. Targets used today are more complicated than those used previously and are fabricated by new methods that are still in their infancy and, accordingly, are less understood.[1] These techniques involve the plasma-induced (a low-temperature, glow-discharge) polymerization of gas-phase monomers. The energy from the plasma and the presence of ions allow gas-phase and gas-surface interactions to occur that are otherwise unattainable using classical solvent chemistry because numerous reaction mechanisms are now thermodynamically and kinetically allowed. The resulting materials are amorphous solid-state solutions where the composition cannot be inferred *a priori* from the processing conditions. The overriding importance of this target-fabrication technique, however, is that thin-wall capsules, and capsules with discrete radial regions of the capsule wall doped with mid- to high-atomic-weight elements, can now be produced.[2] The associated uncertainty regarding the composition of these targets now requires the evaluation and application of suitable analysis techniques.

When a target is made of commercially available material, the material assay is accurately known. When targets are made using coating processes, only the composition of the source (precursor) material is well known; independent analysis of the as-deposited material is needed if the composition is to be accurately known. This analysis is done by many methods: The most common technique is electron microscopy using either energy-dispersive or wavelength-dispersive x-ray detection to identify the elements. These techniques are well established, and quantitative data can be obtained with the use of NIST standards. The diagnostic probe size is small (typically <1-μm diameter, 5 μm deep) and nondestructive, features that are desirable for analyzing ICF targets. Another technique adapted for ICF-sized shells—x-ray fluorescence—is also nondestructive and is used to identify dopants (chlorine, titanium, germanium, silicon) in individual shells according to their characteristic x-ray emission signal.[3] Carbon, hydrogen, oxygen, and nitrogen cannot be detected. Again, the actual elemental composition can be quantified if a suitable external calibration of the technique can be established. The techniques discussed here provide a third nondestructive method for assaying individual capsules, with the added virtue that they do not require external calibration. This eliminates several sources of uncertainty in the measurement.

In this article the capabilities and limitations of the ion-beam techniques along with the accuracy that can be achieved in the absence of external calibration are discussed. An analysis of current ICF capsules and some flat-foil targets is presented. This is not the only work that has used ion-beam techniques to characterize ICF targets: recently, Sandia National Laboratory reported on using ion tomography to measure the density and density uniformity of foam targets used in Sandia's ICF program.[4]

Rutherford Backscattering Spectroscopy

The first of two ion-beam techniques used to determine the elemental composition of ICF targets is Rutherford backscattering spectroscopy (RBS). This technique analyzes the energy of ions elastically recoiled off a surface. The stoichiometry, areal density, and presence of impurities in the top 5 to 20 μm of the material can be absolutely determined. Elements with atomic number $Z \geq 4$ can be identified at concentrations as low as 100 parts per million (the sensitivity depends on the atomic mass of the elements involved). The typical surface area of the analysis beam is 1×1 mm, although smaller probe dimensions (limit: 1-μm diam) are achievable by using quadropole electro-optics to focus the beam. The principal disadvantage of the RBS technique is that it cannot be used to detect elements at trace concentrations: it has moderate sensitivity to heavy elements in mid- to light matrices (threshold is 1 in $\sim 10^4$) and poor sensitivity to light elements in heavy matrices (threshold

~1 part in 10). Fortunately, these limitations do not apply to the ICF targets investigated for this article. A second limitation of the RBS technique is the logistical one of having ready access to the equipment. The equipment is expensive to purchase and operate and exists only in a few universities and commercial organizations.

RBS also quantifies the composition of the film at varying depths: the minimum resolvable depth increment is 5 to 10 nm, and the maximum depth the technique can probe depends on the material composition of the film and the ion beam. For example, a He$^+$ beam at 2.0 MeV can distinguish chlorine in a hydrocarbon matrix to a depth of ~ 6 μm; a H$^+$ beam at 1.4 MeV can distinguish chlorine in the same polymer down to 20 μm. These capabilities allow the location and concentration of dopants in a multilayered polymer capsule to be accurately characterized. (A concern in the fabrication process is that the dopant may diffuse out of its original layer when the capsules are processed after the vapor-phase, plasma-polymerization process is complete.)

Principles

Analysis ions are accelerated to a well-defined energy (typically 1 to 10 MeV) and are focused onto the target. Most ions lose energy through inelastic collisions with the target substrate and are implanted into, or are transmitted through, the substrate. A very small fraction of the incident ions elastically recoil off atoms in the target substrate, and a further fraction of the recoiled ions have sufficient energy to escape from the solid and be detected. The energy of the recoiled ions is measured using a surface-barrier detector, and the number of ions in a predefined energy range (referred to as a channel) is counted. The substrate atoms are identified by measuring the energy of the recoiled atom, allowing for the energy the ion loses traversing (both entering and exiting) the substrate. The number of atoms per cross-sectional area is determined from the total number of recoils detected.

A schematic representation of the recoil process is shown in Fig. 75.14(a), and the resulting backscattered spectrum, in Fig. 75.14(b). The abscissa displays the energy of the recoiled ions, where the bandwidth of each energy channel is the energy resolution of the detector (16 keV) and the highest channel number has the greatest energy. The abundance and distribution of elements *A* and *B* are calculated from the peaks A_A and A_B. The peak height depends on (1) the absolute number of identical substrate atoms at each resolvable discrete depth and (2) the kinematics of the ion–atom interaction. The peak width

depends on the distribution of the identical substrate atoms through the film depth: ions that recoil from deeper within the solid possess lower recoil energies as they lose energy traversing the substrate. The ratio of the energy E_0 of the incident ion to the energy E_1^A of the high-energy side of peak *A* is the kinematic factor $K_A = E_1^A / E_0$, which is specific for the incident ion, the target atom, and the scattering angle. The kinematic factor is also given by

$$K = \left\{ \left[\left(M_2^2 - M_1^2 \sin^2 \theta \right)^{1/2} + M_1 \cos \theta \right] \Big/ \left(M_1 + M_2 \right) \right\}^2 ,$$

where θ is the laboratory angle through which the incident ion is scattered and M_1 and M_2 are the masses of the incident ion and target atom, respectively.[5] K, M_1, E_0, and θ are all known, allowing M_2 to be determined. (It is physically intuitive that the greater the mass of the substrate atom, the higher the energy of the recoiled He ion.) The physical basis for this equation is that the kinematic factor depends on the conservation of energy and momentum in a two-body collision, a realistic approximation at these energies (0.5 to 5 MeV for He$^+$) where the collisions are pure Coulombic and where relativistic and off-resonance nuclear reactions do not occur. Tables of the kinematic factors are available for many incident ions (including ^{1}H$^+$ and ^{4}He$^+$) and substrate atoms at discrete recoil angles (θ).[5] An added significance of the kinematic factor is that it influences the mass resolution of the technique; the incident ion and ion energy can be varied to resolve elements with similar masses. Other important factors affecting the accuracy and sensitivity of the technique are the resolution of the surface-barrier detector and energy straggling by the ion beam as it penetrates into the surface (i.e., statistical fluctuations that cause the initially monoenergetic ion beam to assume an increasingly wide energy range as the penetration depth increases).

The areal density of the *i*th element is determined from the knowledge of the experimental configuration [Fig. 75.14(a)]: the detector solid angle Ω; the integrated peak count A_i, for a known number of incident ions Q; and the measured, or calculated, cross section $\sigma_i(E, \theta)$:

$$N_i \, t = \frac{A_i \cos \theta}{Q \Omega \sigma_i (E, \theta)},$$

where N_i is the atomic density of the *i*th element and *t* is the film thickness. If the scattering is Rutherford, the cross section $\sigma(E, \theta)$ can be calculated:

$$\sigma(E,\theta) = \left(Z_1 Z_2 e^2 / 4E\right)^2$$

$$\times \frac{4\left[\left(M_2^2 - M_1^2 \sin^2 \theta\right)^{1/2} + M_2 \cos\theta\right]^2}{M_2 \sin^4 \theta \left(M_2^2 - M_1^2 \sin^2 \theta\right)^{1/2}},$$

where Z_1 and Z_2 are the atomic numbers of the incident ion and target atom, respectively, and $e^2 = 1.44 \times 10^{-13}$ MeV-cm.

This analysis typically yields ±3% uncertainty for the areal density measurement and less than 1% uncertainty for the average stoichiometry. This precision decreases as deeper layers are analyzed because of energy straggling.

Material analyses using these techniques are typically done with ^{4}He ions and modest accelerator energies (0.5 to 2 MeV). At higher and lower energies, the elastic-scattering cross section departs from the Rutherford cross section (i.e., near Coulombic): at lower energies the deviation is due to the nuclear charges being partially screened by the electron shells of both nuclei; at higher energies the deviation is caused by the presence of short-range nuclear forces. Helium is typically used because the backscattering cross sections with all atoms larger than beryllium are nearly Rutherford in this energy region, and there is extensive experimental data regarding the kinematic factors and Rutherford-scattering cross sections.

Nuclear Resonance Analysis of Hydrogen

Accurately quantifying the amount of hydrogen in materials is extremely difficult. Most analytical techniques are unable to detect hydrogen. Those that can detect hydrogen quantify the atom indirectly by probing those atoms/complexes that incorporate hydrogen, i.e., classical spectroscopy looks at the absorption/emission of hydrogen-bonded complexes; electron-detection–based techniques (i.e., x-ray photoelectron spectroscopy and electron-energy-loss spectroscopy) quantify hydrogen from the electron-energy-loss spectrum. More conventional methods (i.e., combustion analysis) that can quantify the hydrogen content typically require a large sample size. This introduces an additional source of uncertainty when analyzing ICF targets since many (typically in excess of 100) capsules are required to obtain the necessary mass. The measured hydrogen content is thus an aggregate value that averages several processing batches and many capsules from the same batch. Consequently, it is impossible to know how much the hydrogen content varies from one target to the next.

Ion-beam–based techniques have been used for more than 10 years to measure hydrogen concentrations in thin films. Because these techniques are sensitive to small variations in hydrogen concentrations and require only a small sample size, they are convenient for analyzing ICF targets. Two ion-beam techniques exist: One technique, elastic recoil detection (ERD), is the reverse of classical RBS since heavy incident atoms forward-scatter lower-Z substrate atoms ($1 \le Z \le 9$) and are themselves kinematically recoiled.[5] The second technique is
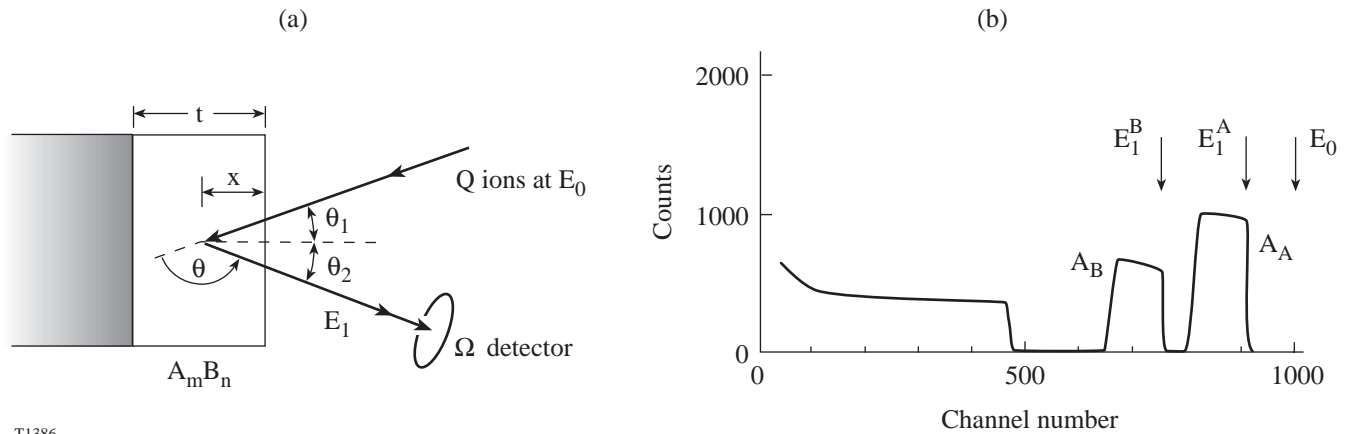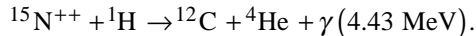
(a)

(b)

T1386

Figure 75.14

(a) Schematic of the experimental geometry used for RBS. (b) Associated Rutherford backscattered spectrum for a two-element material ($A_m B_n$) on a lower-mass substrate.

nuclear resonance analysis (NRA). This technique measures the gamma-ray product (γ) of a nuclear reaction[5]

$$^{15}\text{N}^{++} + {}^{1}\text{H} \rightarrow {}^{12}\text{C} + {}^{4}\text{He} + \gamma \,(4.43 \text{ MeV}).$$

The reaction cross section at the resonance energy (6.385 ±0.005 MeV) is large and decreases rapidly off resonance; the cross section is four orders of magnitude lower and 8 keV off resonance. The γ-ray yield is proportional to the hydrogen concentration at the resonant energy and is accurate to within 2 at.%. Depth profiling is achieved by varying the incident $^{15}\text{N}^{++}$ energy, and as the ion loses energy traversing the solid, a region develops within the solid where the ion energy is at resonance (6.385 MeV) and γ rays are produced. The detection "window" equates to a depth of ~7.5 nm in the solids analyzed for this article. This technique's advantage over ERD is greater depth resolution and sensitivity, and it is this latter technique that is used to analyze ICF targets.

Experimental Conditions

The ion-beam work was analyzed using the Dynamitron Accelerator (Model P.E.A.-3.0) at the Accelerator Laboratory at the State University of New York at Albany. The three ions used were $^{1}\text{H}^{+}$, $^{4}\text{He}^{+}$, and $^{15}\text{N}^{++}$ at energies of 1.4, 2, and 8 MeV, respectively. Three beamlines were used. One beamline was configured for standard RBS analysis (nominal 1-mm × 1-mm spot size). The laboratory geometry [Fig. 75.14(a)] was as follows: the angle between the beam and the detector, ($\theta_1 + \theta_2$), was 14°; the angle between the sample normal and the detector, θ_2, was 7°; the sample normal was 7° above the equator; and the solid angle Ω of the surface-barrier detector was 31 msr. The second beamline was configured for microprobe analysis (spatial spot size ~1-μm diam); the detector was above the incoming beam at $\theta_1 + \theta_2 = 23°$; the sample was perpendicular to the beam; and the solid angle was 87 msr. The third beamline used $^{15}\text{N}^{++}$ for hydrogen analysis. A NaI scintillation detector was positioned directly behind the incident ion beam.

Data recorded during the 5 to 10 min typically required to acquire a RBS spectrum are (1) the number of recoils at each discrete energy resolvable by the surface-barrier detector (FWHM resolution is 16 keV); (2) the total current and charge striking the target; and (3) a correction for the dead time of the pulse-height analyzer. The total charge and current incident on the surface were optimized to obtain a satisfactory signal-to-noise ratio while minimizing any ion-beam damage to the substrate. This latter effect is of special concern as most of the

analyzed materials are plastics and are susceptible to bulk heating effects. Typically the total charge delivered to the substrate is less than 10 μC/cm^2. This threshold was chosen based on a related report that found that bombarding a teflon film with 6-MeV nitrogen ions decreased the fluorine concentration by only 1%.[6] Since carbon–hydrogen and carbon–fluorine bonds have comparable strengths, this ion-beam threshold is believed to have a minimal perturbation on the target's composition. This was confirmed by measuring the hydrogen content of solution-cast polystyrene films to be 50 at.%, the theoretically expected value. The total dead time of the detector is kept below 10% by controlling the ion-beam current. Finally, particle-induced x-ray emission (PIXE) data were acquired and used to help qualitatively identify the elements present in the material.

Data Analysis

The first step to determine whether ion-beam techniques are suitable for analyzing ICF targets is to calculate the behavior of an energetic ion in an ICF target. Of interest are the trajectory and penetration range of different ions, at specific energies, within the material. These data are available using "Stopping and Range of Ions in Materials"[7]—a software that uses the known collisional cross sections and stopping powers to perform a Monte Carlo simulation of an ion's path through the material. In this manner the divergence ("straggling") of the beam as a function of depth can be determined. Also, the energy lost by the ion to the substrate as it penetrates deeper into the material can be determined.

An example of this simulation is shown in Fig. 75.15. The modeled substrate is a multilayered polymer capsule, as provided by General Atomics, and analyzed by RBS (Fig. 75.16). The incident He ion is at 2 MeV and is defined as a point source on the surface of the substrate. The ion penetrates 9.44 μm into the plastic with a depth "straggle" of 0.18 μm and a radial divergence of ~0.3 μm [Figs. 75.15(a) and 75.15(b)]. Figure 75.15(c) shows the energy lost as a function of depth as the He ion penetrates the material; on average, the ion loses ~20 eV/Å. This information is useful for determining whether the ion beam is heating and possibly altering the substrate. These data confirm that a microprobe beam with a 2-μm-diam spot size will sample a cylindrical volume no greater than 3 μm in diameter and ~8 μm deep.

The Rutherford backscattering spectrum is analyzed using a standard code—Rump[8]—which uses known kinematic factors, Rutherford cross sections, and stopping powers to simulate a backscattered energy spectrum for any material

composition. The procedure is to first simulate the RBS spectrum using a "guessed" elemental composition and then compare the theoretical spectrum with the actual spectrum. The guessed composition is then refined and the theoretical spectrum recalculated. The process is iterated until the stimulated recoil spectrum corresponds with the actual spectrum. When the material is not isotropic, it is necessary to specify the composition of the material at discrete layers. Agreement between the theoretical and actual spectra of various ICF polymer targets is shown in Figs. 75.16–75.18. The accuracy of these analyses is ±2 at.% of the absolute value for the primary

components (i.e., C, N, O) and 5% to 20% for trace (<10 at.% total concentration) dopants such as Cl, Si, Ge, and Ti.

RBS detects elements with atomic numbers greater than 4. As this excludes hydrogen, a major component of ICF polymer capsules (~50 at.%), its concentration was determined using nuclear resonance analysis. The hydrogen concentration (ρ_H) is related to the experimentally measured gamma-ray yield (Y) by

$$Y = \int Q \rho_H(x) \sigma(x) \, dx,$$

(a)

(b)

(c)
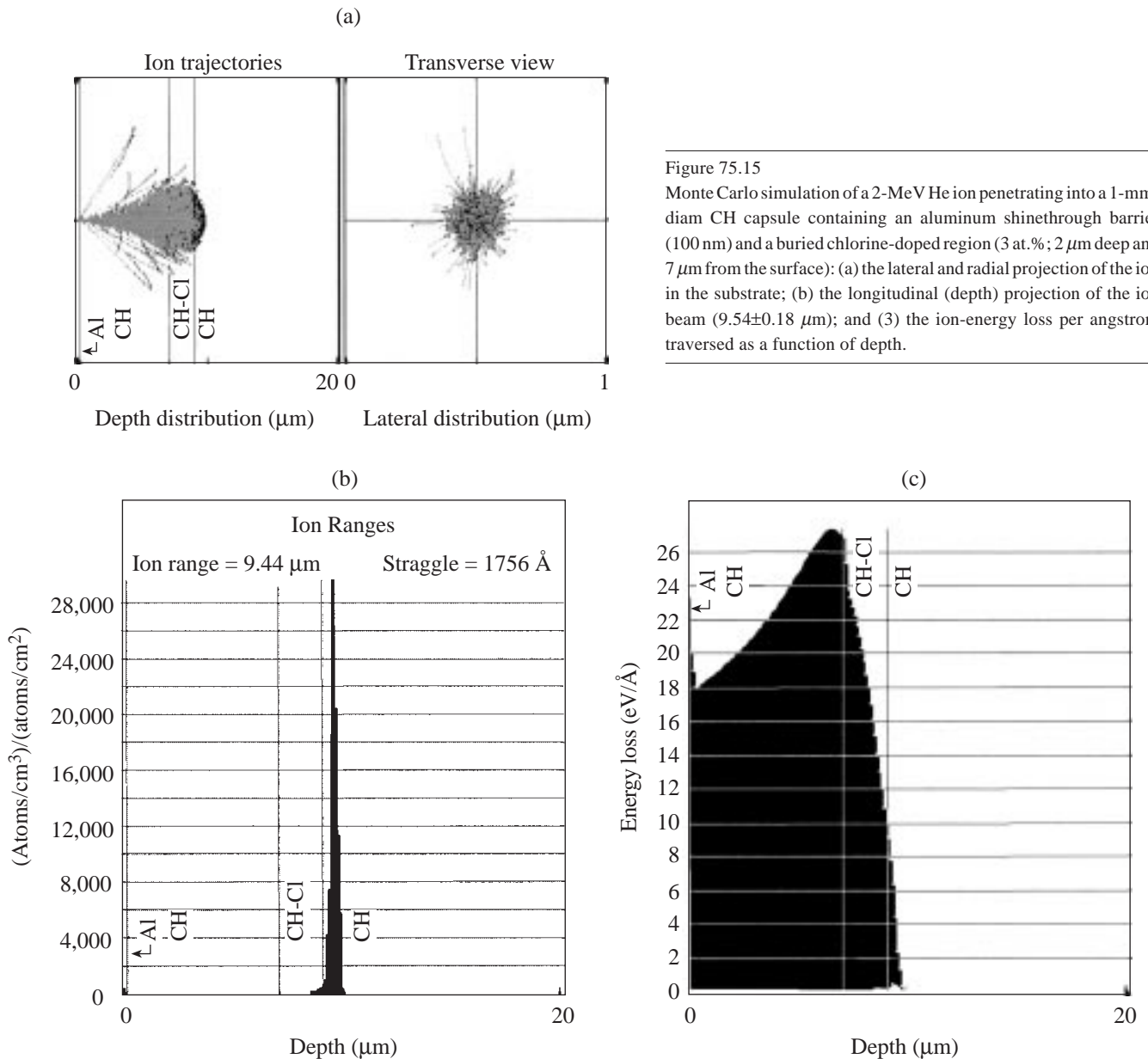
Figure 75.15
Monte Carlo simulation of a 2-MeV He ion penetrating into a 1-mm-diam CH capsule containing an aluminum shinethrough barrier (100 nm) and a buried chlorine-doped region (3 at.%; 2 μm deep and 7 μm from the surface): (a) the lateral and radial projection of the ion in the substrate; (b) the longitudinal (depth) projection of the ion beam (9.54±0.18 μm); and (3) the ion-energy loss per angstrom traversed as a function of depth.

T1420

where Q is the number of incident ions and σ is the cross section. Clearly, this cross-sectional dependency requires the film's elemental composition (elements other than hydrogen), film thickness, and density to be accurately known—information that is obtained from the RBS analysis.

Using $dx = dE/(dE/dx)$ gives

$$Y = Q\int \frac{\rho_H(E)\,\sigma(E)}{dE/dx}\,dE,$$

where

$$\sigma(E) = \frac{\sigma_0 \Gamma^2/4}{(E - E_{res})^2 + \Gamma^2/4}$$

is the Breit–Wigner formula,[5] σ_0 is the cross section at the resonance energy, and Γ is the full width at half-maximum of the cross section. Integration yields

$$Y = \frac{Q\rho_H \pi/2\sigma_0\,\Gamma}{dE/dx}$$

or

$$\rho_H(x) = K(dE/dx)\,Y(x),$$

where K is a constant incorporating all the cross-section parameters (including detector efficiency). K is independent of the material being analyzed; for example, to calculate the amount of hydrogen in a hydrocarbon:

$$\rho_H(\text{at.\%}) = (0.45 \times 10^{19})(dE/dx)_{CH}$$
$$(\text{measured \# counts}/\,0.5{-}\mu C\ \text{total charge}),$$

and

$$(dE/dx)_{CH} = \rho_{CH}\frac{\chi_C(dE/dx)_C + \chi_H(dE/dx)_H}{\chi_C MW_C + \chi_H MW_H},$$

where 0.45×10^{19} is the constant K, dE/dx is the stopping power of the CH substrate, MW is the molecular weight, and χ is the atomic fraction. The penetration depth is equal to

$$\left[E(^{15}N) - E_{reson}(6.385\ \text{MeV})\right]/(dE/dx)_{CH}.$$

Clearly, to completely analyze a polymer capsule, both RBS and NRA data sets must be obtained and iterated until each data set can be accurately simulated with the same elemental composition.

Results

1. Plasma Polymer Capsules

The elemental composition of all types of ICF capsules used at LLE are summarized in Table 75.III. For the most common type of ICF target, a hydrocarbon capsule made by plasma
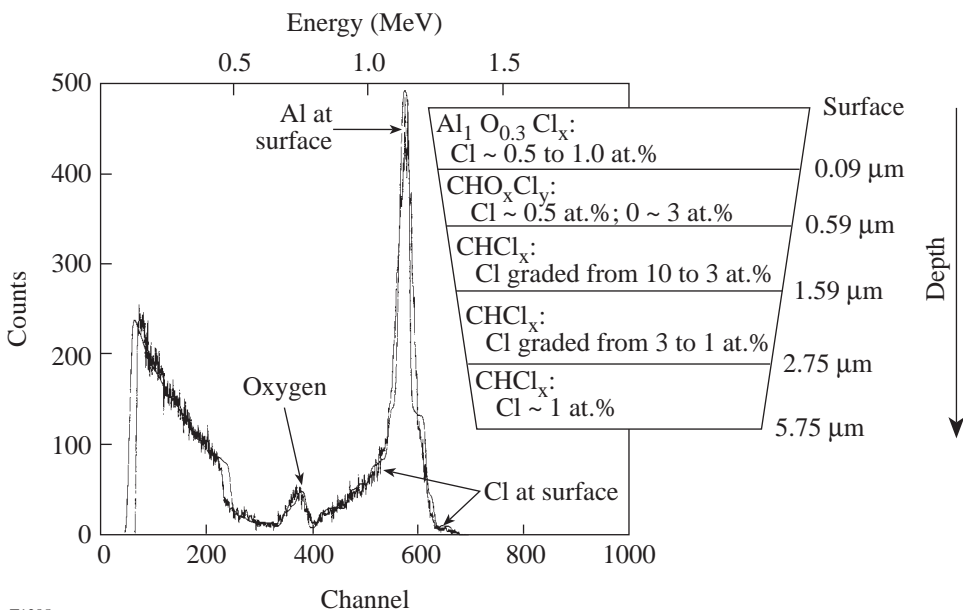

Figure 75.16
RBS spectrum of a 900-μm-diam capsule overlaid with the simulated spectrum. The Cl distribution of elements in the top 5.75 μm is inset.

T1285

Table 75.III: The range of composition of each element in capsules and flat films provided by GA, as measured using ion-beam analysis.

Film Material	Composition (fractional-atom content)						
	Carbon	Hydrogen	Silicon	Germanium	Titanium	Chlorine	Oxygen
CH	0.4→0.48	0.5→0.55					0.02→0.06
CH-Cl	0.44→0.47	0.50→0.53				<0.01→0.1 (pyrolyzed) 0.02→0.03 (unpyrolyzed)	0.01→0.04
CH-Ti	0.33→0.43	0.42→0.62			0.015→0.067	0→0.015	0.02→0.08
CH-Si	0.40	0.47	0.06				0.07
CH-Ge	0.42→0.44	0.48→0.50		0.02→0.04			0.02→0.08

polymerization, the hydrogen concentration ranged from 50 to 55 at.%. There is insufficient data to determine statistically if this variation is inherent in the plasma-processing method or if the fluctuation is a measure of the repeatability of the process. Oxygen was also identified in the polymer; the quantity varied from <1 at.% to a maximum of ~6 at.%. It is speculated that oxygen is adsorbed from the environment and that the concentration depends on how long the capsule was exposed to air. (The maximum of 6 at.% was observed after the plastic had been stored in the laboratory for several months.)

Data obtained from analyzing capsules doped with high-atomic-number elements are summarized below.

a. Silicon-doped capsules. The concentration was constant at 6±1 at.% in all the shells and flat films analyzed. Moreover, silicon was uniformly distributed throughout the depth of the shell wall, as far as the ion beam could probe (6 μm). Figure 75.17 (spectrum 3) shows that the leading edge of the silicon signal was suppressed when a hydrocarbon plastic overcoat was applied (as was expected). Importantly, this signal remained suppressed when the capsule was pyrolyzed (a necessary processing step to remove the mandrel). The absence of any signal due to silicon having diffused to the outer surface of the capsule demonstrated the thermal stability of the silicon-doped plastic; hence, this material is suitable for processing by the current target-fabrication techniques. The oxygen content was 7 at.%.

b. Germanium-doped capsules. The germanium-doping fabrication process was evaluated by examining Ge-doped capsules made simultaneously in the same batch and also in

different batches. As with the silicon-doped capsules, the germanium concentration was uniformly distributed throughout the wall of the capsule (shown in Fig. 75.18), and oxygen was present. The measured germanium concentrations varied from 2 to 4 at.% from one capsule to the next. The variation is a measure of the repeatability of the processing conditions: plasma polymer capsules fabricated at the same time varied by less than <1 at.% while those made in different batches varied by a factor of 2. Although the processing conditions were intentionally identical for all the batches analyzed, the varying germanium concentrations demonstrate the inherent control and repeatability of the process.

c. Titanium-doped capsules. The ion-beam analysis technique was used by LLE to assist GA in developing Ti-doped plasma polymer capsules. Capsules were produced using purposely varied processing parameters, and the resulting titanium concentrations varied from 1 to 8 at.%. High titanium concentrations (6 at.%) were accompanied by high oxygen levels (9 at.%) and lower hydrogen concentrations (41 at.%). Figure 75.19 shows this correlation; the depth-profiled hydrogen concentrations at 0.1, 0.28, and 0.44 μm are shown for two films containing different titanium concentrations. Currently, capsules with titanium concentrations of from 3 to 6 at.% are available.

d. Chlorine-doped capsules. The chlorine content was analyzed using both helium and hydrogen ion beams; the former provided greater sensitivity and accuracy while the latter provided greater penetration that allowed the complete 20-μm wall of the capsules to be profiled. The quantity and position of the chlorine were found to be strongly dependent on
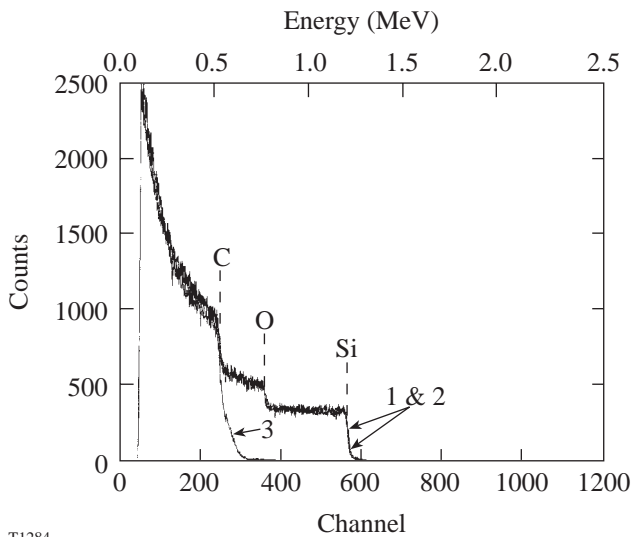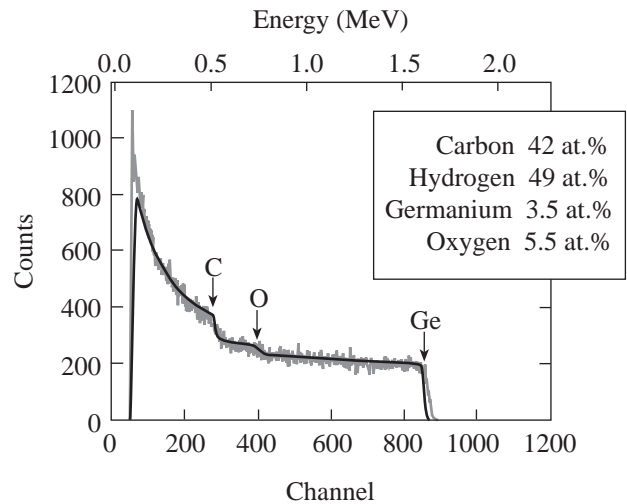
T1284

Figure 75.17
RBS spectra of three silicon-doped capsules show that the silicon is uniformly distributed through the capsule wall and is thermally stable: (1) Si-doped CH; (2) Si-doped CH after pyrolysis; and (3) Si-doped CH overcoated with CH and then pyrolyzed at 300°C.

T1387

Figure 75.18
RBS spectrum of a Ge-doped capsule. Germanium is uniformly distributed through the first 5 μm of the capsule wall.
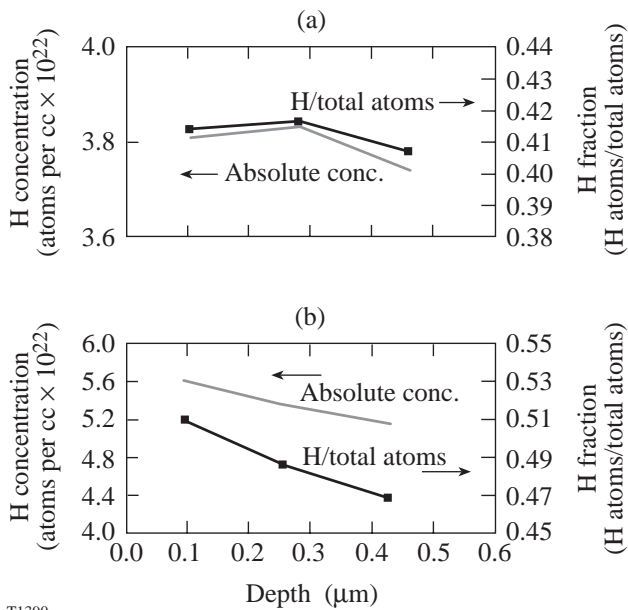

T1390

Figure 75.19
Depth-profiled hydrogen concentrations (expressed as an absolute density and an atomic fraction) in two Ti-doped plastic films: film (a) consists of 44-at.% carbon, 6-at.% titanium, and 9-at.% oxygen content, and film (b) consists of 42-at.% carbon, 2-at.% titanium, and 6-at.% oxygen.

how the polymer capsule was processed. When the capsule was pyrolyzed at 300°C after fabrication (as is typically done to remove the decomposable mandrel), chlorine diffused from the originally doped layer and was distributed throughout the shell wall. The chlorine concentration at any depth would vary from <1 to 10 at.%, with the higher concentration measured in a very thin band at the external wall of the shell. The distribution is shown in Fig. 75.16. Here, chlorine was intended to be located in a 2-μm region 7 μm beneath the surface. In reality, chlorine was detected throughout the top 5.75 μm of the capsule—the maximum depth at which the He ion at 2 MeV could detect chlorine in plastic. A hydrogen ion beam was used to extend the depth sensitivity to detect how far chlorine had diffused into the capsule's wall (a different capsule from the one analyzed above). The resulting spectrum is shown in Fig. 75.20. The chlorine-doped layer was intended to be 1 μm thick and 6 μm below the surface with a concentration of 6 at.%. Actually, the layer was distributed through the top 10 μm of the capsule with an average concentration of 0.05 at.%; no chlorine was detected at greater depths.

Analysis of many chlorine-doped capsules shows the chlorine concentration to be 2 to 3 at.% and thermally stable when the chlorine-doped layer is deposited after the pyrolysis is complete. The consequence of these results for designing targets for ICF experiments is that capsules with a chlorine-doped layer within 3 μm of the inner surface are not achievable; conversely, capsules with a chlorine-doped layer more than 3 μm from the inner surface are feasible.

Energy (MeV)
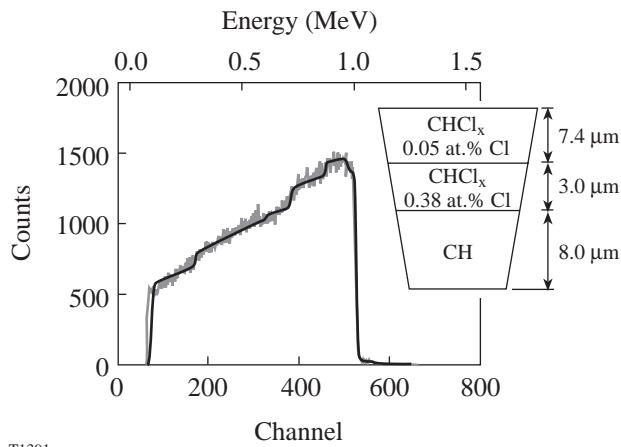
T1391

Figure 75.20
The experimental RBS spectrum of a Cl-doped CH capsule overlaid with the simulated fit. A 1.4-MeV H-ion beam profiled the entire 18.4-μm thickness of the capsule wall.

e. *Deuterated capsules.* The fully deuterated polymer capsule is an important type of ICF target. It is made by polymerizing deuterated-gas monomers onto a poly-α-methylstyrene mandrel and then pyrolyzing the composite to remove the mandrel. It is important that no hydrogen be present in the capsule wall after the process. [It is possible that the deuterium in the CD wall and the hydrogen in the poly-α-methylstyrene (PAMS) wall could exchange during the pyrolysis process.] Hydrogen was not detected in the CD capsule wall, which, given the threshold sensitivity of the NRA technique, limits the hydrogen content in the deuterated plastic to be below 1 at.%.

2. Flat-Foil Targets

A type of target used in plasma physics experiments consists of several layers of different elements used to spectroscopically diagnose the plasma temperature. The more accurately the number of atoms in each layer is known (from the measured film thickness, composition, and areal density), the more accurate is the temperature measurement.[9] Current sputter-deposition and evaporation techniques measure the deposition rate using quartz crystal monitors, a method that can measure the film thickness to within 3%–8% but cannot measure the elemental composition. An independent nondestructive method for analyzing targets after they are assembled is needed, and RBS is a suitable technique.

A target analyzed here consisted of a 1-mm-diam plastic (CH) film overcoated with two thin layers of Ti and KCl. The thickness was measured with 3% accuracy. The titanium layer consisted of 30-at.% oxygen (not surprising since titanium is an effective oxygen getter), and the stoichiometric ratio of K to Cl was 1 to 1. These data allowed the total number of titanium, potassium, and chlorine atoms to be determined.

A type of target used for hydrodynamic instability studies uses an open-cell foam (2- to 5-μm pore size; 1-mm diam and 100 μm thick) overcoat to help minimize the growth of the Rayleigh–Taylor instability. Whereas the target design called for a thin, gold overlayer on the foam, fabrication complexities made it impossible to ensure that the gold was confined to the foam's outer surface (given the open cell structure of the material). The RBS spectrum determined that the sputtered gold atoms had penetrated 30 μm below the surface (Fig. 75.21). These data demonstrated that the target, as-
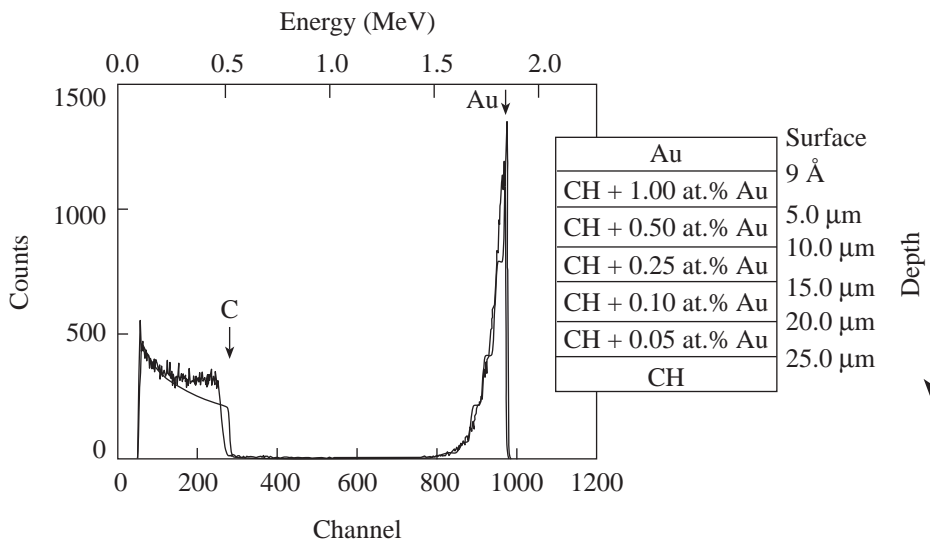
T1421

Figure 75.21
The experimental and simulated RBS spectra of a 30-mg/cm^3-polystyrene foam overcoated with 1 nm of gold.

fabricated, differed significantly from what was intended. This information helps define the capabilities and limitations of different target-fabrication methodologies, which is essential for building new types of targets.

3. Polyimide Shells

The ion-beam analysis technique has also been used to assist the polyimide-shell-development effort.[10] Compositions of films deposited by different processing conditions were determined using both RBS and NRA. Examples of the depth-profile data are shown in Fig. 75.22. These data show that both the elemental ratio in the polyamic acid precursor and the resultant polyimide material were very close to the expected

stoichiometric values; however, both materials possessed excess nitrogen (~2 at.%). This information has allowed the processing parameters to be refined with the goal of optimizing the mass flux of the two precursor monomers.[11]

As discussed previously, RBS provides areal density information, and additional information about the actual (theoretical or measured) density is required to extract the film-layer-thickness information. Conversely, if the film thickness is known, then the actual density can be determined. This approach was used to determine the density of the precursor (polyamic acid) and final (polyimide) films. Films of measured thickness were analyzed, and the density of the
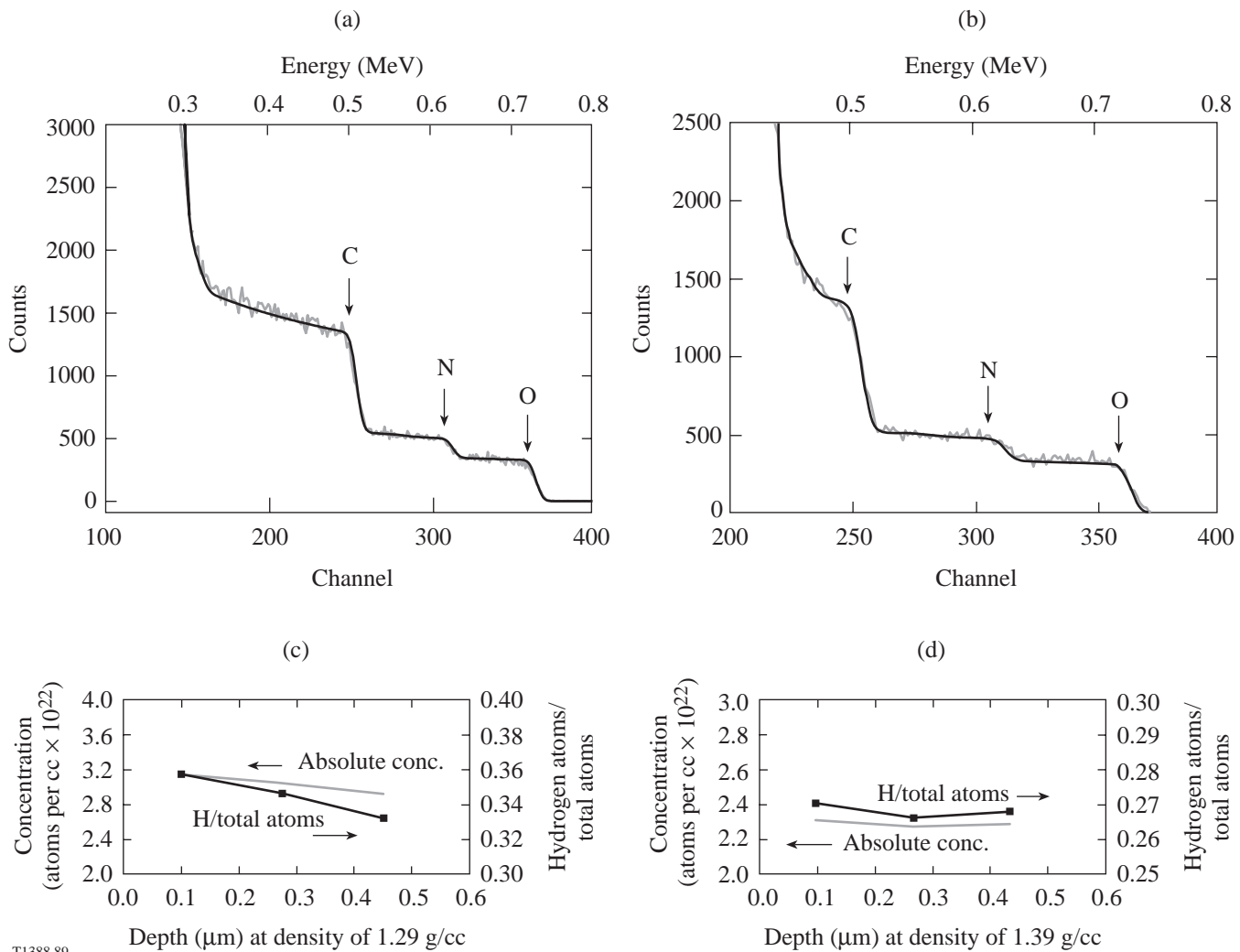
Figure 75.22
The experimental RBS spectra (with the simulated spectra overlaid) and NRA spectra of polyamic acid [(a) and (c)] and polyimide [(b) and (d)] films. The polyamic acid is 2.18 μm thick, consists of 47-at.% carbon, 35-at.% hydrogen, 7-at.% nitrogen, 11-at.% oxygen, and has a density of 1.28 g/cm^3. The polyimide film is 1.78 μm thick, consists of 55-at.% carbon, 26-at.% hydrogen, 7-at.% nitrogen, 12-at.% oxygen, and has a density of 1.44 g/cm^3.

polyamic acid and polyimide films was determined to be 1.29 ± 0.02 g/cm^2 and 1.44 ± 0.02 g/cm^2, respectively. The value of knowing these data is twofold: (1) the implosion dynamics can be more accurately modeled, and (2) significant changes in density and porosity can induce significant changes in the residual intrinsic stress that affects the survivability and ultimate strength of the material.

Summary

Two ion-beam techniques, Rutherford backscattering spectroscopy and nuclear resonance analysis of hydrogen, used in conjunction, provide an accurate method for analyzing the complete elemental composition of individual capsules. These data are used to interpret ICF data and to support the development of suitable targets. The strengths of these techniques are (1) they are absolute measurements that do not rely on external calibration to infer the composition of the substrate material, and (2) they provide depth-resolved information, essential data to confirm that the fabricated targets are what they were designed to be.

ACKNOWLEDGMENT

REFERENCES

1. S. A. Letts, D. W. Myers, and L. A. Witt, J. Vac. Sci. Technol. **19**, 739 (1981).

2. N. Abbas, ICF Target Component Fabrication and Technology Development Support, FY96 Year-End Review, San Diego, CA (October 1996).

3. Internal Confinement Fusion Target Component Fabrication and Technology Development Support, General Atomic's Annual Report to the U.S. Department of Energy, 1 October 1996–30 September 1997.

4. A. Antolak, ICF Target Component Fabrication and Technology Development Support, FY97 Year-End Review, San Diego, CA (October 1997).

5. J. R. Tesmer and M. A. Nastasi, eds. *Handbook of Modern Ion Beam Materials Analysis* (Materials Research Society, Pittsburgh, PA, 1995).

6. P. Bodo and M. Schott, Thin Solid Films **286**, 98 (1996).

7. J. F. Ziegler, J. P. Biersack, and U. Littmark, *The Stopping and Range of Ions in Solids*, The Stopping and Ranges of Ions of Matter, Vol. 1 (Pergamon Press, New York, 1985).

8. L. R. Doolittle, Nucl. Instrum. Methods Phys. Res. B **B9**, 334 (1985).

9. D. D. Meyerhofer, presented at the 25th European Conference on Laser Interactions with Matter (25th ECLIM), Formia, Italy, 4–8 May 1998.

10. E. L. Alfonso, S.-H. Chen, R. Q. Gram, and D. R. Harding, "Properties of Polyimide Shells Made Using Vapor Phase Deposition," to be published in the Journal of Materials Research.

11. E. L. Alfonso, S.-H. Chen, R. Q. Gram, D. R. Harding, and F. Y. Tsai, "Fabrication of Polyimide Shells by Vapor Phase Deposition for Use as ICF Targets," presented at the Target Fabrication Meeting, Jackson Hole, WY, 19–23 April 1998, and to be published in Fusion Technology.

Kα Cold-Target Imaging and Preheat Measurement Using a Pinhole-Array X-Ray Spectrometer

Two-dimensional (2-D) monochromatic imaging of laser-imploded targets[1–6] is useful for diagnosing target compression and stability. Here we present a simple method for such imaging, using an array of about 300 pinholes placed in front of a flat-crystal x-ray spectrometer. The main advantage of this method (in addition to its simplicity) is the ability to simultaneously obtain a large number of images over a wide range of photon energies. This is particularly useful for imaging the emission region of a single spectral line from a doped target, where images around the wavelength of the line can be simultaneously obtained and subtracted from the image at the line. Imaging a spectral line of a dopant can be useful for studying mixing of target layers. *Here we use the array to image Kα fluorescence from a titanium-doped target (excited by core radiation) and thereby obtain an image of the cold layer at peak compression.* This image can otherwise be obtained only through backlighting. Using a flat crystal limits the field of view, but this limitation is shown not to be severe when imaging the compressed target core. On the other hand, the narrow field of view translates into improved spectral resolution. We show that sufficient intensity can be obtained in monochromatic imaging even without the gain in intensity when using a focusing crystal. In addition, the array provides spectra of high spectral resolution because of the reduction in the effective source size. Finally, we show that, in addition to the core-pumped Kα emission, a second Kα-emitting zone of a larger radius appears in the image. This Kα emission is pumped during the laser-irradiation pulse, indicating preheat by suprathermal electrons.

Figure 75.23 shows the geometry of the pinhole array placed in front of a crystal spectrometer. The dispersion direction indicated in Fig. 75.23 is determined by the orientation of the array with respect to the crystal. Rays from the target traversing different pinholes fall on the crystal at different angles; thus, different wavelengths are diffracted. The distance between adjacent pinholes (750 μm) is chosen so that adjacent images on the film are close but not overlapping. Rays from different parts of the target traversing the same pinhole also fall on the crystal at different angles; thus, the target image from

continuum radiation is not monochromatic; rather, the photon energy across the image (in the dispersion direction) varies over a finite interval. A single spectral line will show the image of only a narrow section of the target (in the dispersion direction); however, the compressed core can be imaged by a spectral line of sufficient spectral width. In the direction of dispersion, the shift in the average photon energy between adjacent images is typically ~100 eV. The line of pinholes in a direction perpendicular to that of the crystal dispersion is slightly tilted, causing a small photon-energy shift (of the order of ~10 eV) between two adjacent images in that direction; thus, an array of 30 × 10 pinholes can produce 300 images with energies spread over the range of, say, 4 to 7 keV. The advantage due to the tilt in the vertical lines of pinholes can be viewed in two ways: (a) for a given target location, adjacent images correspond to slightly shifted photon energy, or (b) for a given spectral line, adjacent images correspond to slightly different sections of the target. The properties of array imaging,
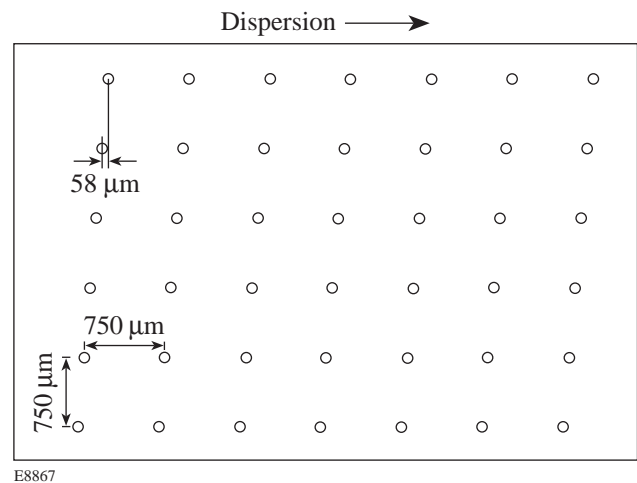

Figure 75.23
The geometry of the pinhole array placed in front of the spectrometer. Each of about 300 pinholes yields a narrow-band, 2-D image at a slightly shifted photon energy. The 58-μm shift due to the tilt in the vertical direction yields an energy shift between adjacent images of ~6 to 10 eV in the range of 4 to 5 keV.

in conjunction with the test results shown in Figs. 75.24 and 75.27, will be further discussed below.

Two arrays of the type shown in Fig. 75.23 were used to image targets imploded on the 60-beam OMEGA laser system.[7] In both cases, the target consisted of a polymer shell containing an embedded, titanium-doped layer. We show two examples of such tests: In the first shot (a) an array of 50-μm-diam pinholes (in 25-μm-thick Pt foil) was used, and the results are shown in Fig. 75.24 (this figure is used mostly to illustrate the properties of array imaging). In the second shot (b) an array of 25-μm-diam pinholes (in 12.5-μm-thick Pt foil) was used and the results are shown later in Fig. 75.27 (this figure is used mostly to illustrate the imaging of the cold, compressed shell through Kα-line fluorescence). Except for the pinhole size and foil thickness, the two arrays had the same geometry as in Fig. 75.23.
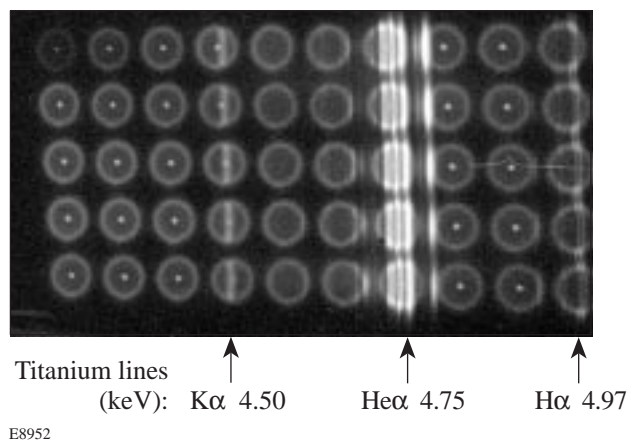

Titanium lines
(keV):   Kα 4.50   Heα 4.75   Hα 4.97

E8952

Figure 75.24
Part of the ~300 array-spectrometer images obtained with an array of 50-μm pinholes, from a titanium-coated target implosion [shot (a)]. Because of the vertical tilt in the array (see Fig. 75.23), the target section imaged by a given spectral line shifts for successive images in that direction. Lines (such as the Heα line) from a different target location can reappear on a neighboring image.

Properties of Array Imaging

In shot (a) a CH polymer shell of 867-μm inner diameter and 13.7-μm thickness was doped with titanium at 7% by atom number, overcoated by 13.9-μm-thick undoped CH. The fill gas was 10 atm deuterium. The laser pulse was a 1-ns flat pulse (to within ±5%) with 0.1-ns rise and fall times and 29.8 kJ of energy. Figure 75.24 shows part of the array images obtained with a Ge(111) diffracting crystal. The dispersion direction is horizontal—a tilt in the images in the vertical direction is

evident. Both the Ti-Kα line and lines of Ti[20+] (helium-like) and Ti[21+] (hydrogen-like) ions are marked. The Ti[20+] Heα line and its dielectronic satellites reappear on neighboring images. This is due to parallel rays emanating from different target locations and traversing adjacent pinholes. Without the array, these two groups of lines would be part of a broad spectral feature representing emission from the whole target. The array transmits rays from only two target slices.

Individual lines yield monochromatic images of only a section of the target (because rays from other target sections do not satisfy the Bragg diffraction condition for that line). On the other hand, the continuum radiation gives rise to complete target images; however, these images are not monochromatic—the photon energy shifts across the image in the direction of dispersion (by ~100 eV). The energy shift between adjacent images in the dispersion direction varies from ~80 eV (at 4 keV) to ~130 eV (at 5 keV). The tilt in the vertical direction causes a photon-energy shift between two adjacent images that varies from ~6 eV (at 4 keV) to ~10 eV (at 5 keV).

The narrow field of view for individual lines (in the direction of dispersion) can be remedied by replacing the flat crystal with a curved crystal in the Rowland-circle geometry;[2,3,5] however, Fig. 75.24 shows that typical lines can be spectrally wide enough for imaging the core even with a flat crystal. This is seen simply in the fact that the lines are about as broad as the target core (e.g., in the lowest image in the column marked "Kα"). The width of the lines in this context refers to their spectral width, transformed into a spatial width in the image. This transformation is obtained by differentiating the Bragg law for diffraction, from which the spatial extent Δx covered by a single spectral line of width ΔE (in the direction of dispersion) can be obtained. The result is $\Delta x = (\Delta E/E)L \tan \theta_B$, in terms of the Bragg angle θ_B and the target distance to the film (along the relevant ray). The spatial width of the Kα line in the direction of dispersion is ~130 μm. Part of it is due to the pinhole size (50 μm), but most of it is due to the spectral width of the Kα line (a larger pinhole size increases the field of view in the direction of dispersion but reduces the spatial resolution in both directions). Deconvolving the pinhole broadening from the total width shows that the spectral width of the line is ~5 eV and that the spatial width would be ~120 μm when using a very small pinhole. Thus, a flat crystal can yield 2-D Kα monochromatic images of only the core; however, there is no limitation on the field of view in the direction perpendicular to that of the dispersion. Furthermore, because the pinholes tilt in the vertical direction, the position of a given spectral line shifts across the target image for successive images in that direction, as is

clearly evident in Fig. 75.24; thus, the combination of successive images in the vertical direction delineates the total emission region of the line. This works particularly well for the $K\alpha$ line since its linewidth (~5 eV) is about the same as the average energy shift between successive images in the vertical direction (~6 eV). In higher-performing implosions the shell temperature would be higher so that some M-shell electrons would be ionized; in that case, the $K\alpha$ line would be broader due to the overlapping of shifted lines from various charge states, and the field of view would then broaden. Also, in such implosions the compressed core is smaller and would thus require a smaller field of view.

The Ti^{20+} and Ti^{21+} lines in Fig. 75.24 are seen to be emitted from the target periphery, i.e., the hot laser-absorption region. On the other hand, the $K\alpha$ line is emitted by the cold part of the Ti-doped layer following the photoionization of K-shell electrons. The source of this radiation can be either the coronal emission during the laser irradiation or the core radiation during peak compression. The $K\alpha$ line emission in Fig. 75.24 is seen to come from a layer inside the hot corona region: the diameter of the coronal rings is ~900 μm, whereas the length of the $K\alpha$ emission region perpendicular to the dispersion direction is only ~750 μm, and it peaks near its extremities. Thus, the radiation from the laser-heated corona pumps the fluorescence of $K\alpha$ in the cold shell underneath the coronal region. An additional peak can be seen at the target center, indicating the possible $K\alpha$ emission pumped by core radiation. This point is discussed in more detail in the next section, where the results of shot (b) clearly indicate $K\alpha$ fluorescence pumped primarily by core radiation.

An important advantage of this device is the ability to reliably subtract the continuum images off a spectral line from the image on the line, thus obtaining the image of the region emitting that line. This is further discussed in conjunction with Fig. 75.27, where the cold shell is imaged through its $K\alpha$ fluorescence. Additionally, the core spectrum can be easily separated from the coronal emission and plotted over a wide spectral range with good spectral resolution. Additional useful information in Fig. 75.24 is the absence of target cores in the spectral range of ~4.5 to 4.7 keV and above ~4.9 keV due to absorption of core radiation in the cold titanium layer. This absorption is due to titanium $1s$–$2p$ absorption lines and absorption above the Ti K edge, respectively.[8]

The array spectrometer can be alternatively used for achieving high spectral resolution: in the case of a large emitting source (such as emission prior to peak compression) the pinholes limit the effective source size and thus improve spectral resolution. For example, the fine-structure splitting of the Hα line of titanium is clearly seen in Fig. 75.24, indicating a resolution higher than 500. Without the pinhole array the whole target would radiate the line and the spectral resolution would be less than 100. In Fig. 75.25 the lineout in the direction of dispersion shows that a high-resolution spectrum can be obtained from a large source for lines that are much stronger than the continuum. In that case, the images formed by the continuum can be subtracted and the net line emission obtained. In general, the lineout can be recorded as a function of target position (perpendicular to the direction of dispersion). To facilitate the continuum-image subtraction, the lineout in Fig. 75.25 was chosen to avoid the core emissions. To further illustrate the high spectral resolution, we compare (in Fig. 75.26) part of the spectrum of Fig. 75.25 with that obtained simultaneously by an identical spectrometer where the pinhole array has been replaced by a 50-μm-wide slit. In the latter spectrum, the lines are considerably broadened due to the source size (~0.8 mm). They are further affected by the spatial distribution of target emission; because of the limb effect, the spectral lines appear on film as partly overlapping rings, giving rise to spurious splits in the spectrum. An 0.8-mm source size corresponds in the present arrangement without the array to a spectral resolution $E/\Delta E$ of ~130, whereas the pinhole-array spectrum in Fig. 75.26 shows a spectral resolution $E/\Delta E$ higher than ~500.

E8864
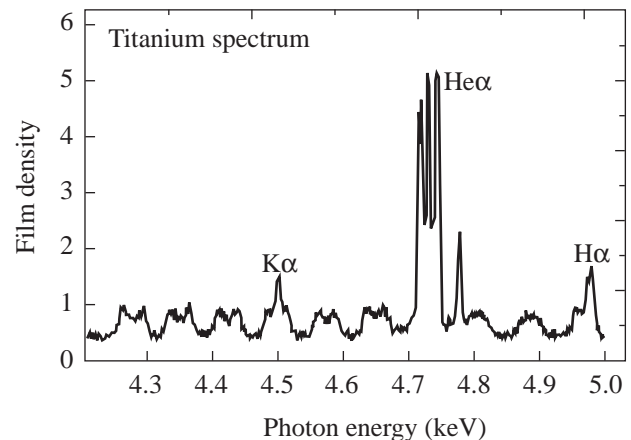
Figure 75.25
Lineout of Fig. 75.24 in the direction of dispersion (avoiding the cores), showing that a high-resolution spectrum from a large source can be obtained by using a pinhole-array spectrometer. For lines that are much stronger than the continuum, the images (that are due to the continuum) can be subtracted away. The line at ~4.8 keV is the Ti Heα line (from a different target location) transmitted though an adjacent pinhole.
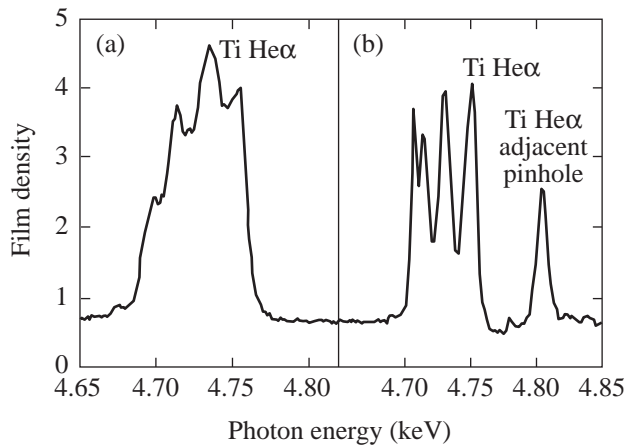
E8825

Figure 75.26
Comparison of the Ti Heα line manifold obtained simultaneously with and without the pinhole array. The Heα line ($2p^1P–1s$ transition in Ti^{20+}) is well resolved from its low-energy satellites when using the array. Without the array the lines are considerably broadened by the ~0.8-mm source size.

Imaging the Cold Shell with Kα Fluorescence

In shot (b), an empty CD polymer shell of 898-μm inner diameter and 5.9-μm thickness was coated with an 11.7-μm-thick layer of CH doped with titanium at 2% by atom number, overcoated by 13.5-μm-thick undoped CH. The laser pulse shape was the same as in shot (a), and its energy was 27.1 kJ.

Figure 75.27 shows part of the array images from target shot (b) obtained with a PET(002) diffracting crystal. The laser-irradiation uniformity in this shot was deficient, leading to a nonuniform implosion. We chose to display a section of the array images where the Kα line image is centered on the target core (second image from left). For images above and below this image the Kα line moves off target center toward the left and right, respectively. The Ti^{20+} lines (indicative of hot plasma) are seen to be emitted from the periphery of the target. On the other hand, a ring of emission at the wavelength of the Ti Kα line (indicative of a cold plasma) is seen to be emitted around the compressed core. This is evident when comparing the emission around the core in the second image from left to that in the other images. The nonsphericity of the Kα emission pattern is discussed below. The spatial features of these lines indicate that the Ti Heα line is emitted during the laser-irradiation time, whereas the Kα line is emitted around peak compression and is pumped by core radiation. These conclusions are consistent with the streaked spectra obtained for shot (b). Figure 75.28 shows lineouts of streaked spectra at three different times of the implosion: t_1– during the laser-irradia-

tion period (lasting about ~1 ns); t_2–during the shell coasting when no radiation is emitted (lasting about 0.8 ns); and t_3–during peak compression, or stagnation (lasting about 0.2 ns). It is clearly seen that the Ti^{20+} Heα line is emitted during the laser irradiation; more precisely, the streak record shows that it is emitted toward the end of the laser pulse, when the burnthrough of the polymer overcoat has reached the doped layer. On the other hand, the Kα line is emitted during peak compression. This is entirely consistent with the conclusions drawn from the spatial patterns of these lines. In addition to the Kα line, the spectrum at peak compression also shows strong absorption above the Ti K edge. This is absorption of core radiation by the cold shell around the core and is precisely the source of photoionization leading to Kα fluorescence;[9] this observation provides an additional indication that the Kα line is pumped by core radiation at peak compression. The drop of intensity above the K edge can be used to estimate the areal density ($\rho\Delta r$) of the doped layer at peak compression and from here the total $\rho\Delta r$ of the compressed shell. It should be pointed out that there is very little change in the K-shell absorption at a given energy when M- or L-shell electrons are ionized.[10] In this case, however, the transmitted intensity above the K edge is too weak to determine the areal density, and only a lower limit of the $\rho\Delta r$ can be obtained. Assuming transmission of less than ~10% at the K edge, the areal density of the doped layer is $\rho\Delta r > 22$ mg/cm^2. The total areal density of the compressed shell (that includes the undoped mandrel) can be estimated[8] as $\rho\Delta r > 32(\pm6)$ mg/cm^2.
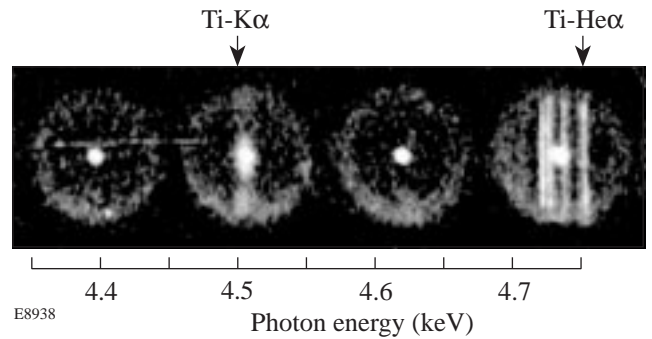
E8938

Figure 75.27
Part of the array images from target shot (b). The Ti^{20+} lines are seen to be emitted from the periphery of the target. On the other hand, a ring of emission at the wavelength of Ti Kα line is seen to be emitted around the compressed core. The Kα line is excited by core radiation, and its image delineates the cold shell at peak compression (see Fig. 75.28).

Figure 75.27 indicates that the Kα linewidth is insufficient for imaging the full extent of the cold shell in the dispersion direction. Since no limitation of field of view applies to the perpendicular direction, the Kα image is elliptically shaped. The vertical profile of the Kα emission shows the true dimension of the cold shell. By combining successive images in the vertical direction, we can obtain at least a qualitative view of the 2-D image of the cold shell. As mentioned above, in future high-performance implosions a single image may be sufficient for obtaining the 2-D image of the cold shell.

Using vertical lineouts in Fig. 75.27 we can obtain the dimensions of the cold shell in that direction. Figure 75.29(a) shows two such lineouts: (a) through the center of the second image from the left ("on Kα") and (b) an average of lineouts through the centers of the neighboring images on each side ("off Kα"). The peaks of the two profiles varied by about 10% (possibly due to fluctuations in pinhole sizes) and were normalized to the same height. The difference between these two curves [shown in Fig. 75.29(b)] delineates a ring-shaped layer of cold Ti-doped shell. Changing the relative intensity of the two profiles in Fig. 75.29(a) within the 10% uncertainty changes mostly the central minimum in Fig. 75.29(b), but not

the overall shape and dimensions of the intensity ring. Alternative off-Kα profiles could be chosen by moving above and below the Kα image in Fig. 75.27 (sufficiently for the Kα emission to disappear); however, the closeness of peak intensity of the two profiles in Fig. 75.29(a) indicates that the choice adopted here is adequate. The nonuniformity of the implosion seen in the images of Fig. 75.27 is also evident in Fig. 75.29(b). Figure 75.29(a) also shows Kα emission at a ~300-μm radius. This delineates the position of the cold shell during the laser pulse, when it is pumped by radiation and suprathermal electrons from the laser-heated material; this is further discussed in the following section. Figure 75.29(a) shows higher Kα intensity around +300 μm than around −300 μm, again indicating nonuniformity. This nonuniformity mirrors the nonuniformity during peak compression: the peak of the Kα profile around +80 μm is higher than the peak around −80 μm. This is surely the result of the irradiation nonuniformity as evident in Fig. 75.27: The coronal emission in the four
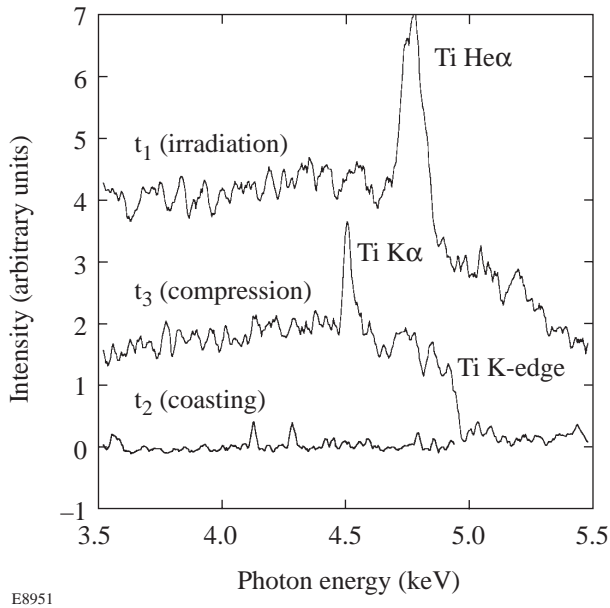
Figure 75.28
Spectra recorded by a streaked spectrograph at three times during the implosion of shot (b). The Ti^{20+} line emission occurs during the laser-pulse irradiation, t_1, whereas the K-edge absorption and the concomitant Kα line emission occur about ~1 ns after the end of the laser pulse, at the time of peak compression, t_3; t_2 is a time during the intervening coasting. These results confirm the conclusions from Fig. 75.27. Positive axis direction corresponds to downward direction in Fig. 75.27.

E8951

E8937a
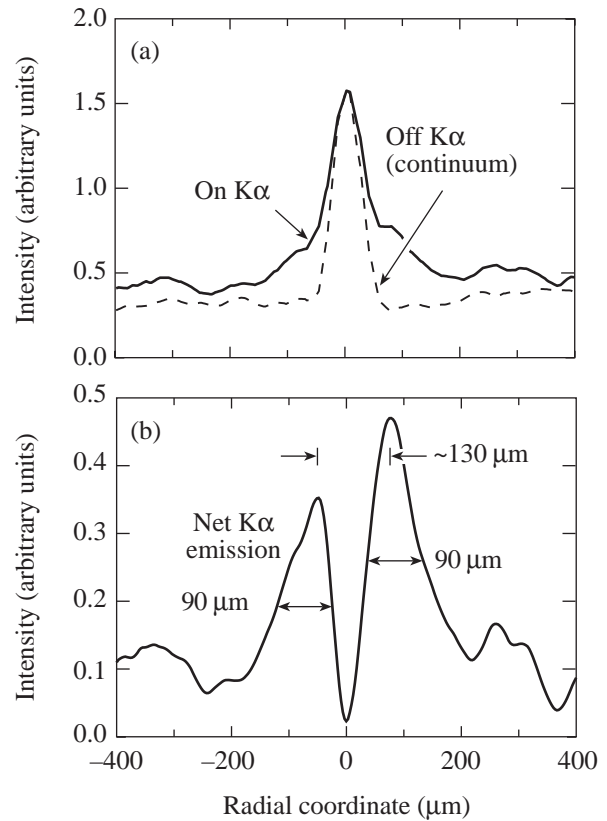
Figure 75.29
(a) Lineouts through images of Fig. 75.27, in the vertical direction (perpendicular to the direction of dispersion). The "on Kα" curve is through the center of the second image from the left; the "off Kα" curve is an average of lineouts through the centers of the two neighboring images on each side. (b) The difference between the two curves in (a) delineates the cold Ti-doped shell.

images is more intense on the lower half of the target, corresponding to a higher intensity of Kα (the positive axis in Figs. 75.29 and 75.30 corresponds to the downward direction in Fig. 75.27). Figure 75.29(b) indicates, for the cold shell, a ring of ~90-μm thickness and an average diameter of ~130 μm. In a previous experiment,[9] the Kα from a similar Ti-doped target was imaged in one dimension using a slit in front of a flat-crystal spectrometer. With one-dimensional (1-D) imaging, a ring-shaped source results in a flat-topped profile, and only the outer diameter of the ring can be reliably determined. The FWHM of the Kα profile in Ref. 9 (~250 μm) is similar to the FWHM in Fig. 75.29(b); however, the array yields an actual image of the ring of Kα emission (the profiles in Fig. 75.29 are slices through a 2-D image rather than 1-D images). The Kα emission profile and the K-edge absorption relate to the same target region, namely, the cold doped layer; thus, the ring thickness from Fig. 75.29(b) and the areal density derived from the K-edge absorption can be used to estimate the shell density. As noted above, the ablated part of the doped layer emits the Heα line of titanium, whereas the unablated doped layer emits the Kα line. The thickness of the doped layer (~90 μm) found in Fig. 75.29(b) is larger than the actual thickness at peak compression because of the time integration. Also, the areal density estimated above was only a lower limit; thus, a lower limit for the density of the doped layer can be obtained by dividing the estimated $\rho\Delta r$ of that layer (22 mg/cm^2) by its thickness (~90 μm) to yield $\rho > 2$ g/cm^3. This low density (albeit only a lower limit) is to be expected in view of the deficient symmetry of the laser irradiation in this experiment. A better determination of the shell density can be obtained by (a) lowering the level of doping to avoid complete K-edge absorption and (b) time-gating the spectrometer to avoid smearing due to time integration.

Preheat Measurement Using Early Kα Emission

In addition to Kα emission excited by core radiation at peak compression, Kα radiation is also emitted during the laser-irradiation pulse. The latter emission can be seen in Fig. 75.27 (second image from the left) and in Fig. 75.29 as a weak ring of emission at a radius of ~300 μm. To better understand the origin of this emission, we simulate the transport through the target of radiation giving rise to Kα emission, both the primary (or pumping) radiation and the secondary (or fluorescent) Kα radiation. We use profiles of target parameters calculated by the one-dimensional code *LILAC* to compute the transport of radiation of photon energy above the Ti K-edge, flowing radially outward and inward. The radiation is derived from the OPLIB astrophysical opacity tables[11] using the LTE approximation. To calculate the pumping of Kα fluorescence we

must know the component of the total opacity (given by the tables) that is related to photoionization of K-shell electrons. At the K edge, this component is easily found from the K-edge jump in the opacity tables; for all higher photon energies we make use of its known dependence on photon energy. Finally, the Kα emission is transported along straight cords in the direction of observation, and the resulting profile is convolved with the instrumental broadening function (due to the pinhole's finite size).

Figure 75.30 compares the resulting Kα profile with the measured profile (from Fig. 75.29), normalized to the simulated profile. Two ring-shaped Kα emission zones are seen: an intense ring at a radius of ~80 μm and a weaker ring at a radius of ~300 μm. In the experiment (Fig. 75.27), only sections of each ring are observed (along the vertical axis) because the crystal limits the field of view in the direction of dispersion. The simulations show that the strong, inner ring is emitted around peak compression and is pumped by outgoing core radiation; on the other hand, the weak, outer ring is emitted during the laser-irradiation pulse and is pumped by ingoing coronal radiation. The nonuniformity in the measured image (higher intensity at positive radial distances) was discussed above. Figure 75.30 shows that the position of the cold shell during the laser pulse and during peak compression is in rough agreement with one-dimensional code predictions, in spite of the marked nonuniformity. It should be noted, however, that the inner, undoped shell is not detected by the Kα emission;

E9010
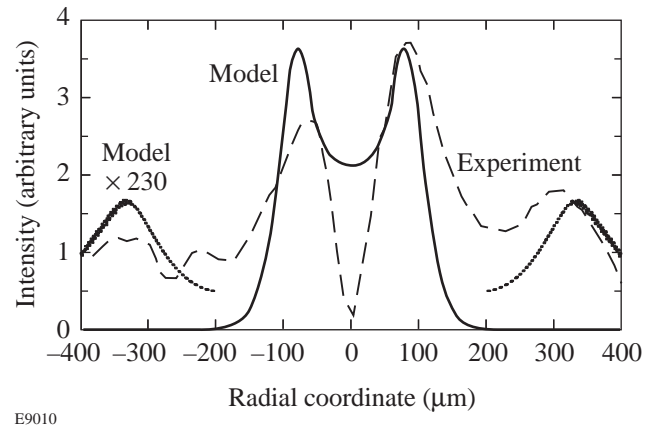
Figure 75.30
Measured and simulated radial profile of Kα emission for target shot (b). The inner ring of ~80-μm radius marks the position of the cold shell around the time of peak compression and is pumped by core radiation. The outer ring of ~300-μm radius marks the position of the shell during the laser pulse and is pumped by coronal radiation. The simulation includes only radiation transport, and the required multiplication by a factor of 230 shows that the outer ring is pumped by suprathermal electrons rather than by radiation.

the behavior of that segment of the shell is most indicative of target performance.

Whereas the position of the outer $K\alpha$ emission ring is quite well predicted by the code, its intensity is not: we must multiply its calculated intensity by ~230 to match the experiment. The only obvious explanation is that the outer ring of $K\alpha$ emission is mostly excited not by radiation but by suprathermal electrons, which are not included in the simulations. This question can be asked: How does the assumption of LTE in the radiation-transport calculations affect these conclusions? First, the LTE assumption affects mostly the intensity of the emission rings rather than their position. Second, departures from LTE would be more severe in the outer ring (of lower density) and would reduce the radiation available for pumping. Thus, the outer $K\alpha$ ring would be even weaker with respect to the inner $K\alpha$ ring than with the LTE calculations.

We now estimate the total preheat energy E_{ph} deposited in the target, based on the energy $E_{K\alpha}$ of electron-excited $K\alpha$ emission. The total $K\alpha$ energy of the outer ring, measured by a spatially integrating spectrometer, is $E_{K\alpha}$ ~10 mJ. For suprathermal-electron temperatures T_h above ~10 keV the ratio $R = E_{ph}/E_{K\alpha}$ tends to a constant independent of T_h. For medium-Z elements this constant is ~170;[12] thus, the preheat energy deposited in the titanium part of the shell is ~10 mJ $\times$ 170 = 1.7 J. To estimate the total preheat of the Ti-doped shell we note that the deposition rate for electrons in CH (over a very wide electron energy range) is ~10 times higher than that in Ti at 2% concentration;[13] thus, the preheat energy deposited in the doped shell is ~17 J. Since about half of the unablated shell is doped, this brings the total preheat energy to ~34 J. This estimate of preheat energy is independent of T_h; it only assumes that T_h is well above ~10 keV. The suprathermal electrons surmised from the $K\alpha$ emission can give rise to fast (or suprathermal) ions. In fact, total fast-ion energies of the order of 10 J (and ion energies >> 10 keV) have been measured by the charged-particle spectrometer on similar OMEGA target shots; thus, the two measurements are consistent.

In conclusion, a simple imaging method for laser-fusion experiments has been demonstrated. Placing a multi-pinhole array in front of a flat-crystal spectrometer yields monochromatic, two-dimensional images with an ~100- to 150-μm field of view, sufficient for imaging cores of highly compressed targets. Images of the whole target are also obtained, with an ~100-eV bandwidth of the continuum. The method was applied to imaging the $K\alpha$ fluorescence, shown to be excited by the core radiation at peak compression. This latter method yields the image of the cold shell at peak compression without using backlighting. Sufficient intensity has been shown to be obtained with 25-μm pinholes and a flat, nonfocusing diffracting crystal. Additionally, high spectral resolution was shown to be obtained with the array. This is particularly useful when measuring lines from the laser-interaction region, where the size of the target limits the spectral resolution to ~100, whereas with the array, the resolution can be five times higher. Finally, preheat in the amount of ~40 J was deduced from $K\alpha$ emission during the laser pulse, which appears as an outer ring of ~300-μm radius.

ACKNOWLEDGMENT

REFERENCES

1. C. L. S. Lewis and J. McGlinchey, Opt. Commun. **53**, 179 (1985).

2. J.-C. Kieffer *et al.*, Appl. Opt. **28**, 4333 (1989).

3. C. Brown *et al.*, Rev. Sci. Instrum. **68**, 1099 (1997).

4. F. J. Marshall and J. A. Oertel, Rev. Sci. Instrum. **68**, 735 (1997).

5. M. Vollbrecht *et al.*, J. Quant. Spectrosc. Radiat. Transf. **58**, 965 (1997).

6. H. Azechi *et al.*, Appl. Phys. Lett. **37**, 998 (1980).

7. T. R. Boehly, R. S. Craxton, T. H. Hinterman, J. H. Kelly, T. J. Kessler, S. A. Kumpan, S. A. Letzring, R. L. McCrory, S. F. B. Morse, W. Seka, S. Skupsky, J. M. Soures, and C. P. Verdon, Rev. Sci. Instrum. **66**, 508 (1995).

8. B. Yaakobi, F. J. Marshall, D. K. Bradley, J. A. Delettrez, R. S. Craxton, and R. Epstein, Phys. Plasmas **4**, 3021 (1997).

9. B. Yaakobi and F. J. Marshall, J. Quant. Spectrosc. Radiat. Transfer **61**, in press.

10. D. J. Botto, J. McEnnan, and R. H. Pratt, Phys. Rev. A **18**, 580 (1978).

11. M. F. Argo and W. F. Huebner, J. Quant. Spectrosc. Radiat. Transfer **16**, 1091 (1976).

12. B. Yaakobi, J. Delettrez, L. M. Goldman, R. L. McCrory, W. Seka, and J. M. Soures, Opt. Commun. **41**, 355 (1982).

13. G. Knop and W. Paul, in *Alpha-, Beta- and Gamma-Ray Spectroscopy*, 1st ed., edited by K. Siegbahn (North-Holland, Amsterdam, 1965), Vol. 1, p. 12; L. V. Spencer, *Energy Dissipation by Fast Electrons*, National Bureau of Standards, Monograph 1 (U.S. Government Printing Office, Washington, DC, 1959).

Forward and Backward Stimulated Brillouin Scattering of Crossed Laser Beams

Stimulated Brillouin scattering (SBS) in a plasma is the decay of an incident (pump) light wave into a frequency-downshifted (Stokes) light wave and an ion-acoustic (sound) wave.[1] It is important in direct[2] and indirect[3] inertial confinement fusion (ICF) experiments because it scatters the laser beams away from the target, thereby reducing the energy available to drive the compressive heating of the nuclear fuel.

The SBS of an isolated beam has been studied in detail. Backward SBS was studied in numerous early papers, and near-forward, sideward, and near-backward SBS were studied in some recent papers.[4–8] Because beams overlap in the coronal plasma surrounding the nuclear fuel, it is also important to analyze SBS (and other parametric instabilities) driven by two (or more) crossed beams. For some scattering angles the SBS geometries allow the pump waves to share daughter waves.[9–11] Because the growth of these daughter waves is driven by two pump waves (rather than one), the growth rates associated with these scattering angles are higher than the growth rates associated with other scattering angles. Such is the case for forward and backward SBS, in which the Stokes wave vectors bisect the angle between the pump wave vectors.

The outline of this article is as follows: (1) We derive the equations governing forward and backward SBS. (2) We solve the linearized equations governing the transient phase of the instability. These equations differ from the linearized equations governing the SBS of an isolated beam[7] because the forward and backward SBS of crossed beams each involve one Stokes wave and two sound waves (rather than one). (3) We solve the nonlinear equations governing the steady state of the instability. These equations describe the nonlinear competition between forward and backward SBS. (4) We discuss the entire evolution of forward and backward SBS. Finally, (5) we summarize the main results of the article.

In the Appendix we show that, in steady state, the equations governing the simultaneous near-forward and near-backward SBS of an isolated beam are equivalent to the equations governing the simultaneous forward and backward SBS of crossed beams; thus, many results of this article also apply to the SBS of an isolated beam.

Governing Equations

The SBS of crossed beams is governed by the Maxwell wave equation[1]

$$\left(\partial_{tt}^2 + \omega_e^2 - c^2\nabla^2\right)A_h = -\omega_e^2 n_l A_h \tag{1}$$

for the electromagnetic potential, together with the sound-wave equation[1]

$$\left(\partial_{tt}^2 + c_s^2 - \nabla^2\right)n_l = \frac{1}{2}c_s^2\nabla^2\langle A_h^2\rangle. \tag{2}$$

The electromagnetic potential $A_h = \left(v_h/c_s\right)\left(m_e/m_i\right)^{1/2}$ is the quiver speed of electrons in the high-frequency electric field divided by a characteristic speed that is of the order of the electron thermal speed; n_l is the low-frequency electron density fluctuation associated with the sound wave divided by the background electron density; and the $\langle\ \rangle$ signify that only the low-frequency response to the ponderomotive force was retained.

The geometry associated with forward SBS is shown in Fig. 75.31(a). The forward SBS of beam 1 is subject to matching conditions of the form

$$\omega_1 = \omega_f + \omega_{s1}, \quad \mathbf{k}_1 = \mathbf{k}_f + \mathbf{k}_{s1}, \tag{3}$$

where $(\omega_1,\mathbf{k}_1)$ and $(\omega_f,\mathbf{k}_f)$ satisfy the light-wave dispersion equation $\omega^2 = \omega_e^2 + c^2k^2$, and $(\omega_{s1}, \mathbf{k}_{s1})$ satisfies the sound-wave dispersion equation $\omega^2 = c_s^2k^2$. Similar matching conditions apply to the forward SBS of beam 2. Because the sound frequencies depend on the magnitudes of the sound-wave vectors, but not on their directions, $\omega_{s2} = \omega_{s1} = \omega_s$.

(a)

(b)
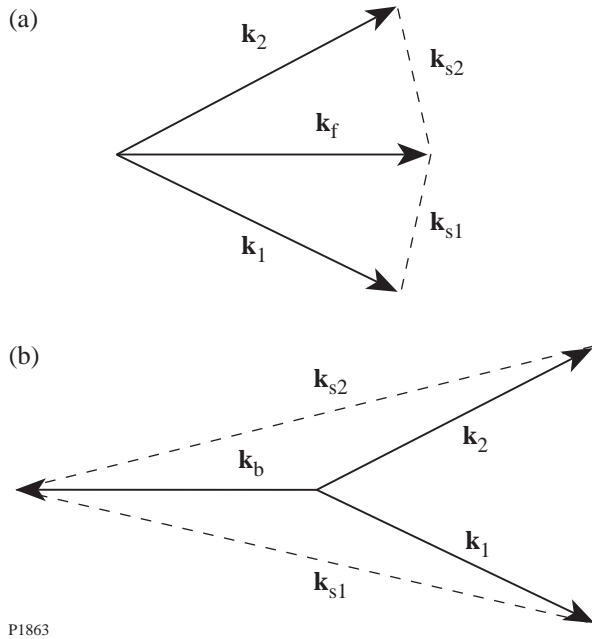
P1863

Figure 75.31
Geometry associated with the SBS of crossed laser beams: (a) forward SBS; (b) backward SBS.

By substituting the Ansätze

$$A_h = \left[A_1 \exp\left(i\mathbf{k}_1 \cdot \mathbf{x} - i\omega_0 t\right) + A_2 \exp\left(i\mathbf{k}_2 \cdot \mathbf{x} - i\omega_0 t\right) \right.$$
$$\left. + A_f \exp\left(i\mathbf{k}_f \cdot \mathbf{x} - i\omega_f t\right) \right] + c.c. \qquad (4)$$

and

$$n_l = N_1 \exp\left(i\mathbf{k}_{s1} \cdot \mathbf{x} - i\omega_s t\right)$$
$$+ N_2 \exp\left(i\mathbf{k}_{s2} \cdot \mathbf{x} - i\omega_s t\right) + c.c. \qquad (5)$$

in Eqs. (1) and (2), one can show that

$$\partial_z A_f = i\left(\omega_e^2 / 2\omega_0 v_0\right)\left(A_1 N_1^* + A_2 N_2^*\right), \qquad (6)$$

$$\left(\partial_t + v_{s1}\right)N_1^* = -i\left(\omega_s^2 / 2\omega_s\right)A_1^* A_f + v_{s1} n^*, \qquad (7)$$

$$\left(\partial_t + v_{s2}\right)N_2^* = -i\left(\omega_s^2 / 2\omega_s\right)A_2^* A_f + v_{s2} n^*. \qquad (8)$$

Because $\omega_s \ll \omega_0$, we made the approximation in Eq. (6) that the frequency and group speed of the scattered light wave equal the frequency and group speed v_0 of the pump waves, respec-

tively. In Eqs. (7) and (8) $v_{s1} N_1^*$ and $v_{s2} N_2^*$ are phenomeno-logical terms that model the Landau damping of the sound waves,[12] and $v_{s1} n^*$ and $v_{s2} n^*$ are phenomenological terms that maintain the density fluctuations associated with the sound waves at their common noise level n^* in the absence of instability. Because the Landau-damping rates depend on the magnitudes of the sound-wave vectors, but not on their direc-tion, $v_{s2} = v_{s1} = v_s$.

Equations (6)–(8) describe the initial (transient) evolution of SBS. In steady state,

$$d_z A_f = \mu_f \left(|A_1|^2 + |A_2|^2\right) A_f, \qquad (9)$$

where

$$\mu_f = \omega_e^2 \omega_s^2 / 4\omega_0 \omega_s v_s v_0. \qquad (10)$$

Apart from a factor of $|A_1|^2$ or $|A_2|^2$, μ_f is the spatial growth rate of forward SBS in the strongly damped regime.[7] The forward-scattered intensity $F = |A_f|^2$ satisfies the equation

$$d_z F = 2\mu_f \left(P_1 + P_2\right) F, \qquad (11)$$

where $P_1 = |A_1|^2$ and $P_2 = |A_2|^2$ are the pump intensities.

The geometry associated with backward SBS is shown in Fig. 75.31(b). The backward SBS of beam 1 is subject to matching conditions of the form

$$\omega_1 = \omega_b + \omega_{s1}, \quad \mathbf{k}_1 = \mathbf{k}_b + \mathbf{k}_{s1}, \qquad (12)$$

where $(\omega_1, \mathbf{k}_1)$ and $(\omega_b, \mathbf{k}_b)$ satisfy the light-wave dispersion equation, and $(\omega_{s1}, \mathbf{k}_{s1})$ satisfies the sound-wave dispersion equation. Similar matching conditions apply to the backward SBS of beam 2: as in forward SBS, $\omega_{s2} = \omega_{s1} = \omega_s$.

By adding to Ansatz (4) the term

$$A_b \exp\left(i\mathbf{k}_b \cdot \mathbf{x} - i\omega_b t\right) + c.c. \qquad (13)$$

and to Ansatz (5) the terms

$$N_1 \exp\left(i\mathbf{k}_{s1} \cdot \mathbf{x} - i\omega_s t\right) + N_2 \exp\left(i\mathbf{k}_{s2} \cdot \mathbf{x} - i\omega_s t\right) + c.c. \quad (14)$$

associated with backward SBS, one can show that

$$-\partial_z A_b = i\left(\omega_e^2/2\omega_0 v_0\right)\left(A_1 N_1^* + A_2 N_2^*\right), \quad (15)$$

$$\left(\partial_t + v_{s1}\right)N_1^* = -i\left(\omega_s^2/2\omega_s\right)A_1^* A_b + v_{s1} n^*, \quad (16)$$

$$\left(\partial_t + v_{s2}\right)N_2^* = -i\left(\omega_s^2/2\omega_s\right)A_2^* A_b + v_{s2} n^*. \quad (17)$$

As in forward SBS, $v_{s2} = v_{s1} = v_s$. In its transient (linear) phase, backward SBS is independent of forward SBS.

In steady state, the backward-scattered intensity $B = |A_b|^2$ satisfies the equation

$$-d_z B = 2\mu_b\left(P_1 + P_2\right)B, \quad (18)$$

where μ_b is given by Eq. (10) and the values of ω_s and v_s associated with backward SBS. Apart from a factor of $|A_1|^2$ or $|A_2|^2$, μ_b is the spatial growth rate of backward SBS in the strongly damped regime.[7]

In the high-gain regime, the intensities of the scattered light waves as they exit the plasma are comparable to the intensities of the pump waves as they enter the plasma, and one must account for the depletion of the pump waves within the plasma. In steady state, the pump intensities satisfy the equations

$$d_z P_1 = -2\mu_f F P_1 - 2\mu_b B P_1, \quad (19)$$

$$d_z P_2 = -2\mu_f F P_2 - 2\mu_b B P_2, \quad (20)$$

where we made the approximation that the evolution of the pump waves is one dimensional. One can verify Eqs. (19) and (20) by applying the principle of power conservation to Eqs. (11) and (18).

Linear Analysis of the Transient Phase

The forward SBS of crossed beams consists of two mirror-image processes that share the same Stokes wave and, hence, are governed by the coupled equations (6)–(8). By making the substitutions $\omega_0^{1/2} A_f \rightarrow A_f$, $i\omega_e N_1^*/\omega_s^{1/2} \rightarrow N_1$, $i\omega_e N_2^*/\omega_s^{1/2} \rightarrow N_2$, $i\omega_e n^*/\omega_s^{1/2} \rightarrow n$, and $z/v_0 \rightarrow z$, one can rewrite these equations as

$$\partial_z A_f = \gamma_{f1} N_1 + \gamma_{f2} N_2, \quad (21)$$

$$\left(\partial_t + v_s\right)N_1 = \gamma_{f1} A_f + v_s n, \quad (22)$$

$$\left(\partial_t + v_s\right)N_2 = \gamma_{f2} A_f + v_s n, \quad (23)$$

where

$$\gamma_{f1} = \omega_e \omega_s |A_1|/2(\omega_0 \omega_s)^{1/2}, \quad (24)$$

$$\gamma_{f2} = \omega_e \omega_s |A_2|/2(\omega_0 \omega_s)^{1/2}. \quad (25)$$

A_f is proportional to the action amplitude of the Stokes wave, and N_1 and N_2 are proportional to the action amplitudes of the sound waves. In the absence of damping, γ_{f1} and γ_{f2} are the temporal growth rates of the forward SBS of beams 1 and 2, respectively, in an infinite plasma.

By using the combined amplitudes

$$N_+ = \left(\gamma_{f1} N_1 + \gamma_{f2} N_2\right)/\gamma_f, \quad (26)$$

$$N_- = \gamma_f \left(N_1/\gamma_{f1} - N_2/\gamma_{f2}\right), \quad (27)$$

where $\gamma_f = \left(\gamma_{f1}^2 + \gamma_{f2}^2\right)^{1/2}$, one can rewrite Eqs. (21)–(23) as

$$\partial_z A_f = \gamma_f N_+, \quad (28)$$

$$\left(\partial_t + v_s\right)N_+ = \gamma_f A_f + v_s n_+, \quad (29)$$

$$\left(\partial_t + v_s\right)N_- = v_s n_-, \quad (30)$$

where $n_+ = n\left(\gamma_{f1} + \gamma_{f2}\right)/\gamma_f$ and $n_- = n\gamma_f\left(1/\gamma_{f1} - 1/\gamma_{f2}\right)$. Equations (28) and (29) are equivalent to the equations governing the forward SBS of an isolated beam,[7] and Eq. (30) is simple. Consequently, the solutions of Eqs. (28)–(30) can be written in the form

$$A_f(z,t) = \int_0^t \int_0^z v_s n_+ G_f(z - z', t - t')dz' dt', \quad (31)$$

$$N_+(z,t) = \int_0^t \int_0^z v_s n_+ G_+(z - z', t - t')dz' dt', \quad (32)$$

$$N_-(z,t) = \int_0^t \int_0^z v_s n_- G_-(z - z', t - t')dz' dt', \quad (33)$$

where the Green functions

$$G_f(z,t) = \gamma_f \, I_0\left[2\gamma_f \, (zt)^{1/2}\right] \exp(-\nu_s t), \qquad (34)$$

$$G_+(z,t) = \gamma_f \, (t/z)^{1/2} \, I_1\left[2\gamma_f \, (zt)^{1/2}\right]$$
$$\times \exp(-\nu_s t) + \delta(z) \, \exp(-\nu_s t), \qquad (35)$$

$$G_-(z,t) = \delta(z) \, \exp(-\nu_s t). \qquad (36)$$

In Eqs. (34) and (35), I_m is the modified Bessel function of the first kind, of order m. The original amplitudes N_1 and N_2 are determined by Eqs. (32) and (33) and the inversion equations

$$N_1 = (\gamma_{f1}/\gamma_f)\left[N_+ + (\gamma_{f2}^2/\gamma_f^2)N_-\right], \qquad (37)$$

$$N_2 = (\gamma_{f2}/\gamma_f)\left[N_+ - (\gamma_{f1}^2/\gamma_f^2)N_-\right]. \qquad (38)$$

Solutions (31)–(33) describe the growth and dissipative saturation of forward SBS. By analyzing the time dependence of the Green functions, one can show that the saturation time

$$t_s \sim \gamma_f^2 z / \nu_s^2. \qquad (39)$$

The steady-state limits of solutions (31)–(33) are

$$A_f(z,\infty) = (n_+ \nu_s/\gamma_f)\left[\exp(\gamma_f^2 z/\nu_s) - 1\right], \qquad (40)$$

$$N_+(z,\infty) = n_+ \exp(\gamma_f^2 z/\nu_s), \qquad (41)$$

$$N_-(z,\infty) = n_-. \qquad (42)$$

Notice that $\gamma_f^2/\nu_s \nu_0 = \mu_f(|A_1|^2 + |A_2|^2)$, in agreement with Eq. (9). If the interaction length exceeds a few gain lengths, one can model Stokes generation as Stokes amplification with an incident amplitude $A_f(0) = (n_+ \nu_s/\gamma_f)$.

The backward SBS of crossed beams also consists of two mirror-image processes that share a Stokes wave and are governed by Eqs. (21)–(25), with f replaced by b and z replaced by $l-z$; thus, Eqs. (26)–(42), and the conclusions drawn from them, also apply to backward SBS. Equa-

tions (21)–(23) apply to other parametric instabilities driven by crossed pump waves, provided that one type of daughter wave is strongly damped.

Nonlinear Analysis of the Steady State

The simultaneous forward and backward SBS of crossed beams is governed by Eqs. (11) and (18)–(20). By making the substitution $P_1 + P_2 \to P$, one can rewrite these equations as

$$d_z F = 2\mu_f PF, \qquad (43)$$

$$-d_z B = 2\mu_b PF, \qquad (44)$$

$$d_z P = -2(\mu_f F + \mu_b B)P. \qquad (45)$$

Equations (43)–(45) apply to other simultaneous parametric instabilities driven by crossed pump waves, provided that one type of daughter wave is strongly damped. For SBS, $\mu_b = \mu_f = \mu$,[7] and one can use the substitution $2\mu z \to z$ to rewrite Eqs. (43)–(45) in the simple form

$$d_z F = PF, \qquad (46)$$

$$-d_z B = PB, \qquad (47)$$

$$d_z P = -(F+B)P. \qquad (48)$$

The substitutions $F/P(0) \to F$, $B/P(0) \to B$, $P/P(0) \to P$, and $P(0)z \to z$ nondimensionalize Eqs. (46)–(48) but leave them unchanged in form. Because the solutions of Eqs. (46)–(48) are complicated, it is instructive to review the limiting solutions that apply to forward and backward SBS separately.

1. Forward SBS

In the absence of backward SBS, Eqs. (46)–(48) reduce to

$$d_z F = PF, \qquad (49)$$

$$d_z P = -FP. \qquad (50)$$

It follows from these equations that

$$P + F = 1 + N_f, \qquad (51)$$

where $N_f = F(0)$ is incident (noise) intensity of the forward-scattered wave. Since $P \geq 0$, it follows from Eq. (51) that

$$S_f \leq 1 + N_f, \tag{52}$$

where $S_f = F(l)$ is the output (signal) intensity of the forward-scattered wave and l is the gain length of forward SBS. Equation (52) reflects the fact that the signal intensity cannot exceed the total input intensity.

By substituting Eq. (51) in Eq. (49), one can show that

$$\left(1 + N_f\right)z = \log\left[\frac{F}{N_f\left(1 + N_f - F\right)}\right]. \tag{53}$$

Equation (53) determines the interaction distance z required to produce the forward-scattered intensity F. By inverting this equation, one finds that

$$F(\zeta) = \frac{N_f\left(1 + N_f\right)}{N_f + \exp(-\zeta)}, \tag{54}$$

where $\zeta = \left(1 + N_f\right)z$. Solution (54) is consistent with Eq. (52).

The normalized intensities of the pump and Stokes waves in a semi-infinite plasma are plotted as functions of the gain distance z in Fig. 75.32, for the case in which $N_f = 10^{-6}$. As the Stokes intensity increases, the pump intensity decreases, in accordance with Eq. (51). For future reference, notice that the initial growth of the Stokes wave from noise is driven by an undepleted pump wave.
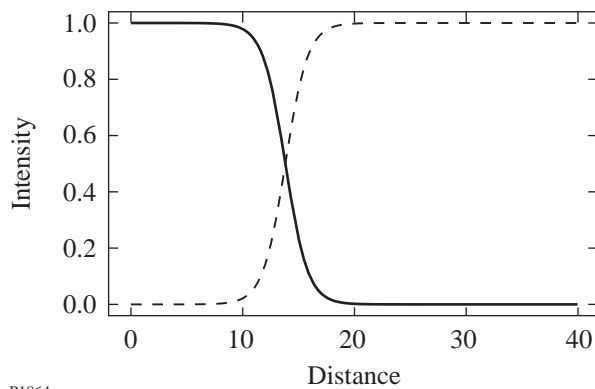
P1864

Figure 75.32
Normalized intensities plotted as functions of the gain distance for forward SBS in a semi-infinite plasma. The solid line represents the pump wave; the dashed line represents the Stokes wave. For forward SBS the output intensities from a finite plasma depend on the plasma length in the same way that the intensities within a semi-infinite plasma depend on the distance from the plasma boundary.

2. Backward SBS

In the absence of forward SBS, Eqs. (46)–(48) reduce to

$$-d_z B = PB, \tag{55}$$

$$d_z P = -BP. \tag{56}$$

It follows from these equations that

$$P - B = 1 - S_b, \tag{57}$$

where $S_b = B(0)$ is the output (signal) intensity of the backward-scattered wave. Since $P \geq 0$, it follows from Eq. (57) that

$$S_b \leq 1 + N_b, \tag{58}$$

where $N_b = B(l)$ is the incident (noise) intensity of the backward-scattered wave and l is the gain length of backward SBS. Equation (58) reflects the fact that the signal intensity cannot exceed the total input intensity.

By substituting Eq. (57) in Eq. (55), one can show that

$$\left(1 - S_b\right)z = \log\left[S_b\left(1 - S_b + B\right)/B\right]. \tag{59}$$

The signal intensity is determined by Eq. (59) and the condition $B(l) = N_b$. By inverting Eq. (59), with S_b known, one finds that

$$B(\zeta) = \frac{S_b\left(1 - S_b\right)}{\exp(\zeta) - S_b}, \tag{60}$$

where $\zeta = \left(1 - S_b\right)z$. Solution (60), which was first obtained by Tang,[13] is consistent with Eq. (58).

The normalized output intensity of the Stokes wave is plotted as a function of the gain length l in Fig. 75.33(a), for the case in which $N_b = 10^{-6}$. The normalized intensities of the pump and Stokes waves within the plasma are plotted as functions of the gain distance z in Fig. 75.33(b), for the case in which $N_b = 10^{-6}$ and $l = 30$. Because the pump and Stokes waves propagate in opposite directions, the initial growth of the Stokes wave from noise is driven by a depleted pump wave [Fig. 75.33(b)]. Consequently, when pump depletion is important ($l > 10$), the rate at which the Stokes output intensity increases with gain length is slower for backward SBS [Fig. 75.33(a)] than for forward SBS (Fig. 75.32). Backward SBS scatters the pump power less efficiently than forward SBS.
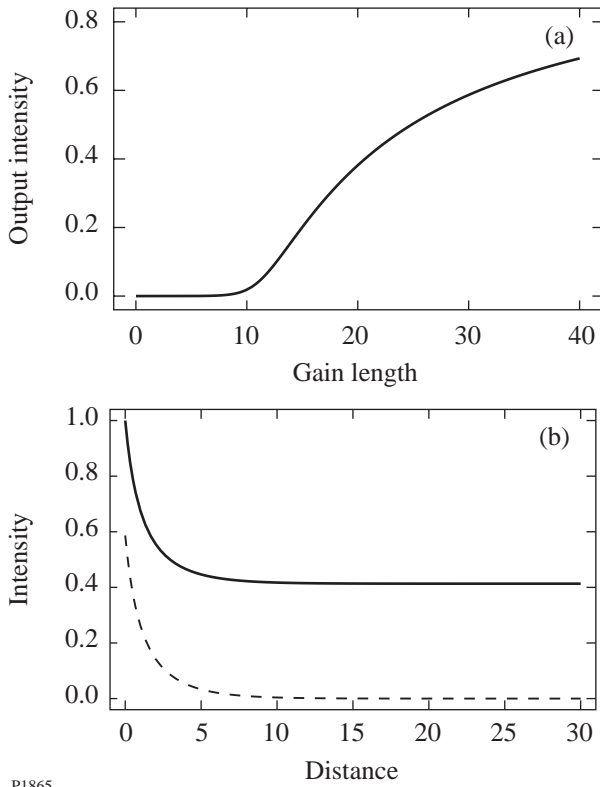
Figure 75.33

(a) Normalized output intensity of the Stokes wave plotted as a function of the gain length l for backward SBS. (b) Normalized intensities within the plasma plotted as functions of the gain distance for $l = 30$. The solid line represents the pump wave; the dashed line represents the Stokes wave.

3. Simultaneous Forward and Backward SBS

When forward and backward SBS occur simultaneously, it follows from Eqs. (46)–(48) that

$$P + F - B = 1 + N_f - S_b \tag{61}$$

and

$$FB = N_f S_b. \tag{62}$$

Equation (61) is a generalization of equations that apply to the forward and backward instabilities separately, whereas Eq. (62) is peculiar to the combined instability. Since $P \geq 0$, it follows from Eq. (61) that

$$S_f + S_b \leq 1 + N_f + N_b. \tag{63}$$

Equation (63) reflects the fact that the total signal intensity cannot exceed the total input intensity. It follows from Eqs. (62) and (63) that

$$S_f \leq N_f + \frac{N_f}{N_f + N_b}, \tag{64}$$

$$S_b \leq N_b + \frac{N_b}{N_f + N_b}. \tag{65}$$

By substituting Eqs. (61) and (62) in Eq. (46), one can show that

$$d_z F = (R_+ - F)(R_- + F), \tag{66}$$

where

$$\pm 2R_\pm = 1 + N_f - S_b \pm \left[(1 + N_f - S_b)^2 + 4N_f S_b \right]^{1/2}. \tag{67}$$

It follows from Eq. (66) that

$$(R_+ + R_-)z = \log \left[\frac{(R_+ - N_f)(R_- + F)}{(R_+ - F)(R_- + N_f)} \right]. \tag{68}$$

S_b is determined by Eq. (68) and the condition $B(l) = N_b$, which is equivalent to the condition $F(l) = (N_f / N_b) S_b$. By inverting Eq. (68), with S_b known, one finds that

$$F(\zeta) = \frac{R_+ (R_- + N_f) \exp(\zeta) - R_- (R_+ - N_f)}{(R_- + N_f) \exp(\zeta) + (R_+ - N_f)}, \tag{69}$$

where $\zeta = (R_+ + R_-)z$. Solution (69) is consistent with Eq. (64). For the common case in which $1 - S_b \gg N_f$, one can use the approximate roots

$$R_+ \approx 1 - S_b + N_f / (1 - S_b), \tag{70}$$

$$R_- \approx N_f S_b / (1 - S_b), \tag{71}$$
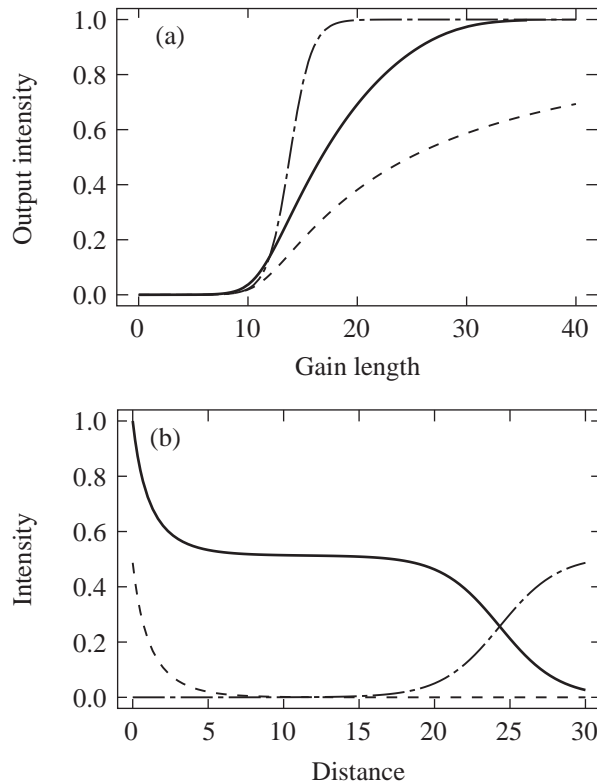
to rewrite Eqs. (68) and (69) as

$$(1 - S_b)z \approx \log \left\{ \frac{(1 - S_b) \left[N_f S_b + (1 - S_b) F \right]}{(1 - S_b - F) N_f} \right\} \tag{72}$$

and

$$F(\zeta) \approx \frac{N_f (1 - S_b) \left[\exp(\zeta) - S_b \right]}{N_f \exp(\zeta) + (1 - S_b)^2}, \tag{73}$$

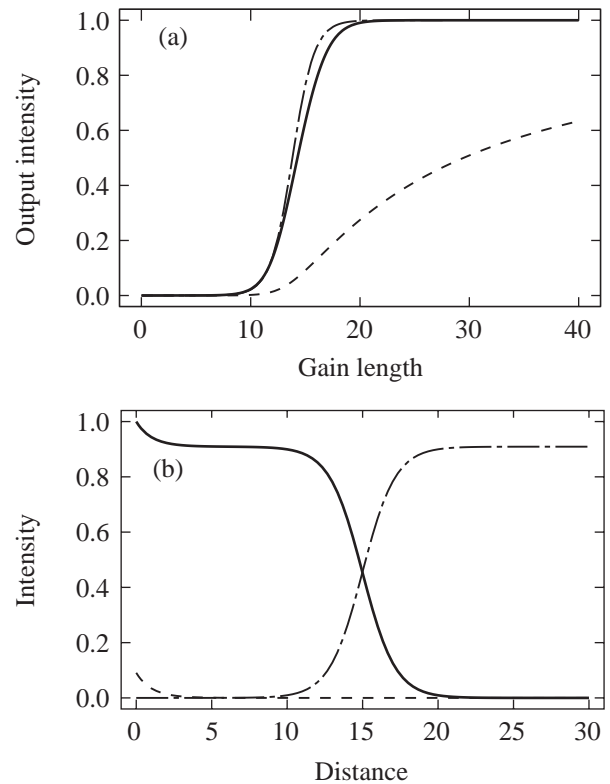respectively, where $\zeta \approx (1 - S_b)z$.

The normalized (total) output intensity of the (forward and backward) Stokes waves is plotted as a function of the gain length l in Fig. 75.34(a), for the case in which $N_b = N_f = 10^{-6}$. When pump depletion is unimportant ($l < 10$), the Stokes output intensity of the combined instability is the sum of the Stokes output intensities of the forward and backward instabilities. The normalized intensities of the pump and Stokes waves within the plasma are plotted as functions of the gain distance z in Fig. 75.34(b) for the case in which $N_b = N_f = 10^{-6}$ and $l = 30$. The initial growth of both Stokes waves from noise is driven by a depleted pump wave. Consequently, when pump depletion is important ($l > 10$), the rate at which the Stokes output intensity increases with gain length is slower for the combined instability than for the forward instability [Fig. 75.34(a)].

In Figs. 75.32–75.34, the noise intensities for forward and backward SBS were equal. This choice made possible a fair comparison of the intrinsic scattering efficiencies of the two instabilities. The noise intensity for forward SBS is larger, however, than the noise intensity for backward SBS because the action sources that generate the light waves [Eq. (40) for forward SBS and its analog for backward SBS] are inversely proportional to the sound frequencies.[14] To illustrate how this imbalance affects the combined instability, the normalized output intensity of the Stokes waves is plotted as a function of the gain length in Fig. 75.35(a) for the case in which $N_f = 10^{-16}$ and $N_b = 10^{-7}$. The normalized intensities of the pump and Stokes waves within the plasma are plotted as functions of the gain distance in Fig. 75.35(b) for the case in which $N_f = 10^{-6}$, $N_b = 10^{-7}$, and $l = 30$. It is clear from the figures that forward SBS overwhelms backward SBS in steady state.

P1866

Figure 75.34
(a) Normalized output intensities plotted as functions of SBS gain length l. The forward and backward noise intensities are equal. The solid line represents the total output intensity for the combined instability. For comparison, the dot–dashed and dashed lines represent the output intensities when forward and backward SBS occur separately [Figs. 75.32 and 75.33(a), respectively]. (b) Normalized intensities within the plasma plotted as functions of the gain distance for $l = 30$. The solid line represents the pump wave, the dot–dashed line represents the forward Stokes wave, and the dashed line represents the backward Stokes wave.

P1866

Figure 75.35
(a) Normalized output intensities plotted as functions of SBS gain length l. The forward noise intensity exceeds the backward noise intensity by a factor of 10. The solid line represents the total output intensity for the combined instability. For comparison, the dot–dashed and dashed lines represent the output intensities when forward and backward SBS occur separately. (b) Normalized intensities within the plasma plotted as functions of the gain distance for $l = 30$. The solid line represents the pump wave, the dot–dashed line represents the forward Stokes wave, and the dashed line represents the backward Stokes wave.

Discussion

Initially, pump depletion is unimportant, and forward and backward SBS grow independently. This (linear) spatio-temporal growth is described by Eqs. (28)–(30). Since the growth rate $\gamma_f \propto (\sin\phi)^{1/2}$ [Eqs. (24) and (25)], the sound-wave damping rate $\nu_s \propto \sin\phi$, and the saturation time $t_s \propto 1/(\sin\phi)$ [Eq. (39)], where 2ϕ is the scattering angle, backward SBS grows and saturates more quickly than forward SBS.[7] The steady-state (nonlinear) spatial evolution of backward SBS is described by Eqs. (57) and (60). In the high-gain regime, backward SBS depletes the pump wave significantly [Fig. 75.33(b)]; thus, the spatiotemporal growth of forward SBS is driven by a pump wave whose intensity varies with distance, and Eqs. (31)–(36) do not apply as written. By making the substitutions $N_\pm/\gamma_f \to N_\pm$, $n_\pm/\gamma_f \to n_\pm$, and $\int_0^z [\gamma_f(z')]^2 dz' \to z$ in Eqs. (28)–(30), however, one can show that

$$\partial_z A_f = N_+, \tag{74}$$

$$(\partial_t + \nu_s)N_+ = A_f + \nu_s n_+, \tag{75}$$

$$(\partial_t + \nu_s)N_- = \nu_s n_-. \tag{76}$$

Since Eqs. (74)–(76) contain no variable coefficients, their solution can be inferred from Eqs. (31)–(36). It follows that the (linear) saturation time of forward SBS is given by Eq. (39), with $\gamma^2 z$ replaced by $\int_0^z [\gamma_f(z')]^2 dz'$. Since the saturation time is proportional to the (integrated) gain distance, the reduction of the gain distance by pump depletion shortens the saturation time of forward SBS. Since the steady-state (nonlinear) Eqs. (46)–(48) have a unique solution, the spatial evolution of the combined instability is given by Eqs. (61), (62), and (69), even though forward and backward SBS grow at different rates and saturate at different times. It is clear from Figs. 75.34 and 75.35 that the output intensity of the backward Stokes wave is lower in the presence of the forward Stokes wave than in its absence; thus, the combined instability is characterized by a burst of backward SBS followed by the ascendance of forward SBS.

The major theme of the **Nonlinear Analysis of the Steady State** section and the preceding discussion is that forward and backward SBS coexist and compete for the pump energy. One should remember that several other processes also coexist and modify this competition. These processes include double SBS,[9] which is made possible by a sound wave whose wave vector is the sum of the pump-wave vectors, and the transfer of energy between the pump waves[15–21] and the Bragg scattering of the pump waves,[16] both of which are made possible by a sound wave whose wave vector is the difference of the pump-wave vectors; thus, the interaction physics is even richer than the physics discussed herein.

Summary

In this article we studied in detail the simultaneous forward and backward SBS of crossed laser beams. We obtained new analytical solutions for the linearized equations governing the transient phase of the instability [Eqs. (21)–(23)] and the nonlinear equations governing the steady state [Eqs. (46)–(48)]. In their transient phases, forward and backward SBS grow independently. Initially, backward SBS grows more quickly than forward SBS. As the backward Stokes wave grows, it depletes the pump wave and modifies the growth of the forward Stokes wave. In steady state, forward SBS dominates the combined instability because the forward Stokes wave has a larger noise intensity from which to grow and forward SBS scatters the pump power more efficiently.

In the Appendix we show that the equations governing the simultaneous near-forward and near-backward SBS of an isolated beam are equivalent to the equations governing the simultaneous forward and backward SBS of crossed beams; thus, the results of this article also apply to the SBS of an isolated beam.

Appendix A: Forward and Backward SBS of an Isolated Laser Beam

In this appendix we show that the equations governing the simultaneous forward and backward SBS of an isolated beam are equivalent to the equations governing the simultaneous forward and backward SBS of crossed beams. The geometry associated with the forward SBS of an isolated beam is shown in Fig. 75.36(a). Each forward-scattering process is subject to matching conditions of the form

$$\omega_0 = \omega_f + \omega_s, \quad \mathbf{k}_0 = \mathbf{k}_f + \mathbf{k}_s, \tag{A1}$$

where $(\omega_0, \mathbf{k}_0)$ and $(\omega_f, \mathbf{k}_f)$ satisfy the light-wave dispersion equation $\omega^2 = \omega_e^2 + c^2 k^2$, and $(\omega_s, \mathbf{k}_s)$ satisfies the sound-
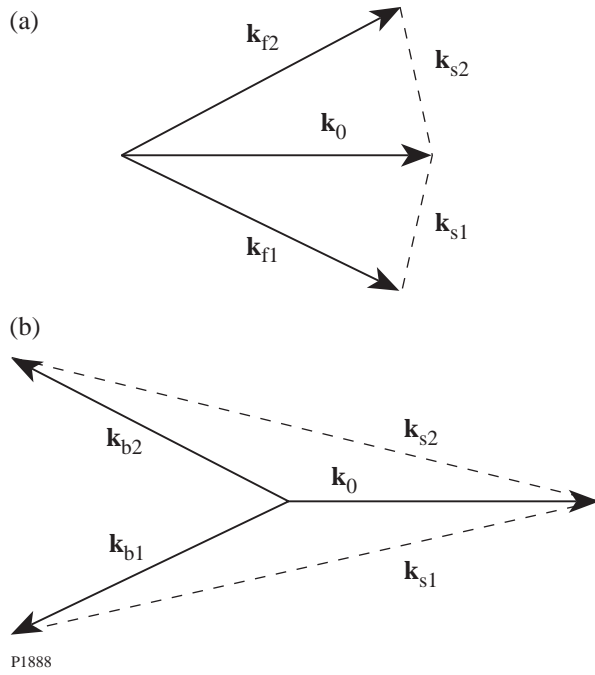
(a)

(b)

P1888

Figure 75.36
Geometry associated with the SBS of an isolated laser beam: (a) near-forward SBS; (b) near-backward SBS.

wave dispersion equation $\omega^2 = c_s^2 k^2$. Because the frequencies of the daughter waves depend on the magnitude of their wave vectors, but not on their directions, $\omega_{f2} = \omega_{f1} = \omega_f$ and $\omega_{s2} = \omega_{s1} = \omega_s$.

By substituting the Ansätze

$$A_h = \left[A_0 \exp\left(i\mathbf{k}_0 \cdot \mathbf{x} - i\omega_0 t\right) + A_{f1} \exp\left(i\mathbf{k}_{f1} \cdot \mathbf{x} - i\omega_f t\right) \right.$$
$$\left. + A_{f2} \exp\left(i\mathbf{k}_{f2} \cdot \mathbf{x} - i\omega_f t\right) \right] + c.c. \tag{A2}$$

and

$$n_l = N_1 \exp\left(i\mathbf{k}_{s1} \cdot \mathbf{x} - i\omega_s t\right)$$
$$+ N_2 \exp\left(i\mathbf{k}_{s2} \cdot \mathbf{x} - i\omega_s t\right) + c.c. \tag{A3}$$

into Eqs. (1) and (2), and making the slowly varying envelope approximation, one can show that each forward-scattering process is governed by equations of the form

$$\partial_z A_f = i\left(\omega_e^2 / 2\omega_0 v_0\right) A_0 N^*, \tag{A4}$$

$$\left(\partial_t + v_s\right) N^* = -i\left(\omega_s^2 / 2\omega_s\right) A_0^* A_f + v_s n^*. \tag{A5}$$

In Eq. (A5), $v_s N^*$ is a phenomenological term that models the Landau damping of the sound wave, and $v_s n^*$ is a phenomenological term that maintains the density fluctuations associated with the sound wave at their noise level n^* in the absence of instability. Because the Landau-damping rates depend on the magnitudes of the sound-wave vectors, but not on their directions, $v_{s2} = v_{s1} = v_s$. By making the substitutions $\omega_0^{1/2} A_f \rightarrow A_f$, $i\omega_e N^* / \omega_s^{1/2} \rightarrow N$, $i\omega_e n^* / \omega_s^{1/2} \rightarrow n$, and $z/v_0 \rightarrow z$, one can rewrite Eqs. (A4) and (A5) as

$$\partial_z A_f = \gamma_f N, \tag{A6}$$

$$\left(\partial_t + v_s\right) N = \gamma_f A_f + v_s n, \tag{A7}$$

where

$$\gamma_f = \omega_e \omega_s |A_0| / 2 \left(\omega_0 \omega_s\right)^{1/2}. \tag{A8}$$

Equations (A6) and (A7) are equivalent to Eqs. (28) and (29), the solution of which was described in the text.

Equations (A4) and (A5) describe the transient evolution of forward SBS. In steady state,

$$d_z A_f = \mu_f |A_0|^2 A_f, \tag{A9}$$

where

$$\mu_f = \omega_e^2 \omega_s^2 / 4\omega_0 \omega_s v_s v_0. \tag{A10}$$

Notice that $\mu_f |A_0|^2 = \gamma_f^2 / v_s v_0$ is in agreement with Eqs. (A6)–(A8). It follows from Eq. (A9) that the forward-scattered intensities $F_1 = |A_{f1}|^2$ and $F_2 = |A_{f2}|^2$ satisfy the equations

$$d_z F_1 = 2\mu_f P F_1, \tag{A11}$$

$$d_z F_2 = 2\mu_f P F_2, \tag{A12}$$

where $P = |A_0|^2$ is the pump intensity.

The geometry associated with the backward SBS of an isolated beam is shown in Fig. 75.36(b). Each backward-

scattering process is subject to matching conditions of the form

$$\omega_0 = \omega_b + \omega_s, \quad \mathbf{k}_0 = \mathbf{k}_b + \mathbf{k}_s, \qquad (A13)$$

where $(\omega_0, \mathbf{k}_0)$ and $(\omega_b, \mathbf{k}_b)$ satisfy the light-wave dispersion equation, and $(\omega_s, \mathbf{k}_s)$ satisfies the sound-wave dispersion equation. As in forward SBS, $\omega_{b2} = \omega_{b1} = \omega_b$ and $\omega_{s2} = \omega_{s1} = \omega_s$.

By adding to Ansatz (A2) the terms

$$A_{b1} \exp(i\mathbf{k}_{b1} \cdot \mathbf{x} - i\omega_b t)$$
$$+ A_{b2} \exp(i\mathbf{k}_{b2} \cdot \mathbf{x} - i\omega_b t) + c.c. \qquad (A14)$$

and to Ansatz (A3) the terms

$$N_1 \exp(i\mathbf{k}_{s1} \cdot \mathbf{x} - i\omega_s t)$$
$$+ N_2 \exp(i\mathbf{k}_{s2} \cdot \mathbf{x} - i\omega_s t) + c.c. \qquad (A15)$$

associated with backward SBS, one can show that each backward-scattering process is governed by equations of the form

$$-\partial_z A_b = i(\omega_e^2 / 2\omega_0 v_0) A_0 N^*, \qquad (A16)$$

$$(\partial_t + v_s) N^* = -i(\omega_s^2 / 2\omega_s) A_0^* A_b + v_s n^*. \qquad (A17)$$

As in forward SBS, $v_{s2} = v_{s1} = v_s$. It follows from Eqs. (A16) and (A17) that the transient evolution of backward SBS is governed by Eqs. (A6)–(A8), with f replaced by b and z replaced by $l-z$. Equations (A6) and (A7) apply to other parametric instabilities driven by an isolated pump wave provided that one type of daughter wave is strongly damped. In steady state, the backward-scattered intensities $B_1 = |A_{b1}|^2$ and $B_2 = |A_{b2}|^2$ satisfy the equations

$$-d_z B_1 = 2\mu_b P B_1, \qquad (A18)$$

$$-d_z B_2 = 2\mu_b P B_2, \qquad (A19)$$

where μ_b is given by Eq. (A10), with f replaced by b.

In the high-gain regime, the intensities of the scattered waves as they exit the plasma are comparable to the intensity of the pump wave as it enters the plasma, and one must account for the depletion of the pump wave within the plasma. In steady state, the pump intensity satisfies the equation

$$d_z P = -2\mu_f(F_1 + F_2) - 2\mu_b(B_1 + B_2). \qquad (A20)$$

By making the substitutions $F = F_1 + F_2$ and $B = B_1 + B_2$ in Eqs. (A11), (A12), (A18), (A19), and (A20), one can show that the simultaneous forward and backward SBS of an isolated beam is governed by the equations

$$d_z F = 2\mu_f P F, \qquad (A21)$$

$$-d_z B = 2\mu_b P B, \qquad (A22)$$

$$d_z P = -2(\mu_f F + \mu_b B) P. \qquad (A23)$$

Equations (A21)–(A23) are equivalent to Eqs. (43)–(45), the solution of which was described in the text. It is clear from the derivation of Eqs. (A21)–(A23) that one can interpret F as the intensity scattered forward over the entire range of angles for which propagation in the z direction is a reasonable approximation, and one can interpret B as the intensity scattered backward over the entire range of angles for which propagation in the $-z$ direction is a reasonable approximation. Equations (A21)–(A23) apply to other parametric instabilities driven by an isolated pump wave, provided that one type of daughter wave is strongly damped. For SBS, $\mu_b = \mu_f = \mu$,[7] and one can use the substitution $2\mu z \to z$ to rewrite Eqs. (A21)–(A23) in the form of Eqs. (46)–(48).

REFERENCES

1. W. L. Kruer, *The Physics of Laser Plasma Interactions*, Frontiers in Physics, Vol. 73, edited by D. Pines (Addison-Wesley, Redwood City, CA, 1988).

2. R. L. McCrory and J. M. Soures, in *Laser-Induced Plasmas and Applications*, edited by L. J. Radziemski and D. A. Cremers (Dekker, New York, 1989), p. 207.

3. J. D. Lindl, Phys. Plasmas **2**, 3933 (1995).

4. M. R. Amin *et al.*, Phys. Rev. Lett. **71**, 81 (1993).

5. M. R. Amin *et al.*, Phys. Fluids B **5**, 3748 (1993).

6. C. J. McKinstrie, R. Betti, R. E. Giacone, T. Kolber, and J. S. Li, Phys. Rev. E **50**, 2182 (1994).

7. R. E. Giacone, C. J. McKinstrie, and R. Betti, Phys. Plasmas **2**, 4596 (1995); **5**, 1218 (1998).

8. C. J. McKinstrie, J. S. Li, and A. V. Kanaev, Phys. Plasmas **4**, 4227 (1997).

9. A. A. Zozulya, V. P. Silin, and V. T. Tikhonchuk, Sov. Phys. JETP **65**, 443 (1987).

10. D. F. DuBois, B. Bezzerides, and H. A. Rose, Phys. Fluids B **4**, 241 (1992).

11. C. J. McKinstrie and M. V. Goldman, J. Opt. Soc. Am. B **9**, 1778 (1992).

12. Laboratory for Laser Energetics LLE Review **74**, 113, NTIS document No. DOE/SF/19460-241 (1998). Copies may be obtained from the National Technical Information Service, Springfield, VA 22161.

13. C. L. Tang, J. Appl. Phys. **37**, 2945 (1966).

14. R. L. Berger, E. A. Williams, and A. Simon, Phys. Fluids B **1**, 414 (1989).

15. W. L. Kruer *et al.*, Phys. Plasmas **3**, 382 (1996).

16. V. V. Eliseev *et al.*, Phys. Plasmas **3**, 2215 (1996).

17. C. J. McKinstrie, J. S. Li, R. E. Giacone, and H. X. Vu, Phys. Plasmas **3**, 2686 (1996).

18. C. J. McKinstrie, V. A. Smalyuk, R. E. Giacone, and H. X. Vu, Phys. Rev. E **55**, 2044 (1997).

19. C. J. McKinstrie, A. V. Kanaev, V. T. Tikhonchuk, R. E. Giacone, and H. X Vu, Phys. Plasmas **5**, 1142 (1998).

20. R. K. Kirkwood *et al.*, Phys. Rev. Lett. **76**, 2065 (1996).

21. A. K. Lal, K. A. Marsh, C. E. Clayton, C. Joshi, C. J. McKinstrie, J. S. Li, and T. W. Johnston, Phys. Rev. Lett. **78**, 670 (1997).

Landau Damping and Transit-Time Damping of Localized Plasma Waves in General Geometries

The collisionless damping of electrostatic plasma waves, first predicted by Landau[1] in 1946 and since rederived in many ways and confirmed experimentally, has become perhaps the most well known phenomenon in plasma physics. Landau damping plays a significant practical role in many plasma experiments and applications but has continued to be of great interest to theorists as well. Much of this interest stems from the counterintuitive nature of the result itself (that waves carrying free energy dissipate with no increase in entropy) coupled with the rather abstruse mathematical nature of Landau's original derivation. For these reasons there was even some controversy over the reality of the phenomenon,[2] until it was actually observed in experiments.

The usual derivation of Landau damping[3] begins by linearizing the Vlasov equation for an infinite homogeneous collisionless plasma. The linearized Vlasov equation is Fourier transformed in space and Laplace transformed in time, and the resulting equations in transform space are then solved algebraically to yield a relation between the perturbing field and the perturbed distribution function. Alternatively, this relation may be obtained by directly integrating the linearized Vlasov equation in configuration space using the method of characteristics,[4] also known as "integration over unperturbed orbits," and then performing the Fourier and Laplace transforms. Integration of this relation over particle velocities then leads to the dielectric response function and a dispersion relation for the plasma waves. Performing the integration over velocities entails the avoidance of a pole on the real axis by deforming the integration contour into the complex velocity plane. (Details can be found in most introductory plasma physics texts.) While this derivation is mathematically elegant, it is physically rather obscure, especially in regard to the introduction of complex velocities. For this reason, many "physical" derivations of Landau damping have been published, employing only real physical quantities throughout.[5,6] In these derivations, the energy transferred from the wave to each particle is calculated directly and then integrated over the particle distribution function to give the damping. In these physical derivations, however, the perturbed particle orbit must be determined and the

wave-particle energy transfer calculated to second order in the field amplitudes. (The reasons for this will be discussed below.) Calculation of the perturbed particle orbit in a time-varying field is rather complicated, even for a plane wave, involving as it does iterated time integrals of the equation of motion. Such complications are contrary to the motivation for a physical derivation of Landau damping, which is to provide a simple, physically intuitive explanation of the phenomenon. Furthermore, they ought to be unnecessary since the transform derivation requires only unperturbed orbits and first-order quantities. One of the results that will emerge below is a physical derivation of Landau damping based solely on unperturbed orbits.

Strictly speaking, the term "Landau damping" applies only to the damping of infinite plane waves in homogeneous plasmas. Localized electrostatic perturbations in inhomogeneous plasmas, however, are also damped by collisionless processes.[7] Particles transiting the region containing the wave exchange energy with it; for a thermal distribution of particles, this results in a net transfer of energy from the wave to the particles and a consequent damping of the wave. This process is usually referred to as "transit-time damping."[8,9] Since, in general, the Fourier transform method used by Landau is difficult to apply in inhomogeneous plasmas, transit-time damping calculations employ the physical approach described above: the energy transferred to each particle is calculated and then integrated over the particle distribution function. Again, however, this requires that the perturbed particle orbits be determined and the energy transfer be calculated to second order in the fields; for a localized field in an inhomogeneous plasma, this is much more complicated than for a plane wave. Since Landau damping can be calculated based solely on the unperturbed orbits, it is natural to inquire if transit-time damping could also be calculated without invoking the perturbed orbits. One of the main purposes of this article is to show how this can be done.

First, we give a physical derivation of transit-time damping in a plasma slab of finite width based on unperturbed orbits and investigate how the damping of a plasma wave confined to the

slab varies with slab width and mode number. We also show that the result reduces to the usual Landau-damping expression as the width becomes large. Next, we present a similar analysis for spherical geometry followed by a brief discussion of the cylindrical case, which is covered in more detail in a future article.[10] Finally, in an appendix, we show formally that in general geometries our approach gives results equivalent to those obtained by other methods that require the use of perturbed orbits and higher-order terms.

Transit-Time Damping in Slab Geometry

Our approach to transit-time damping may be outlined as follows: Consider a localized oscillating electrostatic field that may be regarded as stationary in time, i.e., its oscillation amplitude is unchanging. In practice, this may correspond to a situation of weak damping, where the damping rate is much smaller than the oscillation frequency (as is often the case for Landau damping), or to a situation where wave energy lost to damping is replenished by an external source, such as in the case of stimulated Raman or Brillouin scattering, where the electrostatic wave is driven by interaction with an electromagnetic pump wave. We assume that the particle distribution function f_0 depends solely on the particle energy E, and we further assume that collisional damping is negligible and take the plasma to be collisionless, so that $f_0(E)$ satisfies the Vlasov equation. Consider a six-dimensional phase-space volume element dV, which passes through the localization volume in time Δt and emerges as the volume element dV^*. Since the Vlasov equation conserves phase-space volume, we have $|dV^*| = |dV|$, though the shape of the volume element may change. Through interaction with the field, each particle in dV acquires an energy increment ΔE, which may be positive or negative. Since the situation is stationary and the Vlasov equation is invariant under time reversal, the time-reversed process must be occurring simultaneously. In the reversed process, the volume element dV^* enters the localization volume and emerges as dV, each particle in the volume *losing* the energy increment ΔE in time Δt. The net rate at which energy is transferred to the particles associated with dV is then

$$\Delta P = \left\langle \frac{\Delta E}{\Delta t} \Big[f_0(E)dV - f_0(E+\Delta E)dV^* \Big] \right\rangle$$

$$\cong -\frac{\left\langle (\Delta E)^2 \right\rangle}{\Delta t} \frac{\partial f_0}{\partial E} dV, \tag{1}$$

where the angle brackets indicate averaging over the field phase. Integration of this quantity over the phase space within

the localized volume then gives *twice* the collisionless power transfer to the electrons since the phase space is effectively included twice in the integration (both forward and backward in time).

To illustrate, we now calculate the average energy gain rate of electrons crossing a one-dimensional slab region containing a standing-wave electrostatic field. We will obtain a simple expression for the field damping rate as a function of the slab length (for fixed oscillation frequency and wavelength).

Consider a standing-wave electrostatic potential, ϕ, of real frequency ω:

$$\phi = -\frac{C}{k}\sin(kx)\cos(\omega t)$$

in the slab region with boundaries at $x = 0$ and $x = L$. Here C is a constant inside the slab and vanishes outside, and $kL = 2\pi j$ with j a positive integer so that the potential is continuous. The corresponding electrostatic field is

$$E(x,t) = C\cos(kx)\cos(\omega t).$$

We also assume that electrons with a constant number density n_0 and a velocity distribution $f_0(E)$ are streaming constantly and freely through this region from the left at $x = 0$ and from the right at $x = L$. The density and temperature are chosen such that $\omega_{\rm pe}^2 \gg 3k^2 v_T^2$, where $\omega_{\rm pe}^2$ is the usual plasma frequency and v_T the thermal velocity, so that weak Landau damping and quasi-steady-state conditions obtain. The frequency ω and wave number k then satisfy the Bohm-Gross dispersion relation $\omega^2 = \omega_{\rm pe}^2 + 3k^2 v_T^2 \approx \omega_{\rm pe}^2$. We can also treat the case of stronger damping, with $\omega_{\rm pe}^2 \sim 3k^2 v_T^2$, if we assume that the steady state of the field is maintained by an external source such as the stimulated Raman scattering instability.

To first order in the field amplitude C, the velocity increment obtained by an electron of initial velocity v crossing the slab is simply

$$\Delta v = -\int_0^T \frac{eC}{m}\cos(kvt)\cos(\omega t + \phi)dt,$$

where we have used the unperturbed orbit $x = vt$. Here ϕ is the phase of the field at the time of entrance of the particle, and $T = L/v$. To this order, the energy change ΔE is given by

$\Delta E = mv\Delta v$. It is a simple matter to carry out the integral and then average $(\Delta E)^2$ over the phase. Note that $kvT = kL = 2\pi j$ and hence $\exp(\pm kvT) = 1$. The result is

$$\left\langle(\Delta E)^2\right\rangle = \frac{(evC)^2}{2}\sin^2\left(\frac{\omega T}{2}\right)\left[\frac{1}{\omega + kv} + \frac{1}{\omega - kv}\right]^2,$$

and Eq. (1) becomes

$$\Delta P = -\frac{(evC)^2}{2T}\sin^2\left(\frac{\omega T}{2}\right)$$
$$\times \left[\frac{1}{\omega + kv} + \frac{1}{\omega - kv}\right]^2 n_0\frac{df_0(v)}{dE}dv.$$

The net power transferred is obtained by integrating this expression over the phase space within the slab volume, noting that $T = L/|v|$. The result is

$$P = -\frac{\omega_{pe}^2 C^2}{16\pi}\int_{-\infty}^{\infty}\sin^2\left(\frac{\omega L}{2|v|}\right)$$
$$\times\left[\frac{1}{\omega + kv} + \frac{1}{\omega - kv}\right]^2 v|v|\frac{df_0(v)}{dv}dv, \qquad (2)$$

where we have divided by 2 to compensate for the double-counting of phase space, as noted earlier. Note also that although the familiar resonant denominators appear in the integrand, they do not represent poles because of the sine function, so the difficulties in dealing with poles in the velocity integration that arise in Landau's calculation do not appear here.

The energy damping rate follows by dividing this result by the total plasma-wave energy within the slab volume. This energy is

$$W = \int_0^L\left\langle\frac{E^2(x,t)}{4\pi}\right\rangle dx = \frac{C^2 L}{16\pi}, \qquad (3)$$

where the angle brackets denote averaging over time; hence, the field *amplitude* damping rate is *half* of (2) divided by (3):

$$\gamma = -\omega_{pe}^2\int_0^{\infty}\sin^2\left(\frac{\omega L}{2v}\right)$$
$$\times\left[\frac{1}{\omega + kv} + \frac{1}{\omega - kv}\right]^2\frac{v^2}{L}\frac{df_0(v)}{dv}dv. \qquad (4)$$

It is easy to show that this reduces to the Landau value in the infinite slab-length limit. Without loss of generality, we may take ω and k positive. If $v \neq \omega/k$, the integrand is finite and thus gives no contribution to γ as $L \to \infty$ (keeping k fixed, which means increasing L in wavelength steps, or j in integral steps). For $v \to \omega/k$, the integrand varies directly as L and becomes infinite. Clearly, the integrand is proportional to $\delta(v - \omega/k)$ in this limit. Replacing nonresonant values of v by ω/k and defining the integration variable $q \equiv \pi(L/\lambda)(\omega/kv - 1)$, where $\lambda = 2\pi/k$ is the wavelength, yields

$$\gamma = -\omega_{pe}^2\left(\frac{\omega}{k}\right)^2\frac{df_0}{dv}\bigg|_{\frac{\omega}{k}}\frac{1}{2\omega}\int_{-\pi L/\lambda}^{\infty}\frac{\sin^2 q}{q^2}dq.$$

In the limit of an infinite homogeneous plasma $L/\lambda \to \infty$, we obtain

$$\gamma = -\frac{\pi\omega_{pe}^2\omega}{2k^2}\frac{df_0}{dv}\bigg|_{\frac{\omega}{k}}, \qquad (5)$$

which is the familiar Landau damping rate for electrostatic waves in a homogeneous plasma.

Colunga *et al.*[11] have also obtained an expression for transit-time damping in a slab and noted that it can be represented as the Landau damping of the Fourier components of the localized electric field, which also gives (5) as the size of the slab increases. Their derivation, however, requires calculation of the wave-particle energy transfer to second order (i.e., use of perturbed orbits.)

We next investigate the damping rate's dependence on the slab size and plasma parameters. Assuming a Maxwellian distribution for $f_0(E)$ and changing the integration variable to $z \equiv \omega/kv$, Eq. (4) becomes

$$\gamma = \frac{4F^3\omega_{pe}^2\lambda}{(2\pi)^{3/2}L\omega}\int_0^{\infty}\frac{\sin^2\left(\frac{\pi L}{\lambda}z\right)\exp\left(-F^2/2z^2\right)}{\left(1 - z^2\right)^2 z^3}dz. \quad (6)$$

Here, $F = \omega/kv_T$, with v_T the electron thermal velocity. For values of F well above unity, we have $\omega \approx \omega_{pe}$ and $F \approx (k\lambda_D)^{-1}$. The integral above is readily evaluated, for fixed F, and its variation with j is shown in Figs. 75.37(a) and 75.37(b) for $F = 6$ and $F = 4$, respectively. What is actually plotted is the ratio of γ to γ_L, where γ_L is the infinite slab limit $(L/\lambda \to \infty)$ of Eq. (6),
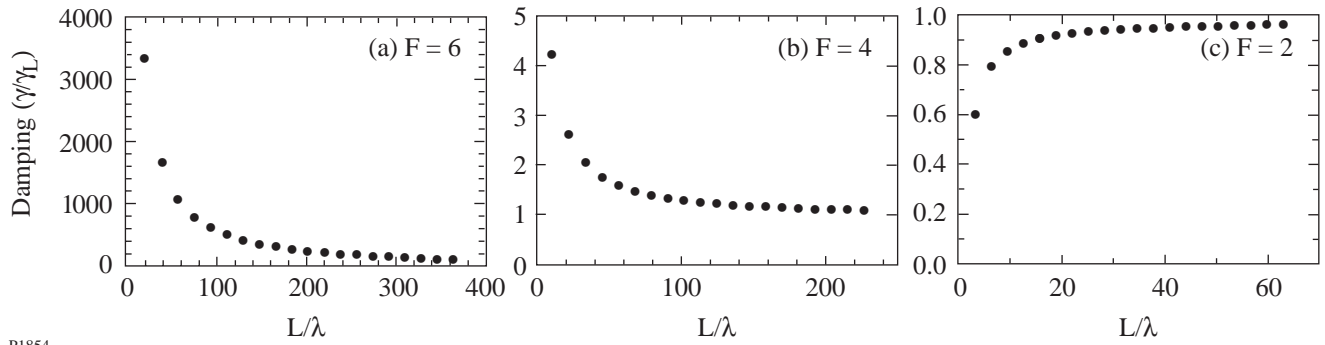
P1854

Figure 75.37

Damping rates for a standing plasma wave in a slab of length L, normalized to the Landau damping rate for an infinite homogeneous plasma γ_L. In (a)–(c) results are presented for three values of the parameter $F = \omega/kv_t$, with smaller values of F corresponding to stronger Landau damping.

$$\gamma_{\mathrm{L}} = \left(\frac{\pi}{8}\right)^{1/2} \frac{F^3\omega_{\mathrm{pe}}^2}{\omega} \exp\left(\frac{-F^2}{2}\right), \qquad (7)$$

the usual Landau damping value. The Landau result arises from the resonant part of the integral; the nonresonant part gives rise to the finite geometry transit-time component of the damping.

Note the monotonic decrease in damping to the usual Landau value as L/λ increases. The value of the ratio at $L/\lambda = 1$ increases as F increases and can be quite large; hence, the transit-time damping can be much larger than the Landau rate for finite slabs. Note, however, that γ_{L} decreases exponentially with increasing F.

The nonresonant contribution does not always lead to augmentation of the Landau damping rate. As F decreases, the variation with L/λ reverses and the damping *increases* monotonically to the Landau value, as shown in Fig. 75.37(c) for $F = 2$. The general trend seems to be that the finite geometry increases the damping when the infinite geometry (Landau) limit of the damping is small (large F) and reduces damping when the infinite geometry limit is large. An analogous trend appears in the spherical and cylindrical cases, as discussed below, and a qualitative interpretation is presented in the **Conclusions** section.

Transit-Time Damping in Spherical Geometry

As an example of a finite three-dimensional calculation, we now examine the damping of electrostatic modes trapped in a sphere of radius R with a homogeneous internal density n_0. To illustrate the method as simply as possible, we consider only

modes with no angular dependence (angular mode numbers $l = m = 0$); more complicated potentials and density profiles will give rise to more complicated forms of the function G, defined in Eq. (10) below, but can be handled by the same basic approach.

The potential inside the sphere is taken to be

$$\phi(r,t) = Aj_0(kr)\cos(\omega t + \alpha), \qquad (8)$$

corresponding to a standing spherical wave, where $j_0(x) = \sin x/x$ denotes the spherical Bessel function of order zero, and α is an arbitrary constant representing the phase of the wave, to be averaged over below. The boundary condition is $j_0(kR) = 0$, so k may be any of a discrete set of wave numbers determined by the roots of the Bessel function.

Let $t = 0$ be the time when a particle is closest to the center of the sphere. We obtain its change in energy by integrating over the unperturbed orbit:

$$\Delta E = -e\int_{-t_0}^{t_0} \mathbf{v}\cdot\nabla\phi(\mathbf{r},t)\,dt.$$

Here $2t_0 = \sqrt{R^2 - b^2}/v$ is the time required to cross the sphere, where b is the distance of closest approach to the center of the sphere. The total derivative of the potential is

$$\frac{d}{dt}\phi[\mathbf{r}(t),t] = \mathbf{v}\cdot\nabla\phi[\mathbf{r}(t),t] + \frac{\partial}{\partial t}\phi[\mathbf{r}(t),t],$$

so the above integral can be written

$$\Delta E = -e\int_{-t_0}^{t_0} \left\{ \frac{d}{dt}\phi[\mathbf{r}(t),t] - \frac{\partial}{\partial t}\phi[\mathbf{r}(t),t] \right\} dt.$$

The potential seen by the particle is the same before and after passing through the sphere, so

$$\int_{-t_0}^{t_0} \frac{d}{dt}\phi[\mathbf{r}(t),t]\,dt = 0$$

and

$$\Delta E = e\int_{-t_0}^{t_0} \frac{\partial}{\partial t}\phi[\mathbf{r}(t),t]\,dt.$$

Substituting the form of the potential, changing the integration variable to $s = kvt$, and averaging over the phase α gives

$$\left\langle \Delta E^2 \right\rangle = \frac{\omega^2 e^2 A^2}{2k^2 v^2} G^2\left(kR, kb, \frac{\omega}{kv}\right), \tag{9}$$

where

$$G\left(kR, kb, \frac{\omega}{kv}\right) \equiv \int_{-k\sqrt{R^2-b^2}}^{k\sqrt{R^2-b^2}} \times j_0\left(\sqrt{k^2 b^2 + s^2}\right)\cos\left(\frac{\omega s}{kv}\right) ds, \tag{10}$$

a function that must be evaluated numerically.

Next we must integrate Eq. (1), the power loss in an element of phase-space volume, over the six-dimensional phase space inside the sphere. The total power being transferred to particles in the sphere is then

$$P = \int_0^\pi d\theta_r \sin\theta_r \int_0^{2\pi} d\phi_r$$

$$\times \left\{ \int_0^R dr\, r^2 \int_0^\infty dv\, v^2 \int_0^\pi d\theta_v \int_0^{2\pi} d\phi_v \left[-\frac{1}{2}\frac{\left\langle \Delta E^2 \right\rangle}{\Delta t}\frac{\partial f_0}{\partial E} \right] \right\}, \tag{11}$$

where the factor $1/2$ in the integrand compensates for the double-counting of phase space, as noted earlier in the **Transit-Time Damping** section. Because of the spherical symmetry, the term in braces must be independent of θ_r and ϕ_r, so for convenience we can evaluate it at $\theta_r = \phi_r = 0$ and obtain

$$P = 4\pi n_0 \left\{ \int_0^R dr\, r^2 \int_0^\infty dv\, v^2 \int_0^\pi d\theta_v \int_0^{2\pi} d\phi_v \right.$$

$$\left. \times \left[-\frac{1}{2}\frac{\left\langle \Delta E^2 \right\rangle}{\Delta t}\frac{\partial f_0}{\partial E} \right] \right\} \Bigg|_{\theta_r = \phi_r = 0}. \tag{12}$$

For $\theta_r = \phi_r = 0$ we can use the relation $b/r = \sin\theta_v$ to convert the integral over θ_v to an integral over b:

$$\int_0^\pi d\theta_v \sin\theta_v \to 2\int_0^{\pi/2} d\theta_v \sin\theta_v \to 2\int_0^r db\,\frac{b/r}{\sqrt{r^2-b^2}}. \tag{13}$$

From Eqs. (9) and (10) we see that $\left\langle \Delta E^2 \right\rangle$ is independent of r for fixed b, so using Eq. (13) and $\Delta t = 2\sqrt{R^2-b^2}\big/v$, we can perform the r and ϕ_v integrals in Eq. (12):

$$P = \frac{2\pi^2 \omega^2 e^2 A^2 n_0}{k^2}$$

$$\times \int_0^\infty dv\, v\left[-\frac{\partial f_0(E)}{\partial E} \right]\int_0^R db\, b\, G^2\left(kR, kb, \frac{\omega}{kv}\right). \tag{14}$$

The amplitude-damping rate is now given by $\gamma/\omega = P/2\omega W$, where W is the wave energy contained in the sphere:

$$W = \int_V \left\langle \frac{E^2}{4\pi} \right\rangle_t dV.$$

From Eq. (8) we have

$$\left\langle E^2 \right\rangle_t = \frac{1}{2}k^2 A^2 j_0'^2(kr),$$

so

$$W = \int_V \frac{E_{max}^2}{16\pi} dV = \frac{1}{2}k^2 A^2 \int_0^R r^2 j_0'^2(kr)\,dr = \frac{1}{4}RA^2. \tag{15}$$

As $R \to \infty$ with k fixed, the electrostatic wave will locally come to look like a plane wave with wave number k throughout most of the volume of the sphere, so we might expect that in this limit Eq. (14) should give the usual Landau damping rate for such a wave. In Appendix A we show that this is indeed the case.

As in the slab geometry, we can characterize the wave parameters by the quantity $F = \omega/kv_T$ and calculate the damping rates obtained from Eqs. (14) and (15) as the radius of the sphere changes. Figures 75.38(a)–75.38(c) show the results for $F = 6, 4,$ and 2, respectively. As in the slab case, we find that the results lie above the Landau limit when the damping is weak (F large), and below when the damping is strong (F small).

Cylindrical Geometry

The case of cylindrical geometry is somewhat more complicated than the slab and spherical geometries because there are two independent components of the wave vector: axial and radial. The cylindrical case is analyzed in detail in a forthcoming article,[10] where the results are applied to the problem of stimulated Raman scattering in a self-focused light filament in a laser-produced plasma. Here we merely note that the damping rate can be shown both analytically and numerically to approach the Landau value as the radius becomes large, and we show some results for the case of a purely radial wave vector for the same values of $F = \omega/kv_T$ as in the slab and spherical cases [Figs. 75.39(a)–75.39(c)]. Once again, we find that the finite radius results lie below the Landau value for F small and above for F large.
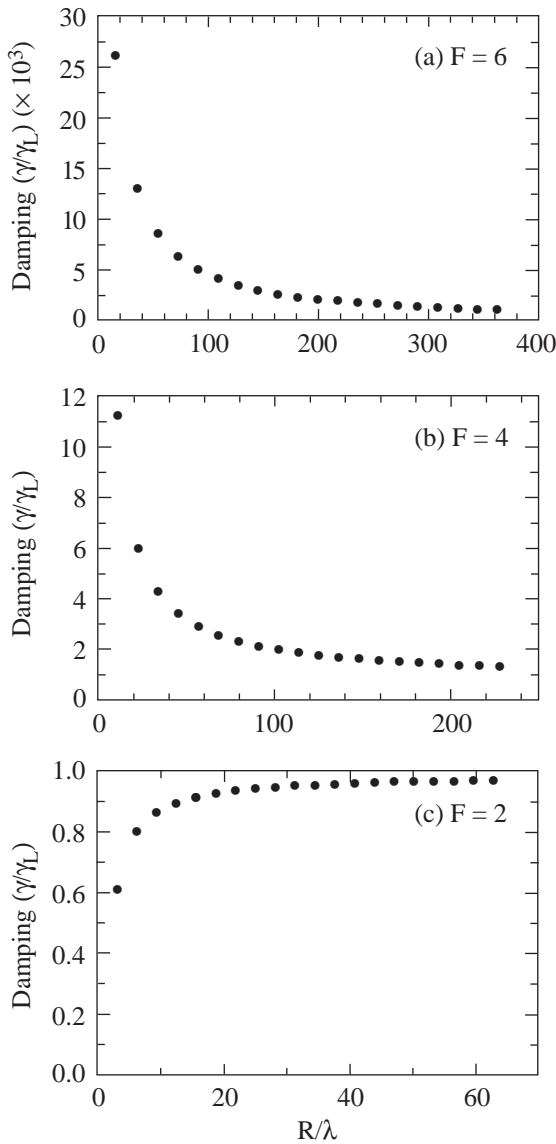
P1855

Figure 75.38
Same as Fig. 75.37, but for a sphere of radius R.
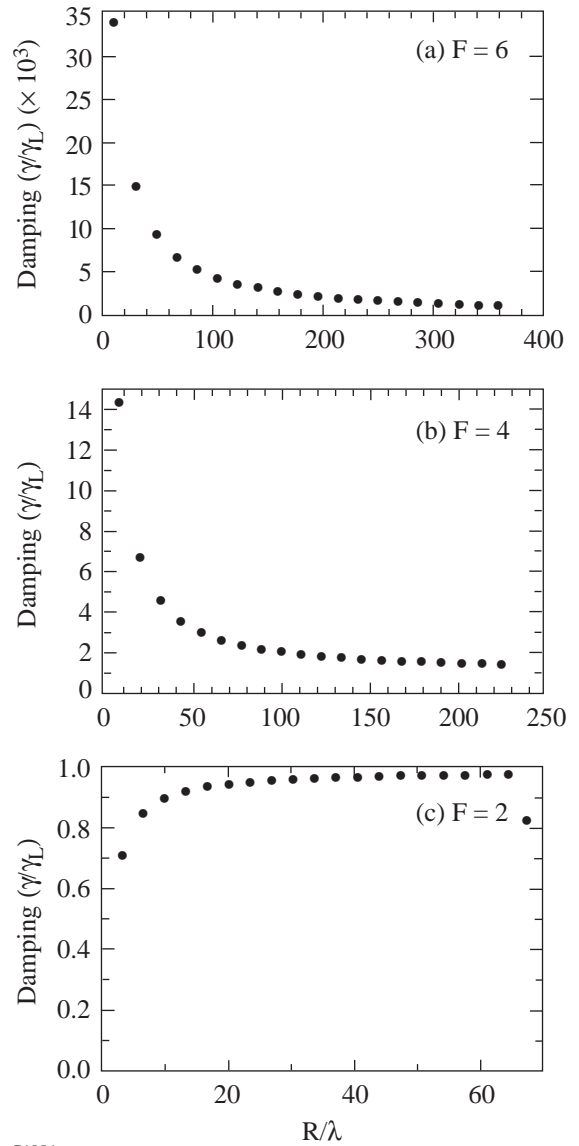
P1856

Figure 75.39
Same as Fig. 75.37, but for a cylinder of radius R. Here $F = \omega/kv_t$, where k is the radial wave number of the oscillation and the axial wave number is zero.

Conclusions

In summary, we have demonstrated a new, simplified approach to calculating transit-time damping. Our approach uses the time-reversal invariance of the Vlasov equation to avoid the necessity of calculating the wave–particle energy exchange to second order in the wave fields. We have illustrated the method by analyzing the damping of electrostatic oscillations in slab, cylindrical, and spherical geometries, both analytically and numerically. In general, our results seem to show that finite geometry effects tend to augment Landau damping when it would be small in an unbounded geometry, and reduce it when it would be large.

These results suggest a qualitative physical interpretation based on regarding the particles interacting with the electrostatic wave as falling into two classes: resonant and nonresonant. Resonant particles are those whose (unperturbed) motion keeps them in a constant phase relationship with the wave; depending on this phase they continuously either gain or lose energy from their interaction with the wave. As is well known, these are the particles responsible for Landau damping in infinite homogeneous plasmas. Nonresonant particles, on the other hand, see a varying wave phase as they propagate, and alternately gain and lose energy as this phase changes. In the case of an infinite geometry, these gains and losses cancel out over the infinite "transit time," and the nonresonant particles make no contribution to Landau damping. In the case of a finite system, the "resonant" particles can be regarded as those that do not get significantly out of phase with the wave while passing through the system; since their transit time decreases as the system becomes smaller, the number of particles that can be regarded as resonant increases as the confinement volume shrinks. It can be shown,[6] however, that the contribution of these nearly resonant particles to the damping goes as the fourth power of the time, so that the net contribution to the damping of the near-resonant particles diminishes as the confinement volume and the transit time become smaller. On the other hand, for a finite volume the energy gains and losses of the nonresonant particles no longer average to zero, and as the volume becomes smaller, the contribution of these nonresonant particles to the damping becomes larger. Thus, the damping in a finite system contains a smaller resonant component and a larger nonresonant component than in the corresponding infinite system. When the Landau damping is large in the infinite system (F small), the decrease in the resonant damping dominates the increase in the nonresonant damping, so that the damping in the finite system decreases from the Landau rate as the system size diminishes. When Landau damping is small (F large), the increase in nonresonant damping dominates, and the transit-

time damping of the finite system is larger than the Landau damping of the corresponding infinite system. This picture is in qualitative agreement with the results we have obtained above for the slab, cylinder, and spherical geometries.

It should be noted that the essential advantage of the time-reversal invariance approach—the need to calculate the wave–particle energy transfer ΔE to only first order—is not dependent on the particular geometry of the system under consideration. For purposes of illustration, we have chosen simple geometries; in more complex geometries and inhomogeneous plasmas the phase-space integrals such as Eq. (13) will have to be carried out numerically, but the simplification in the calculation of ΔE will then be even more valuable. In Appendix B we show that the time-reversal invariance approach can be applied in quite general geometries, and verify that it gives results identical to the perturbed orbit approach.

Appendix A: Large-Radius Limit of Collisionless Damping in Spherical Geometry

To evaluate the damping rate for large radii, we first investigate the nature of the function

$$S(kR, z) \equiv \frac{k}{R} \int_0^R db\, b\, G^2(kR, kb, z), \qquad (A1)$$

from which Eqs. (14) and (15) contain the R dependence of the damping rate (here $z \equiv \omega/kv$ and the factor k is included for convenience to make the function dimensionless). From Eq. (10) we have, using $j_0(x) \equiv \sin(x)/x$ and defining $t = s/kR$ and $x = b/R$,

$$G(kR, x, z) = 2\int_0^{\sqrt{1-x^2}} \frac{\sin kR\sqrt{t^2+x^2}}{\sqrt{t^2+x^2}} \cos(zkRt)dt$$

$$= \mathrm{Im}\left\{ \int_0^{\sqrt{1-x^2}} \frac{1}{\sqrt{t^2+x^2}} \right.$$

$$\left. \left[e^{ikR\left(\sqrt{t^2+x^2}-zt\right)} + e^{ikR\left(\sqrt{t^2+x^2}+zt\right)} \right] dt \right\}$$

$$= \mathrm{Im}\left\{ \int_0^{\sqrt{1-x^2}} \frac{1}{\sqrt{t^2+x^2}} \left[e^{ikR\psi_-(t)} + e^{ikR\psi_+(t)} \right] dt \right\}, \qquad (A2)$$

where

$$\psi_{\pm}(t) \equiv \sqrt{t^2 + x^2} \pm zt.$$

We next use the method of stationary phase to determine the dominant behavior of $G(kR,x,z)$ as $kR \to \infty$. Using the Riemann–Lebesgue lemma, it is readily shown that the integral in Eq. (A2) vanishes as $1/kR$ as $kR \to \infty$ unless the functions

$$\psi'_{\pm}(t) = \frac{d}{dt}\left[\sqrt{t^2 + x^2} \pm zt\right] = \frac{t}{\sqrt{t^2 + x^2}} \pm z$$

vanish at some point in the t integration interval $\left[0, \sqrt{1-x^2}\right]$, in which case the integral will vanish more slowly than $1/kR$ as $kR \to \infty$. Clearly $\psi'_+(t)$ cannot vanish in this interval, so the dominant behavior of G is given by

$$G(kR,x,z) \sim \mathrm{Im}\left\{\int_0^{\sqrt{1-x^2}} \frac{1}{\sqrt{t^2+x^2}} e^{ikR\psi_-(t)} dt\right\}$$

$$\text{for } x^2 + z^2 \le 1. \tag{A3}$$

The inequality in Eq. (A3) is the necessary and sufficient condition that $\psi'_-(t)$ vanish in $\left[0, \sqrt{1-x^2}\right]$. When this inequality is not satisfied, G vanishes more rapidly as $kR \to \infty$ and hence may be neglected; thus, the dominant behavior of Eq. (A1) as $kR \to \infty$ is given by

$$S(kR,z) \sim kR\int_0^{\sqrt{1-z^2}} dx\, x\, G^2(kR,x,z). \tag{A4}$$

The dominant contribution to the integral in Eq. (A3) comes from the point in $\left[0, \sqrt{1-x^2}\right]$ where $\psi'_-(t)$ vanishes, so we may extend the upper limit of the range of integration without changing the leading behavior of G:

$$G(kR,x,z) \sim \mathrm{Im}\left\{\int_0^1 \frac{1}{\sqrt{t^2+x^2}} e^{ikR\left(\sqrt{t^2+x^2} - zt\right)} dt\right\}$$

$$\text{for } x^2 + z^2 \le 1,$$

$$\sim 2\int_0^1 \frac{\sin\left(kR\sqrt{t^2+x^2}\right)}{\sqrt{t^2+x^2}} \cos(zkRt)\, dt.$$

Using $t = s/kR$ and $x = b/R$, this can be written

$$G(kR,kb,z) \sim 2\int_0^{kR} \frac{\sin\sqrt{k^2b^2+s^2}}{\sqrt{k^2b^2+s^2}} \cos(zs)\, ds$$

$$\sim 2\int_0^{\infty} \frac{\sin\sqrt{k^2b^2+s^2}}{\sqrt{k^2b^2+s^2}} \cos(zs)\, ds$$

$$= \pi J_0\left(kb\sqrt{1-z^2}\right) \text{ for } \left(\frac{b}{R}\right)^2 + z^2 \le 1.$$

Substituting in Eq. (A4), we obtain

$$S(kR,z) \sim \frac{1}{kR}\int_0^{kR\sqrt{1-z^2}} d(kb)(kb)\, G^2(kR,kb,z)$$

$$\sim \frac{\pi^2}{kR}\int_0^{kR\sqrt{1-z^2}} d(kb)(kb) J_0^2\left(kb\sqrt{1-z^2}\right)$$

for $z \le 1$. Using

$$\int x J_0^2(\alpha x)\, dx = \frac{x^2}{2}\left[J_0^2(\alpha x) + J_1^2(\alpha x)\right],$$

this becomes

$$S(kR,z) \sim \frac{\pi^2 kR}{2}\left(1-z^2\right)$$

$$\left\{J_0^2\left[kR\left(1-z^2\right)\right] + J_1^2\left[kR\left(1-z^2\right)\right]\right\}$$

$$\sim \pi \text{ as } kR \to \infty \text{ for } z < 1,$$

where we have used the formula

$$\lim_{x\to\infty} x\left[J_0^2(x) + J_1^2(x)\right] = \frac{2}{\pi}.$$

For $z > 1$, since the condition $x^2 + z^2 \le 1$ cannot be satisfied, $S(kR,z)$ must vanish as $kR \to \infty$. Defining

$$T(z) \equiv \lim_{kR\to\infty} S(kR,z) = \begin{cases} \pi, & z < 1 \\ 0, & z > 1 \end{cases},$$

we see that $T(z)$ is a step function in z.

Thus, using Eqs. (14) and (15), the damping rate for large kR becomes

$$\lim_{kR\to\infty} \frac{\gamma}{\omega} = \lim_{kR\to\infty} \frac{P}{2\omega W}$$

$$= \frac{4\pi^2\omega e^2}{k^3} n_0 \int_0^\infty dv v \left[-\frac{\partial f_0}{\partial E} \right] T\left(\frac{\omega}{kv}\right)$$

$$= \frac{4\pi^2\omega e^2}{k^3} n_0 \pi \int_{\omega/k}^\infty dv v \left[-\frac{\partial f_0}{\partial E} \right]. \tag{A5}$$

Note from Eqs. (12) that f_0 here is the normalized three-dimensional distribution function, assumed isotropic:

$$4\pi \int_0^\infty v^2 f_0(v) dv = 1.$$

Using

$$\frac{\partial f_0}{\partial E} = \frac{1}{mv} \frac{\partial f_0}{\partial v},$$

the integral in Eq. (A5) is readily evaluated to give

$$\lim_{kR\to\infty} \frac{\gamma}{\omega} = \frac{4\pi^3\omega e^2}{k^3} n_0 f_0\left(\frac{\omega}{k}\right). \tag{A6}$$

This result can be expressed in a more familiar form in terms of the one-dimensional velocity distribution g, defined by

$$g(u) \equiv 2\pi \int_0^\infty dv v f_0\left(\sqrt{u^2 + v^2}\right)$$

$$= 2\pi \int_u^\infty dv v f_0(v). \tag{A7}$$

Differentiating this expression gives

$$\frac{dg}{du} = -2\pi u f_0(u), \text{ or } f_0(u) = -\frac{1}{2\pi u} \frac{dg}{du}.$$

In terms of the one-dimensional distribution function, Eq. (A6) becomes

$$\lim_{kR\to\infty} \frac{\gamma}{\omega} = -\frac{2\pi^2 e^2 n_0}{k^2 m} \frac{dg(u)}{du}\bigg|_{u=\frac{\omega}{k}}$$

$$= -\frac{\pi\omega_p^2}{2k^2} \frac{dg(u)}{du}\bigg|_{u=\frac{\omega}{k}},$$

which is just the Landau damping rate for plane waves of frequency ω and wave number k. This is to be expected since, as the radius of the sphere increases, an increasingly large fraction of the volume of the sphere contains waves that are locally planar, so that particles gain energy from them at the same rate as from a plane wave.

Appendix B: Equivalence of Perturbed Orbit and Time-Reversal Invariance Approaches to Transit-Time Damping

Transit-time damping of a confined electrostatic wave in a plasma arises from the transfer of energy from the wave to particles passing through the confinement region. In many cases of interest it may be assumed for purposes of calculating the damping that the wave properties (amplitude, frequency, etc.) are stationary in time. This means that background plasma properties such as the size and density of the confinement region are either constant or their variation is small during the wave period and the particle transit time. It also means that the wave energy lost to the damping is either replaced by another process, such as stimulated scattering, or again is small during the wave period and particle transit time.

Previous calculations of transit-time damping have taken a straightforward approach: the energy gained or lost by a particle transiting the confinement region is calculated, averaged over the phase of the wave, and integrated over the flux of particles weighted by the velocity distribution function. This approach can be represented in general by Fig. 75.40(a), and the power transferred from the wave to particles can be written

$$P = \int_0^\infty dv_x \, v_x \int d\mathbf{s} \, f_0(E) \left\langle \Delta E(E, 0, \mathbf{s}, \phi) \right\rangle_\phi$$

$$- \int_{-\infty}^0 dv_x \, v_x \int d\mathbf{s} \, f_0(E) \left\langle \Delta E(E, l, \mathbf{s}, \phi) \right\rangle_\phi. \tag{B1}$$

Here the angle brackets denote averaging over the phase ϕ of the wave, and $\mathbf{s}$ represents the coordinates and velocities perpendicular to the arbitrarily chosen x axis:
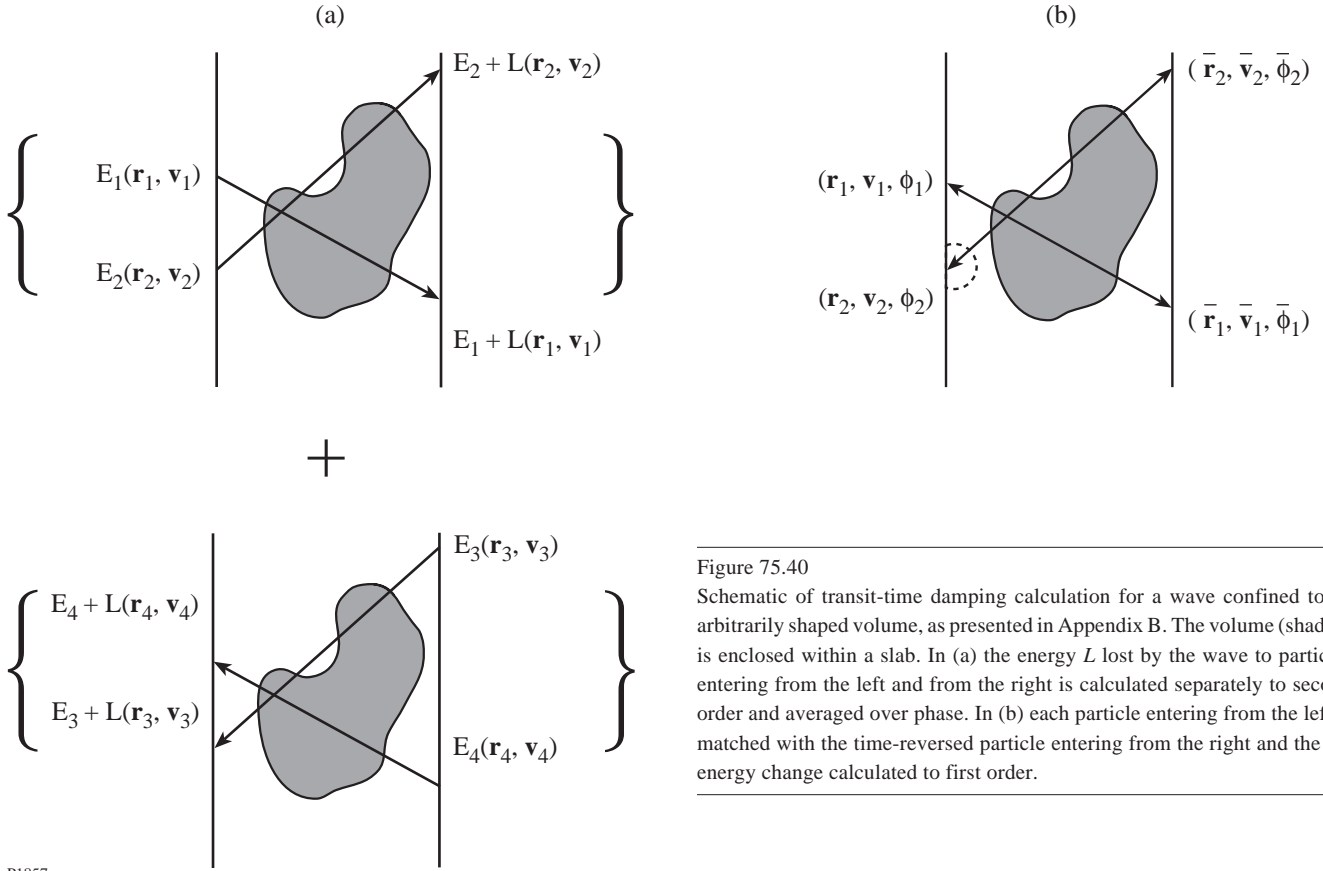
$$d\mathbf{s} = dy dz dv_y dv_z.$$

(a)

(b)

Figure 75.40
Schematic of transit-time damping calculation for a wave confined to an arbitrarily shaped volume, as presented in Appendix B. The volume (shaded) is enclosed within a slab. In (a) the energy L lost by the wave to particles entering from the left and from the right is calculated separately to second order and averaged over phase. In (b) each particle entering from the left is matched with the time-reversed particle entering from the right and the net energy change calculated to first order.

P1857

We include in our analysis all particles passing through a slab extending from $x = 0$ to $x = l$ and containing the confinement volume V. (Of course, only those particles following trajectories passing through V actually contribute to the damping, but describing only these trajectories is difficult for a volume of arbitrary shape. Including all trajectories passing through the slab greatly simplifies the representation of the particle flux in the general case and does not change the result since the additional trajectories do not contribute to the damping.) The functions $\Delta E\,(E,0,\mathbf{s},\phi)$ and $\Delta E\,(E,l,\mathbf{s},\phi)$ give the energy change for particles entering the slab at $x = 0$ and $x = l$, respectively, with energy E, phase ϕ, and other parameters $\mathbf{s}$. The distribution function f_0 is assumed uniform and isotropic and depends only on the energy $E = m\left(v_x^2 + v_y^2 + v_z^2\right)/2$.

The next step is to calculate the phase-averaged energy change:

$$L(E,0,\mathbf{s}) = \left\langle \Delta E\big(E,0,\mathbf{s},\phi\big)\right\rangle_\phi \text{ for } x = 0, \ v_x > 0;$$

$$L(E,l,\mathbf{s}) = \left\langle \Delta E\big(E,l,\mathbf{s},\phi\big)\right\rangle_\phi \text{ for } x = l, \ v_x < 0.$$

The energy ΔE gained or lost by a specific particle is first order in the field amplitude, but the gains and losses cancel to first order after phase averaging, so that the loss functions L are second order in the field. Evaluation of the loss functions thus requires that the energy changes ΔE also be calculated to second order, which in turn means that the perturbed trajectories must be determined and integrated over. This can lead to complicated calculations in general. Details of the calculation of the loss functions and the resulting damping rates are given for some simple cases in Robinson.[9]

Our purpose here is to show that the integrations in Eq. (B1) can be rearranged so that ΔE need only be calculated to first order, which can be accomplished by integration over the unperturbed orbits.

First we take the phase average outside the integrations and write it explicitly as an integral over ϕ:

$$P = \frac{1}{2\pi}\int_0^{2\pi} d\phi \int_0^\infty dv_x\, v_x \int d\mathbf{s}\, f_0(E)\,\Delta E\big(E,0,\mathbf{s},\phi\big)$$
$$- \frac{1}{2\pi}\int_0^{2\pi} d\bar{\phi}\int_{-\infty}^0 d\bar{v}_x\, \bar{v}_x \int d\bar{\mathbf{s}}\, f_0\big(\bar{E}\big)\,\Delta\bar{E}\big(\bar{E},l,\bar{\mathbf{s}},\bar{\phi}\big), \quad (B2)$$

where we have also denoted the integration parameters for particles entering the slab from the right at $x = l$ by an overbar (this amounts only to a change of dummy variable at this point and has no physical significance). We could, however, just as well calculate the second integral in Eq. (B2) by integrating over the parameters with which these particles leave the slab at $x = 0$. Since we are dealing with a collisionless plasma, we can invoke Liouville's theorem to say that an element of phase-space volume is invariant on passing through the slab:

$$dx\,dy\,dz\,dv_x\,dv_y\,dv_z = d\overline{x}\,d\overline{y}\,d\overline{z}\,d\overline{v}_x\,d\overline{v}_y\,d\overline{v}_z.$$ (B3)

Using $d\phi = \omega\,dt$, $d\overline{\phi} = \omega\,d\overline{t}$, $dx = v_x dt$, and $d\overline{x} = \overline{v}_x d\overline{t}$, where ω is the wave frequency, Eq. (B3) becomes

$$v_x\,dy\,dz\,dv_x\,dv_y\,dv_z\,d\phi = \overline{v}_x\,d\overline{y}\,d\overline{z}\,d\overline{v}_x\,d\overline{v}_y\,d\overline{v}_z\,d\overline{\phi}$$

or

$$v_x\,dv_x\,d\mathbf{s}\,d\phi = \overline{v}_x\,d\overline{v}_x\,d\overline{\mathbf{s}}\,d\overline{\phi}.$$ (B4)

Thus, the transformation from the integration parameters at $x = l$ to those at $x = 0$ has unit Jacobian, and we can write Eq. (B2) as

$$P = \frac{1}{2\pi}\int_0^{2\pi} d\phi \int_0^\infty dv_x\ v_x \int d\mathbf{s}\ f_0(E)\Delta E(E,0,\mathbf{s},\phi)$$
$$-\frac{1}{2\pi}\int_0^{2\pi} d\phi \int_{-\infty}^0 dv_x\ v_x \int d\mathbf{s}\ f_0(\overline{E})\Delta\overline{E}(\overline{E},l,\overline{\mathbf{s}},\overline{\phi}),$$ (B5)

where $\overline{E}$ is now a function of the $x = 0$ parameters:

$$\overline{E} = \frac{1}{2}m\left(v_x^2 + v_y^2 + v_z^2\right) + \Delta E(E,0,\mathbf{s},\phi)$$
$$= E + \Delta E(E,0,\mathbf{s},\phi).$$ (B6)

Also, from the definitions of ΔE and $\Delta\overline{E}$, we have

$$\Delta\overline{E}(\overline{E},l,\overline{\mathbf{s}},\overline{\phi}) = E - \overline{E} = -\Delta E(E,0,\mathbf{s},\phi).$$ (B7)

Substituting Eqs. (B6) and (B7) in Eq. (B5), we get

$$P = \frac{1}{2\pi}\int_0^{2\pi} d\phi \int_0^\infty dv_x\ v_x \int d\mathbf{s}\ f_0(E)\Delta E(E,0,\mathbf{s},\phi)$$
$$+\frac{1}{2\pi}\int_0^{2\pi} d\phi \int_{-\infty}^0 dv_x\ v_x \int d\mathbf{s}\ f_0(E + \Delta E)\Delta E(E,0,\mathbf{s},\phi).$$ (B8)

Since the process is assumed to be stationary, Eq. (B8) must be invariant under time reversal. The only effect of the time-reversal operator on Eq. (B8) is to change the sign of v_x (strictly speaking, it also changes the phase by a constant, but since we are integrating over all ϕ, this is irrelevant). The time-reversed form of Eq. (B8) is thus

$$P = -\frac{1}{2\pi}\int_0^{2\pi} d\phi \int_{-\infty}^0 dv_x\ v_x \int d\mathbf{s}\ f_0(E)\Delta E(E,0,\mathbf{s},\phi)$$
$$-\frac{1}{2\pi}\int_0^{2\pi} d\phi \int_0^\infty dv_x\ v_x \int d\mathbf{s}\ f_0(E + \Delta E)\Delta E(E,0,\mathbf{s},\phi).$$ (B9)

Adding Eqs. (B8) and (B9) and dividing by 2 gives

$$P = \frac{1}{4\pi}\int_0^{2\pi} d\phi \int_{-\infty}^\infty dv_x\ |v_x|$$
$$\int d\mathbf{s}\left[f_0(E) - f_0(E + \Delta E)\right]\Delta E(E,0,\mathbf{s},\phi)$$
$$= -\frac{1}{2}\int_{-\infty}^\infty dv_x\ |v_x|\int d\mathbf{s}\left\langle\Delta E^2(E,0,\mathbf{s},\phi)\right\rangle_\phi \frac{df_0}{dE}.$$ (B10)

Note that although this expression is second order in the field, as it should be, it achieves second order only through the squaring of ΔE, so that ΔE itself need only be calculated to first order.

Equation (B10) is a surface integral, i.e., the values of v_x and $\mathbf{s}$ in the integral are evaluated on the $x = 0$ surface of the slab. It is useful to rewrite Eq. (B10) in a form involving a volume integral rather than a flux. The integration in Eq. (B10) is shown schematically in Fig. 75.40(b). Since we are calculating ΔE to first order, we can represent the particle trajectories by their unperturbed orbits. Consider the six-dimensional "flux tube" traced out by a phase-space volume element crossing the slab along an unperturbed orbit (which need not be a straight line). The rate at which phase-space volume enters the tube is $v_x d\mathbf{s}$, and since in a collisionless process phase-space volume is conserved, the volume of the flux tube is given by

$$\Delta V = t_0(E,\mathbf{s})\,v_x\,d\mathbf{s},$$ (B11)

where $t_0(E,\mathbf{s})$ is the time taken for a particle following the orbit to cross the slab. Since phase-space volume moves as an

incompressible fluid, flux tubes cannot intersect, and a set of these flux tubes whose collective cross section comprises the $x = 0$ plane will exactly fill the phase-space volume within the slab. Furthermore, the (unperturbed) flux $v_x d\mathbf{s}$ through the tube is a constant, so we may deform the slab boundary as shown by the dotted contour in Fig. 75.40(b) without affecting the validity of Eq. (B11); the volume of the tube and the time taken to pass along it are reduced in the same proportion. As long as the deformed boundary is outside the volume V in which the potential is nonvanishing, ΔE is also unaffected, so we may deform the original slab boundary to conform to the boundary of V and use Eq. (B11) to convert Eq. (B10) to an integral over the phase space within V:

$$P = -\frac{1}{2} \int_V d^3\mathbf{r} \int d^3\mathbf{v} \frac{\left\langle \Delta E^2 (\mathbf{r}, \mathbf{v}, \phi) \right\rangle_\phi}{t_0 (\mathbf{r}, \mathbf{v})} \frac{df_0}{dE}$$

$$= \frac{1}{2} \int d^3\mathbf{r} \int d^3\mathbf{v} \Delta P, \tag{B12}$$

where ΔP is the expression for the energy loss for a volume of phase space we wrote down immediately on the basis of time-reversal invariance in Eq. (1) at the beginning of this article. We have derived Eq. (B12) from Eq. (B1) here to demonstrate the equivalence of our approach to earlier formulations of transit-time damping, which are also based on Eq. (B1).

REFERENCES

1. L. Landau, J. Phys., USSR **X**, 25 (1946).

2. J. Dawson, Phys. Fluids **4**, 869 (1961).

3. G. Schmidt, *Physics of High Temperature Plasmas* (Academic Press, New York, 1966), pp. 199–210.

4. R. C. Davidson, *Methods in Nonlinear Plasma Theory* (Academic Press, New York, 1972), pp. 57–62.

5. E. M. Lifshitz and L. P. Pitaevskifi, *Physical Kinetics*, Course of Theoretical Physics, Vol. 10, 1st ed. (Pergamon Press, Oxford, 1981), pp. 127–128.

6. D. R. Nicholson, *Introduction to Plasma Theory*, Wiley Series in Plasma Physics (Wiley, New York, 1983), pp. 87–92.

7. G. J. Morales and Y. C. Lee, Phys. Rev. Lett. **33**, 1534 (1974).

8. P. A. Robinson, Phys. Fluids B **1**, 490 (1989).

9. P. A. Robinson, Phys. Fluids B **3**, 545 (1991).

10. R. W. Short and A. Simon, "Collisionless Damping of Localized Plasma Waves in Laser-Produced Plasmas and Application to Stimulated Raman Scattering in Filaments," to be published in LLE Review **76**.

11. M. Colunga, J. F. Luciani, and P. Mora, Phys. Fluids **29**, 3407 (1986).

Publications and Conference Presentations

Publications

A. Babushkin and W. Seka, "Efficient, End-Pumped, 1053-nm Nd:YLF Laser," in *Advanced Solid State Lasers*, edited by W. R. Bosenberg and M. M. Fejer, OSA Trends in Optics and Photonics Series, Vol. 19 (Optical Society of America, Washington, DC, 1998), pp. 111–113.

A. Babushkin, W. Seka, S. A. Letzring, W. Bittle, M. Labuzeta, M. Miller, and R. Roides, "Multicolor Fiducial Laser for Streak Cameras and Optical Diagnostics for the OMEGA Laser System," in *22nd International Congress on High-Speed Photography and Photonics*, edited by D. L. Paisley and A. M. Frank (SPIE, Bellingham, WA, 1997), Vol. 2869, pp. 540–544.

R. Betti, V. N. Goncharov, R. L. McCrory, and C. P. Verdon, "Growth Rates of the Ablative Rayleigh–Taylor Instability in Inertial Confinement Fusion," Phys. Plasmas **5**, 1446 (1998).

S. E. Bodner, D. G. Colombant, J. H. Gardner, R. H. Lehmberg, S. P. Obenschain, L. Phillips, A. J. Schmitt, J. D. Sethian, R. L. McCrory, W. Seka, C. P. Verdon, J. P. Knauer, B. B. Afeyan, and H. T. Powell, "Direct-Drive Laser Fusion: Status and Prospects," Phys. Plasmas **5**, 1901 (1998).

D. K. Bradley, J. A. Delettrez, R. Epstein, R. P. J. Town, C. P. Verdon, B. Yaakobi, S. Regan, F. J. Marshall, T. R. Boehly, J. P. Knauer, D. D. Meyerhofer, V. A. Smalyuk, W. Seka, D. A. Haynes, Jr., M. Gunderson, G. Junkel, C. F. Hooper, Jr., P. M. Bell, T. J. Ognibene, and R. A. Lerche, "Measurements of Core and Pusher Conditions in Surrogate Capsule Implosions on the OMEGA Laser System," Phys. Plasmas **5**, 1870 (1998) (invited).

S.-H. Chen, J. C. Mastrangelo, B. M. Conger, A. S. Kende, and K. L. Marshall, "Synthesis and Characterization of Thermotropic Chiral-Nematic Polythiophenes," Macromolecules **31**, 3391 (1998).

A. V. Chirokikh, W. Seka, A. Simon, R. S. Craxton, and V. T. Tikhonchuk, "Stimulated Brillouin Scattering in Long-Scale-Length Laser Plasmas," Phys. Plasmas **5**, 1104 (1998).

M. E. DeRosa, W. W. Adams, T. J. Bunning, H. Shi, and S.-H. Chen, "Dynamic Mechanical Relaxation Behavior of Low Molecular Weight Side-Chain Cyclic Liquid Crystalline Compounds near the Glass Transition Temperature," Macromolecules **29**, 5650 (1996).

P. M. Fauchet, "Porous Silicon: Photoluminescence and Electroluminescent Devices," in *Light Emission in Silicon*, edited by D. J. Lockwood, Semiconductors and Semimetals Series, Vol. 49 (Academic Press, Orlando, 1996), Chap. 6, pp. 205–252.

D. Fried, W. Seka, R. E. Glena, and J. D. B. Featherstone, "Permanent and Transient Changes in the Reflectance of CO_2-Laser–Irradiated Dental Hard Tissues at λ = 9.3, 9.6, 10.3, and 10.6 μm and at Fluences of 1–20 J/cm^2," Lasers Surg. Med. **20**, 22 (1997).

R. E. Giacone, C. J. McKinstrie, and R. Betti, "Response to 'Comment on "Angular Dependence of Stimulated Brillouin Scattering in Homogeneous Plasma" [Phys. Plasmas **5**, 1215 (1998)]'," Phys. Plasmas **5**, 1218 (1998).

B. E. Gillman and S. D. Jacobs, "Bound-Abrasive Polishers for Optical Glass," Appl. Opt. **37**, 3498 (1998).

W. Göb, W. Lang, and R. Sobolewski, "Magnetoresistance of a $YBa_2Cu_3O_7$ Corbino Disk: Probing Geometrical Contributions to the Unconventional Normal-State Magnetoresistance of High-Temperature Superconductors," Phys. Rev. B: Rapid Commun. **57**, R8150 (1998).

K. Green, M. Lindgren, C.-C. Wang, L. Fuller, T. Y. Hsiang, W. Seka, and R. Sobolewski, "Picosecond Photoresponse in Polycrystalline Silicon," in *Ultrafast Electronics and Opto-electronics, 1997*, edited by M. Nuss and J. Bowers, OSA Trends in Optics and Photonics Series, Vol. 13 (Optical Society of America, Washington, DC, 1997), pp. 106–109.

M. J. Guardalben, "Conoscopic Alignment Methods for Birefringent Optical Elements in Fusion Lasers," Appl. Opt. **36**, 9107 (1997).

O. E. Hanuch, V. B. Agrawal, S. Papernov, M. delCerro, and J. V. Aquavella, "Posterior Capsular Polishing with the Nd:YLF Picosecond Laser: Model Eye Study," J. Refract. Surg. **23**, 1561 (1997).

S. D. Jacobs, "Deterministic Manufacturing of Precision Glass Optics Using Magnetorheological Finishing (MRF)," in *Advances in Fusion and Processing of Glass II*, edited by A. G. Clare and L. E. Jones, Ceramic Transactions, Vol. 82 (The American Ceramic Society, Westerville, OH, 1998), pp. 457–468.

D. Jacobs-Perkins, M. Currie, K. T. Tang, C.-C. Wang, C. Williams, W. R. Donaldson, R. Sobolewski, and T. Y. Hsiang, "Subpicosecond Electro-optic Imaging Using Interferometric and Polarimetric Apparatus," in *Ultrafast Electronics and Optoelectronics, 1997*, edited by M. Nuss and J. Bowers, OSA Trends in Optics and Photonics Series, Vol. 13 (Optical Society of America, Washington, DC, 1997), pp. 202–207.

O. A. Konoplev and D. D. Meyerhofer, "Cancellation of *B*-Integral Accumulation for CPA Lasers," IEEE J. Sel. Top. Quantum Electron. **4**, 459 (1998).

W. Kordonski, D. Golini, P. Dumas, S. Hogan, and S. Jacobs, "Magnetorheological Suspension-Based Finishing Technology," in *Smart Structures and Materials 1998: Industrial and Commercial Applications of Smart Structures Technologies*, edited by J. M. Sater (SPIE, Bellingham, WA, 1998), Vol. 3326, pp. 527–535.

J. C. Lambropoulos, S. D. Jacobs, B. Gillman, F. Yang, and J. Ruckman, "Subsurface Damage in Microgrinding Optical Glasses," in *Advances in Fusion and Processing of Glass II*, edited by A. G. Clare and L. E. Jones, Ceramic Transactions, Vol. 82 (American Ceramic Society, Westerville, OH, 1998), pp. 469–474.

M. Lindgren, W.-S. Zeng, M. Currie, C. Williams, T. Y. Hsiang, P. M. Fauchet, R. Sobolewski, S. H. Moffat, R. A. Hughes, J. S. Preston, and F. A. Hegmann, "An Ultrafast High-T_c Superconducting Y-Ba-Cu-O Photodetector," in *Ultrafast Electronics and Optoelectronics, 1997*, edited by M. Nuss and J. Bowers, OSA Trends in Optics and Photonics Series, Vol. 13 (Optical Society of America, Washington, DC, 1997), pp. 102–105.

S. G. Lukishova, S. V. Belyaev, K. S. Lebedev, E. A. Magulariya, A. W. Schmid, and N. V. Malimonenko, "Behaviour of Non-linear Liquid-Crystal Mirrors, Made of a Nonabsorbing Cholesteric, in the Cavity of an Nd:YAG Laser Operating in the cw Regime and at a High Pulse Repetition Frequency," Quantum Electron. **26**, 796 (1996).

S. G. Lukishova, K. S. Lebedev, E. A. Magulariya, S. V. Belyaev, N. V. Malimonenko, and A. W. Schmid, "Nonlinear 'Brightening' of a Film of Nonabsorbing Chiral Nematic Under Selective Reflection Conditions," JETP Lett. **63**, 423 (1996).

S. G. Lukishova, S. V. Belyaev, K. S. Lebedev, E. A. Magulariya, A. W. Schmid, and N. V. Malimonenko, "Nonlinear Bleaching in the Selective Reflection of Nonabsorbing Chiral-Nematic Liquid-Crystal Thin Films," Mol. Cryst. Liq. Cryst. **303**, 79 (1997).

F. J. Marshall, M. M. Allen, J. P. Knauer, J. A. Oertel, and T. Archuleta, "A High-Resolution X-Ray Microscope for Laser-Driven Planar-Foil Experiments," Phys. Plasmas **5**, 1118 (1998).

C. J. McKinstrie, A. V. Kanaev, V. T. Tikhonchuk, R. E. Giacone, and H. X. Vu, "Three-Dimensional Analysis of the Power Transfer Between Crossed Laser Beams," Phys. Plasmas **5**, 1142 (1998).

C. J. McKinstrie and E. J. Turano, "Nonrelativistic Motion of a Charged Particle in an Electromagnetic Field," J. Plasma Phys. **59**, 555 (1998).

T. J. Murphy, J. M. Wallace, N. D. Delamater, C. W. Barnes, P. Gobby, A. A. Hauer, E. L. Lindman, G. Magelssen, J. B. Moore, J. A. Oertel, R. Watt, O. L. Landen, P. Amendt, M. Cable, C. Decker, B. A. Hammel, J. A. Koch, L. J. Suter, R. E. Turner, R. J. Wallace, F. J. Marshall, D. Bradley, R. S. Craxton, R. Keck, J. P. Knauer, R. Kremens, and J. D. Schnittman, "Indirect-Drive Experiments Utilizing Multiple

Beam Cones in Cylindrical Hohlraums on OMEGA," Phys. Plasmas **5**, 1960 (1998).

S. Papernov, D. Zaksas, and A. W. Schmid, "A Nonlinear UV-Damage Mechanism in Polymer Thin Films Observed from Below to Above Damage Threshold," in *Laser-Induced Damage in Optical Materials: 1997*, edited by G. J. Exarhos, A. H. Guenther, M. R. Kozlowski, and M. J. Soileau (SPIE, Bellingham, WA, 1998), Vol. 3244, pp. 509–515.

S. Papernov, D. Zaksas, and A. W. Schmid, "Perfluorinated Polymer Films with Extraordinary UV-Laser-Damage Resistance," in *Laser-Induced Damage in Optical Materials: 1997*, edited by G. J. Exarhos, A. H. Guenther, M. R. Kozlowski, and M. J. Soileau (SPIE, Bellingham, WA, 1998), Vol. 3244, pp. 522–527.

S. Papernov, D. Zaksas, J. F. Anzellotti, D. J. Smith, A. W. Schmid, D. R. Collier, and F. A. Carbone, "One Step Closer to the Intrinsic Laser-Damage Threshold of HfO_2 and SiO_2 Monolayer Thin Films," in *Laser-Induced Damage in Optical Materials: 1997*, edited by G. J. Exarhos, A. H. Guenther, M. R. Kozlowski, and M. J. Soileau (SPIE, Bellingham, WA, 1998), Vol. 3244, pp. 434–445.

A. L. Rigatti and D. J. Smith, "Status of Optics on the OMEGA Laser System after 18 Months of Operation," in *Laser-Induced Damage in Optical Materials: 1996*, edited by H. E. Bennett, A. H. Guenther, M. R. Kozlowski, B. E. Newnam, and M. J. Soileau (SPIE, Bellingham, WA, 1997), Vol. 2966, pp. 441–450.

M. D. Skeldon, A. Babushkin, J. D. Zuegel, R. L. Keck, A. V. Okishev, and W. Seka, "Modeling of an Actively Stabilized Regenerative Amplifier for OMEGA Pulse-Shaping Applications," in *Second Annual International Conference on Solid State Lasers for Application to Inertial Confinement Fusion*, edited by M. L. André (SPIE, Bellingham, WA, 1997), Vol. 3047, pp. 129–135.

D. J. Smith, J. F. Anzellotti, S. Papernov, and Z. R. Chrzan, "High Laser-Induced-Damage Threshold Polarizer Coatings for 1054 nm," in *Laser-Induced Damage in Optical Materials: 1996*, edited by H. E. Bennett, A. H. Guenther, M. R. Kozlowski, B. E. Newnam, and M. J. Soileau (SPIE, Bellingham, WA, 1997), Vol. 2966, p. 250.

C. Stockinger, W. Markowitsch, W. Lang, W. Kula, and R. Sobolewski, "Mechanisms of Photodoping in Oxygen-Deficient $YBa_2Cu_3O_x$ Films Studied by *In Situ* Transport Measurements," Phys. Rev. B **57**, 8702 (1998).

Forthcoming Publications

R. Adam, R. Sobolewski, W. Markowitsch, C. Stockinger, and W. Lang, "Optically Induced Effects in Y-Ba-Cu-O Josephson Junctions," to be published in Applied Superconductivity.

E. L. Alfonso, S.-H. Chen, R. Q. Gram, and D. R. Harding, "Properties of Polyimide Shells Made Using Vapor Phase Deposition," to be published in the Journal of Materials Research.

A. Babushkin, R. S. Craxton, S. Oskoui, M. J. Guardalben, R. L. Keck, and W. Seka, "Demonstration of the Dual-Tripler Scheme for Increased-Bandwidth Third-Harmonic Generation," to be published in Optics Letters.

R. Betti, "Beta Limits for the $N = 1$ Mode in Rotating-Toroidal-Resistive Plasmas Surrounded by a Resistive Wall," to be published in Physics of Plasmas.

T. R. Boehly, R. L. McCrory, C. P. Verdon, W. Seka, S. J. Loucks, A. Babushkin, R. E. Bahr, R. Boni, D. K. Bradley, R. S. Craxton, J. A. Delettrez, W. R. Donaldson, R. Epstein, D. Harding, P. A. Jaanimagi, S. D. Jacobs, K. Kearney, R. L. Keck, J. H. Kelly, T. J. Kessler, R. L. Kremens, J. P. Knauer, D. J. Lonobile, L. D. Lund, F. J. Marshall, P. W. McKenty, D. D. Meyerhofer, S. F. B. Morse, A. Okishev, S. Papernov, G. Pien, T. Safford, J. D. Schnittman, R. Short, M. J. Shoup III, M. Skeldon, S. Skupsky, A. W. Schmid, V. A. Smalyuk, D. J. Smith, J. M. Soures, M. Wittman, and B. Yaakobi, "Inertial Confinement Fusion Experiments with OMEGA—a 30-kJ, 60-Beam UV Laser," to be published in the Proceedings of the 1997 IAEA Conference, Osaka, Japan, 10–14 March 1997.

T. R. Boehly, V. A. Smalyuk, D. D. Meyerhofer, J. P. Knauer, D. K. Bradley, R. S. Craxton, M. J. Guardalben, S. Skupsky, and T. J. Kessler, "The Reduction of Laser Imprinting Using Polarization Smoothing on a Solid-State ICF Laser," to be published in Physical Review Letters.

S.-H. Chen, J. C. Mastrangelo, B. M. Conger, and D. Katsis, "Design, Synthesis, and Potential Application of Glass-Forming Functional Organic Materials," to be published in the Proceedings of the 6th International Polymer Conference, Kusatsu, Japan, 20–24 October 1997 (invited).

T. J. B. Collins, A. Frank, J. E. Bjorkman, and M. Livio, "Supernova 1987A: Rotation and a Binary Companion," to be published in Astrophysical Journal.

T. J. B. Collins, H. L. Helfer, and H. M. Van Horn, "Accretion Disk and Boundary Layer Models Incorporating OPAL Opacities," to be published in Astrophysical Journal.

T. J. B. Collins, H. L. Helfer, and H. M. VanHorn, "A Model for QPO's in CV's Based on Boundary-Layer Oscillations," to be published in Astrophysical Journal, Letters.

S. Cremer, C. P. Verdon, and R. D. Petrasso, "Tertiary Proton Diagnostics in Future ICF Experiments," to be published in Physics of Plasmas.

M. Currie, R. Sobolewski, and T. Y. Hsiang, "Subterahertz Signal Crosstalk in Transmission Line Interconnects," to be published in Applied Physics Letters.

M. Currie, C.-C. Wang, R. Sobolewski, and T. Y. Hsiang, "Picosecond Nodal Testing of Centimeter-Size Superconducting Microstrip Interconnects," to be published in Applied Superconductivity.

F. Dahmani, J. C. Lambropoulos, A. W. Schmid, S. J. Burns, and C. Pratt, "Nanoindentation Technique for Measuring Residual Stress Field Around a Laser-Induced Crack in Fused Silica," to be published in the Journal of Materials Science.

F. Dahmani, J. C. Lambropoulos, A. W. Schmid, S. Papernov, and S. J. Burns, "Fracture of Fused Silica with 351-nm-Laser-Generated Surface Cracks," to be published in the Journal of Applied Physics.

F. Dahmani, A. W. Schmid, J. C. Lambropoulos, and S. J. Burns, "Laser-Fluence and Laser-Pulse-Number Dependence of Birefringence and Residual Stress near Laser-Induced Cracks in Fused Silica," to be published in Applied Optics.

D. R. Harding, "Using Ion Beam Techniques to Determine the Elemental Composition of ICF Targets," to be published in Fusion Technology.

S. D. Jacobs, W. I. Kordonski, and H. M. Pollicove, "Precision Control of Aqueous Magnetorheological Fluids for Finishing of Optics," to be published in the Proceedings of ERMR 1997, Yonezawa, Japan, 22–25 November 1997.

S. D. Jacobs, H. M. Pollicove, W. I. Kordonski, and D. Golini, "Magnetorheological Finishing (MRF) in Deterministic Optics Manufacturing," to be published in the Proceedings of ICPE '97, Taipei, Taiwan, 20–22 November 1997.

D. Katsis, S.-H. Chen, H. Shi, and A. W. Schmid, "Circular Dichroism Induced in Chiral-Nematic Films," to be published in the MRS Symposium Proceedings, Volume XXX.

J. P. Knauer, R. Betti, D. K. Bradley, T. R. Boehly, T. J. B. Collins, V. N. Goncharov, P. W. McKenty, D. D. Meyerhofer, V. A. Smalyuk, C. P. Verdon, S. G. Glendinning, D. H. Kalantar, and R. G. Watt, "Single-Mode Rayleigh–Taylor Growth-Rate Measurements with the OMEGA Laser System," to be published in Physics of Plasmas.

O. A. Konoplev and D. D. Meyerhofer, "Cancellation of B-Integral Accumulation for CPA Lasers," to be published in Optics Letters.

E. M. Korenic, S. D. Jacobs, S. M. Faris, and L. Li, "Cholesteric Liquid Crystal Flakes—a New Form of Domain," to be published in Molecular Crystals and Liquid Crystals.

E. M. Korenic, S. D. Jacobs, S. M. Faris, and L. Li, "Cholesteric Liquid Crystal Transmission Profile Asymmetry," to be published in Molecular Crystals and Liquid Crystals.

E. M. Korenic, S. D. Jacobs, S. M. Faris, and L. Li, "Color Gamut of Cholesteric Liquid Crystal Films and Flakes by Standard Colorimetry," to be published in COLOR Research and Application.

M. Lindgren, W.-S. Zeng, M. Currie, R. Sobolewski, S. Cherednichenko, B. Voronov, and G. N. Gol'tsman, "Picosecond Response of a Superconducting Hot-Electron NbN Photodetector," to be published in Applied Superconductivity.

F. J. Marshall and G. R. Bennett, "A High-Energy X-Ray Microscope for ICF," to be published in the Review of Scientific Instruments.

K. L. Marshall, J. Haddock, N. Bickel, D. Singel, and S. D. Jacobs, "Angular-Scattering Characteristics of Ferroelectric Liquid Crystal Electro-Optical Devices Operating in the TSM and ESM Modes," to be published in the Journal of Applied Optics.

R. L. McCrory and J. M. Soures, "Status of Direct-Drive Inertial Confinement Fusion Research at the Laboratory for Laser Energetics," to be published in the Proceedings of the 2nd Symposium on Current Trends in International Fusion Research: Review and Assessment, Washington, DC, 10–14 March 1997 (invited).

S. J. McNaught, J. P. Knauer, and D. D. Meyerhofer, "Photoelectron Initial Conditions for Tunneling Ionization in a Linearly Polarized Laser," to be published in Physical Review A.

D. D. Meyerhofer, X. D. Cao, Y. Fisher, O. Konoplev, I. Walmsley, and L. Zheng, "Measurements of Material Properties Using Frequency Domain Interferometry," to be published in the IEEE Journal of Selected Topics in Quantum Electronics.

D. D. Meyerhofer, J. P. Knauer, S. J. McNaught, and C. I. Moore, "Observation of Relativistic Ponderomotive Scattering," to be published in Physics of Plasmas.

B. Nodland and C. J. McKinstrie, "Propagation of a Short Laser Pulse in a Plasma," to be published in Physical Review E.

S. Papernov, A. W. Schmid, and D. Zaksas, "Characterization of Freestanding Polymer Films for Application in 351-nm, High-Peak-Power Laser Systems," to be published in Optical Engineering.

R. D. Petrasso, C. K. Li, M. D. Cable, S. M. Pollaine, S. W. Haan, T. P. Bernat, J. D. Kilkenny, S. Cremer, J. P. Knauer, C. P. Verdon, and R. L. Kremens, "Implosion Symmetry and ρR Measurements of the National Ignition Facility from Nascent 31-MeV Tertiary Protons," to be published in Physical Review Letters.

R. W. Short and A. Simon, "Collisionless Damping of Localized Plasma Waves in Laser-Produced Plasmas and Application to Stimulated Raman Scattering in Filaments," to be published in Physics of Plasmas.

R. W. Short and A. Simon, "Landau Damping and Transit-Time Damping of Localized Plasma Waves in General Geometries," to be published in Physics of Plasmas.

M. D. Skeldon, "A High-Bandwidth Electrical-Waveform Generator Based on Aperture-Coupled Striplines for Optical Pulse-Shaping Applications," to be published in the IEEE Journal of Quantum Electronics.

M. D. Skeldon, R. Saager, and W. Seka, "Quantitative Pump-Induced Wavefront Distortions in Laser-Diode- and Flash-Lamp-Pumped Nd:YLF Laser Rods," to be published in the IEEE Journal of Quantum Electronics.

V. A. Smalyuk, T. R. Boehly, D. K. Bradley, J. P. Knauer, and D. D. Meyerhofer, "Characterization of an X-Ray Radiographic System Used for Laser-Driven Planar Target Experiments," to be published in the Review of Scientific Instruments.

E. A. Startsev and C. J. McKinstrie, "Relativistic Ponderomotive Dynamics of a Test Particle in a Plasma," to be published in Physical Review E.

B. Yaakobi and F. J. Marshall, "Imaging the Cold, Compressed Shell in Laser Implosions Using the Kα Fluorescence of a Titanium Dopant," to be published in the Journal of Quantitative Spectroscopy and Radiative Transfer.

B. Yaakobi, F. J. Marshall, and D. K. Bradley, "Kα Cold Target Imaging and Preheat Measurement Using Pinhole-Array X-Ray Spectrometer," to be published in the Review of Scientific Instruments.

B. Yaakobi, F. J. Marshall, and D. K. Bradley, "Pinhole-Array X-Ray Spectrometer for Laser-Fusion Experiments," to be published in Applied Optics.

L. Zheng and D. D. Meyerhofer, "Self- and Cross-Plate Modulation Coefficients in a KDP Crystal Measured by a Z-Scan Technique," to be published in the Journal of the Optical Society of America B.

J. D. Zuegel and W. Seka, "Upconversion and Reduced $^4F_{3/2}$ Upper-State Lifetime in Intensely Pumped Nd:YLF," to be published in Applied Optics: Lasers, Photonics, & Environmental Optics.

Conference Presentations

A. R. Staley, D. J. Smith, R. C. Eriksson, and R. P. Foley, "Counter-Rotating Planetary Design Increases Production Capacity for Large Rectangular Substrates," 41st Annual Technical Conference of the Society of Vacuum Coaters, Boston, MA, 18–23 April 1998.

———

The following presentations were made at the Target Fabrication Meeting 1998, Jackson Hole, WY, 19–23 April 1998:

E. L. Alfonso, S.-H. Chen, R. Q. Gram, D. R. Harding, and F. Y. Tsai, "Fabrication of Polyimide Shells by Vapor Phase Deposition for Use as ICF Targets."

D. R. Harding, "Using Ion Beam Techniques to Determine the Elemental Composition of ICF Targets."

P. W. McKenty, "Direct-Drive Capsule Requirements for the National Ignition Facility and OMEGA Laser Systems" (invited).

P. W. McKenty and M. D. Wittman, "Characterization of Thick Cryogenic Layers Using an Interferometric Imaging System."

M. D. Wittman, S. Scarantino, and D. R. Harding, "Controlling the Permeability of Shinethrough Barriers on Inertial Fusion Targets."

———

The following presentations were made at CLEO/IQEC 1998, San Francisco, CA, 3–8 May 1998:

A. Babushkin, R. S. Craxton, S. Oskoui, M. J. Guardalben, R. L. Keck, and W. Seka, "Demonstration of the Dual-Tripler Scheme for Increased-Bandwidth Frequency Tripling."

A. Babushkin and W. Seka, "Efficient 1053-nm Nd:YLF Laser End Pumped by a 100-W Quasi-cw Diode Array."

A. V. Okishev, M. D. Skeldon and W. Seka, "New Dual-Regime, Diode-Pumped Master Oscillator for the OMEGA Pulse-Shaping System."

M. D. Skeldon, A. Okishev, R. Keck, W. Seka and S. A. Letzring, "A High-Bandwidth Electrical-Waveform Generator Based on Aperture-Coupled Striplines for OMEGA Pulse-Shaping Applications."

———

The following presentations were made at the 25th European Conference on Laser Interaction with Matter (25th ECLIM), Formia, Italy, 4–8 May 1998:

R. Betti, V. N. Goncharov, and R. L. McCrory, "Hydrodynamic Stability Theory of Unsteady Ablation Fronts."

T. R. Boehly, D. D. Meyerhofer, J. P. Knauer, D. K. Bradley, T. Collins, J. A. Delettrez, V. N. Goncharov, R. L. Keck, S. Regan, V. A. Smalyuk, W. Seka, and R. P. J. Town, "Laser-Uniformity and Hydrodynamic-Stability Experiments at the OMEGA Laser Facility."

D. K. Bradley, J. A. Delettrez, R. Epstein, F. J. Marshall, S. Regan, R. P. J. Town, B. Yaakobi, D. A. Haynes, Jr., C. F. Hooper, Jr., and C. P. Verdon, "Spherical Rayleigh–Taylor Experiments on the 60-Beam OMEGA Laser System."

J. P. Knauer, C. P. Verdon, T. J. B. Collins, V. N. Goncharov, R. Betti, T. R. Boehly, D. D. Meyerhofer, and V. A. Smalyuk, "Interpretation of X-Ray Radiographic Images of Rayleigh–Taylor Unstable Interfaces."

R. L. McCrory, "Strategy for Direct-Drive Ignition on the NIF."

D. D. Meyerhofer, D. K. Bradley, A. V. Chirokikh, R. S. Craxton, S. Regan, W. Seka, R. W. Short, A. Simon, B. Yaakobi, J. Carroll, and R. P. Drake, "Laser–Plasma Interaction Experiments in NIF Direct-Drive-Scale Plasmas."

W. Seka, T. R. Boehly, D. K. Bradley, V. Glebov, P. A. Jaanimagi, J. P. Knauer, F. J. Marshall, D. D. Meyerhofer, R. Petrasso, S. Regan, J. M. Soures, B. Yaakobi, J. D. Zuegel, R. Bahukutumbi, T. J. B. Collins, R. S. Craxton, J. A. Delettrez, R. L. McCrory, P. W. McKenty, R. W. Short, A. Simon, S. Skupsky, and R. P. J. Town, "Experimental Program at LLE in Support of the Direct-Drive Approach to Ignition for the NIF."

———————

S. J. McNaught and D. D. Meyerhofer, "Photoelectron Initial Conditions for Tunneling Ionization in an Elliptically Polarized Laser," 1998 Annual Meeting of the Division of Atomic, Molecular, and Optical Physics (DAMOP), Santa Fe, NM, 27–30 May 1998.

———————

The following presentations were made at the 12th Topical Conference on High-Temperature Plasma Diagnostics, Princeton, NJ, 7–11 June 1998:

F. J. Marshall and G. R. Bennett, "A High-Energy X-Ray Microscope for ICF."

V. A. Smalyuk, T. R. Boehly, D. K. Bradley, J. P. Knauer, and D. D. Meyerhofer, "Characterization of an X-Ray Radiographic System Used for Laser-Driven Planar Target Experiments."

———————

The following presentations were made at Solid State Lasers for Application (SSLA) to Inertial Confinement Fusion, 3rd Annual International Conference, Monterey, CA, 7–12 June 1998:

A. Babushkin, W. Bittle, S. A. Letzring, M. D. Skeldon, and W. Seka, "Regenerative Amplifier for the OMEGA Laser System."

A. Babushkin, R. S. Craxton, S. Oskoui, M. J. Guardalben, R. L. Keck, and W. Seka, "Experimental Verification of the Dual-Tripler Scheme for Efficient Large-Bandwidth Frequency Tripling."

A. Babushkin, J. H. Kelly, C. T. Cotton, M. Labuzeta, M. Miller, T. A. Safford, R. G. Roides, W. Seka, I. Will, M. D. Tracy, and D. L. Brown, "Compact Nd^{3+}-Based Laser System with Gain $G_{SS} \leq 10^{13}$ and 20-J Output Energy."

K. Green, W. Seka, M. D. Skeldon, R. L. Keck, A. V. Okishev, and R. Sobolewski, "Improving the Microwave Bandwidth of Photoconductive Switches Used in the OMEGA Pulse-Shaping System."

J. A. Marozas, "The Cross-Phase Modulation Between Two Intense Orthogonally Polarized Laser Beams Co-Propagating Through a Kerr-like Medium."

A. V. Okishev, M. D. Skeldon, and W. Seka, "Multipurpose, Diode-Pumped Nd:YLF Laser for OMEGA Pulse Shaping and Diagnostics Applications."

M. D. Skeldon, A. V. Okishev, R. L. Keck, W. Seka, and S. A. Letzring, "An Optical Pulse-Shaping System Based on Aperture-Coupled Stripline for OMEGA Pulse-Shaping Applications."

J. D. Zuegel, E. Michaels, S. Skupsky, S. Craxton, J. Kelly, and S. Letzring, "Plans to Achieve 1-THz Bandwidth with Two-Dimensional Smoothing by Spectral Dispersion on OMEGA."

———————

The following presentations were made at the Optical Interference Coating Sixth Topical Meeting, Tucson, AZ, 7–12 June 1998:

M. B. Campanelli and D. J. Smith, "A Wideband Optical Monitor for a Planetary Coating System."

K. L. Marshall, A. L. Rigatti, G. L. Mitchell, J. A. Pathak, A. R. Staley, and J. A. Warner, "An Aqueous Sol-Gel Coating for Epoxy Surfaces."

D. J. Smith, J. A. Warner, and N. LeBarron, "Uniformity Model for Energetic Ion Process Using a Kaufman Ion Source."

———————

The following presentations were made at the 28th Annual Anomalous Absorption Conference, Bar Harbor, ME, 14–19 June 1998:

R. Betti, V. Lobatchev, and R. L. McCrory, "Perturbation Transfer in an Accelerated Shell: Feed-In and Feed-Out."

R. S. Craxton, D. D. Meyerhofer, and W. Seka, "Interpretation of Long-Scale-Length Plasma Characterization Experiments on OMEGA."

J. A. Delettrez, D. K. Bradley, S. Regan, T. R. Boehly, J. P. Knauer, and V. A. Smalyuk, "Mix Experiments on the 60-Beam OMEGA Laser System Using Smoothing by Spectral Dispersion (SSD)."

R. Epstein, J. A. Delettrez, R. P. J. Town, D. K. Bradley, D. Hayes, C. F. Hooper, and C. P. Verdon, "Simulations in One Dimension of the Effects of Fuel–Pusher Mix in Laser-Driven Implosions on Core Temperatures and Densities Determined from Core Emission Spectroscopy."

Y. Fisher, T. R. Boehly, D. K. Bradley, D. R. Harding, D. D. Meyerhofer, and M. D. Wittman, "Shinethrough of Various Barrier-Layer Materials."

R. E. Giacone and C. J. McKinstrie, "Angular Dependence of Stimulated Brillouin Scattering."

V. Lobatchev, R. Betti, and R. L. McCrory, "Theory of the Linear Feed-Out in Planar Geometry."

C. J. McKinstrie and E. A. Startsev, "Forward and Backward Stimulated Brillouin Scattering of Crossed Laser Beams."

D. D. Meyerhofer, T. R. Boehly, D. K. Bradley, T. Collins, J. A. Delettrez, V. N. Goncharov, J. P. Knauer, R. P. J. Town, V. A. Smalyuk, D. Oron, Y. Szebro, and D. Shvarts, "Late-Time Evolution of Broad-Bandwidth, Laser-Imposed Non-uniformities in Accelerated Foils."

S. P. Regan, D. K. Bradley, A. V. Chirokikh, R. S. Craxton, D. D. Meyerhofer, W. Seka, R. P. J. Town, B. Yaakobi, R. P. Drake, and J. J. Carroll III, "Electron Temperature and Density Measurements of Long-Scale-Length, Laser-Produced Plasmas on OMEGA."

J. D. Schnittman, R. S. Craxton, N. D. Delamater, K. A. Klare, T. J. Murphy, J. M. Wallace, E. I. Lindman, G. R. Magelssen, J. A. Oertel, and S. M. Pollaine, "Radiation Drive Symmetry in OMEGA Tetrahedral Hohlraums."

W. Seka, D. K. Bradley, A. V. Chirokikh, R. S. Craxton, S. Regan, D. D. Meyerhofer, R. W. Short, A. Simon, B. Yaakobi, J. J. Carroll III, and R. P. Drake, "Stimulated Brillouin Backscattering in NIF Direct-Drive Scale Plasmas."

R. W. Short, "Simulated Brillouin Scattering in High-Intensity, Self-Focused Filaments: The Effects of Sound Wave Diffraction and Plasma Flow."

A. Simon, "Return-Current Electrons and Their Generation of Electron Plasma Waves."

A. Simon, "The 'Return' of the Electron Beam."

V. A. Smalyuk, T. R. Boehly, D. K. Bradley, J. P. Knauer, D. D. Meyerhofer, D. Oron, Y. Azebro, and D. Shvarts, "Nonlinear Evolution of the 3-D Broad-Bandwidth Spectrum of Imprinting in Planar Targets Accelerated by UV Light."

E. A. Startsev, C. J. McKinstrie, and R. E. Giacone, "Accurate Formulas for the Landau Damping Rates of Electrostatic Waves."

R. P. J. Town, R. P. Bahukutumbi, J. A. Delettrez, R. Epstein, F. J. Marshall, P. W. McKenty, D. D. Meyerhofer, and S. Skupsky, "Simulations of OMEGA Spherical Implosions."

E. J. Turano and C. J. McKinstrie, "Oblique Stimulated Raman Scattering of a Short Laser Pulse in a Plasma Channel."

———————

The following presentations were made at the IXth Conference on Laser Optics (LO '98), St. Petersburg, Russia, 22–26 June 1998:

J. H. Kelly, S. F. B. Morse, R. Boni, W. R. Donaldson, P. A. Jaanimagi, R. L. Keck, T. J. Kessler, A. V. Okishev, A. Babushkin, A. L. Rigatti, W. Seka, and S. J. Loucks, "Performance of the OMEGA Laser for Direct-Drive ICF."

A. V. Okishev, M. D. Skeldon, J. H. Kelly, A. Babushkin, J. D. Zuegel, R. G. Roides, and S. F. B. Morse, "Front-End Laser System for the 60-Beam, 30-kJ (UV) OMEGA Laser Facility."